Extreme ultraviolet lasers and their interactions with matter

Valentin Aslanyan

Doctor of Philosophy

University of York

Physics

March 2016

Abstract

This work describes the generation and matter interactions of laser radiation with wavelengths between approximately 10 and 100 nanometres. The properties and dynamics of plasmas, created rapidly by photons of this wavelength range through the process of photoionization, are discussed here. A collisional-radiative model has been developed and used to simulate the ion populations in such plasmas and make comparisons with local thermodynamic equilibrium (LTE), which is frequently used to model dense plasmas. Despite the effects of rapid heating, due to the absorption of laser energy, and free electron degeneracy, due to the high densities, it is shown that LTE holds for such laser plasmas. Simulations predict that intense photoionizing radiation can cause a wavelike lowering of opacity to propagate through plasma. A number of experiments have been undertaken using a capillary discharge laser operating in neon-like argon, with a wavelength of 46.9 nanometres. Two focal geometries have been used to create plasmas at solid density: a Fresnel zone plate and a multilayer mirror. The focal intensity profiles in both cases have been modelled by a diffraction code, which closely matched micrographs produced in these experiments. The motion of laser-produced plasmas has been modelled by a 2-dimensional radiation-hydrodynamic code. These simulations were extended to 3 dimensions by a geometrical approach and compared to perforations made in thin targets. Laser experiments have allowed the viability of simultaneously generating and probing dense plasmas to be evaluated for both focusing geometries.

Contents

List of Figures

List of Tables

"At that moment sergeant Lee thought he saw his certain destruction, and as a last act of defence, let go the magazine, expecting that they would seize that likewise, and thus all would be ***blown to atoms*** *together."*

- Charles Griswold, writing in 1820 about an American submersible during the American Revolutionary War (1775-1783)

Acknowledgements

I wish to dedicate this thesis to Steve Madigan, my physics school teacher. He nurtured my interest in physics and I owe him a debt of gratitude for helping me to secure a place at my *alma mater*.

I am most grateful to my supervisor Greg Tallents who gave me the opportunity to conduct this research and expertly advised me at every step of the way. I am also grateful to the other staff and students at the York Plasma Institute, in particular to Luke J. Easy and Peter Hill for help with computing clusters, as well as to many others. I would also like to extend my gratitude to my grandfather, who tirelessly helped me with much of the mathematics in this work.

I would like to thank the team at Colorado State University: Professors Rocca, Menoni and Marconi for allowing me to conduct experiments at their lab and advising me on many important details; Mark Woolston for making the work with electronics very enjoyable; Ilya Kuznetsov for insightful discussions and advice on experiments; Herman Bravo for great aid in experiments, in particular machining an entire vacuum-holding wall, complete with ports, in a single day. A special thanks to Manuel Cotelo for discussions about computation and hydrodynamics.

Declaration

All the work presented in this thesis is the author's original work (unless stated otherwise) and has not been submitted previously for a degree at this or any other university. All sources are acknowledged as references. Elements of this work have been published in:

[1] A. K. Rossall *et al.*, Proceedings of SPIE **8849**, 884912 (2013).

[2] V. Aslanyan and G. J. Tallents, Phys. Plasmas **21**, 062702 (2014).

[3] A. K. Rossall *et al.*, Phys. Rev. Applied **3**, 064013 (2015).

[4] V. Aslanyan and G. J. Tallents, Phys. Rev. E **91**, 063106 (2015).

[5] V. Aslanyan and G. J. Tallents, Proceedings of the 14th International Conference on X-Ray Lasers (2016).

1 Introduction

The laser is an important scientific and industrial tool and there has been success in widening its operational parameters since its invention. In this work, we discuss the interaction with matter of lasers operating in the extreme ultraviolet (EUV) and soft x-ray spectral range, with wavelengths below approximately 100 nm.

The successful implementation of lasing at such low wavelengths, using methods described in this chapter, has led to several advantages over conventional visible lasers. EUV radiation can focused more tightly than the visible, as the diffraction limit scales directly with the wavelength. This gives rise to the potential for applications in manufacturing[6] on the sub-micrometre scale,[3] for example of micro-electromechanical systems (MEMS), which has not yet been realised. Lasers in the EUV spectral range allow the creation and diagnosis of extremely dense, but low temperature plasmas, normally not accessible by conventional lasers. These studies are important to fundamental science, with similar states of matter arising in astrophysical objects such as brown dwarf stars.[7] The combination of the high resolution and coherence of EUV lasers allows many applications in imaging, from microscopy[8] and interferometry[9,10] to ablation mass spectrometry.[11]

In this chapter we introduce the plasma state of matter, which is crucial to understanding the interaction of lasers with matter. We then discuss the methods of generating laser radiation with short wavelengths. In Chapter 2 we outline the mathematical framework of wave optics and its application to focusing such short wavelength radiation. In Chapter 3 we present the energy distribution functions of particles and the rates of atomic processes in plasmas. This allows the macroscopic properties of plasmas in equilibrium to be calculated by a collisional-radiative model. Simulations of non-equilibrium plasmas are presented in Chapter 4. Experiments conducted using an EUV laser are presented in Chapter 5.

This work makes use of notation and unit conventions specific to plasma and atomic physics, which are clarified in Appendix A. In particular, electronvolts are used throughout the work to express energies (1 eV$= 1.602 \times 10^{-19}$ J). Temperatures are implicitly multiplied by the Boltzmann constant k_B and therefore also conveniently expressed in electronvolts. Mathematical methods used throughout this work and associated notation are given in Appendix B. Of particular importance to this work are Brent's algorithm,[12] used to efficiently find the roots of transcendental equations, and methods of numerical integration.

1.1 Plasmas

Laser radiation has an inherently large energy density when focused, which typically leads to a fast rise in temperature of any matter upon which it is incident. Lasers incident on solid targets cause melting and expansion leading to the removal of material, referred to as ablation. In some cases, the radiation or thermal pressure may lead to compression of material to high densities.[13,14] Lasers are inherently out of thermodynamic equilibrium, so they are able to create states of matter without a well-defined temperature. Matter rapidly undergoes a phase transition to a plasma when subjected to intense laser light, regardless of its starting phase. Therefore, laser plasma interactions (LPI) are interchangeable with laser *matter* interactions, and we will go into considerable detail discussing plasmas.

1.1.1 Plasma definition and basic properties

A plasma is a fluid state of matter which exists at high temperatures or densities. The characteristic difference between a plasma and a condensed fluid, such as a liquid or gas, is that matter no longer occupies the lowest possible energy states. In conventional plasmas, energetically favourable molecular bonds break, electrons in atoms become excited to high energy levels or become ionized completely; in extreme conditions electron-positron pairs, which ordinarily seek to annihilate, may coexist.[15,16] Therefore, a plasma inevitably contains many types of charged particles, free to move independently; it is this property of being a "carrier" of a multitude of different particles which led Irving Langmuir to draw a similarity with blood plasma and coin the name for physical plasmas.[17]

Mobile charges in a fluid lead to many remarkable properties, such as unique mechanisms of thermal and electrical conduction, absorption and emission of radiation, collective excitations and response to electromagnetic fields. A great deal of effort is spent on modelling the hydrodynamic behaviour of plasmas, in response to lasers at the micron scale, to magnetic fields in tokamaks on the laboratory scale and to gravity on the galactic scale. However, it should be stressed that the aspect which most sets plasmas apart from other states of matter is that some normally tightly bound particles break into a great diversity of others. Atoms dissociate into ions and electrons; nuclei into quarks and gluons, as temperature and density increases. Much of this work takes a microscopic view of a classical plasma to calculate the numbers of different types of ions, from which macroscopic quantities are derived.

An important property of a classical plasma is the ionization fraction, corre-

sponding to the number of free electrons per atom,

$$Z^* = \frac{n_e}{N_T}, \tag{1}$$

where n_e is the free electron density and N_T the total density of atoms. We will examine why such a seemingly energetically unfavourable state - electrons stripped from nuclei - begins to dominate at high temperature.

Plasmas tend to be quasi-neutral, meaning that a free electron does not stray far from its parent atom and there is no localised space charge. However, the charged particles in a plasma are mobile enough to locally screen any buildup of charge. The potential of a charged particle falls off with distance r not as r^{-1} for Coulomb's law, but as $r^{-1}\exp(-r/\lambda_D)$, where the Debye length is given by[18]

$$\lambda_D = \sqrt{\frac{\varepsilon_0 T_e}{e^2 n_e}}, \tag{2}$$

where T_e is the electron temperature, e the electron's charge and ε_0 is the permittivity of free space. Of particular importance is the so-called plasma parameter, given by

$$\Lambda = 4\pi n_e \lambda_D^3. \tag{3}$$

Plasmas exhibit a similar range of behaviours to condensed matter, from a dilute gas to a dense liquid or solid. A plasma corresponds to one of these regimes based on the coupling parameter Γ. This is defined as the ratio of the Coulomb electrostatic potential to the electron temperature,

$$\Gamma = \frac{e^2}{4\pi\varepsilon_0(\frac{4}{3}\pi n_e)^{-1/3} T_e} = 3^{1/3}\Lambda^{-2/3}, \tag{4}$$

where the distance r is given by the average electron separation. Plasmas exhibit classical gas-like behaviour when they are weakly coupled ($\Gamma < 1$) and more collective and quantum behaviour when they are strongly coupled ($\Gamma > 1$). Laser-produced plasmas may often have wide ranges of the coupling parameter, which complicates their simulation.

Electrical and heat flow is governed by the collision of electrons with ions. The flow of current $\vec{j}$ in plasmas obeys Ohm's law as usual,

$$\vec{\mathcal{E}} = \eta\vec{j}, \tag{5}$$

where $\mathcal{E}$ is the electric field and η the resisivity, which is often given by the Spitzer formula,[19]

$$\eta_{\text{Spitzer}} = \frac{\pi Z^* e^2 m_e^{1/2} \Xi}{(4\pi\varepsilon_0)^2 T_e^{3/2}}, \tag{6}$$

where Ξ is the so-called Coulomb logarithm; it is discussed further in §3.1.1. The resistivity is proportional to the rate of collisions between the electrons and ions. Heat flow in a plasma usually obeys Fourier's law,

$$\vec{q} = -k\nabla T, \tag{7}$$

with an analogous Spitzer heat conductivity,

$$k_{\text{Spitzer}} = \frac{T_e^{5/2}(4\pi\varepsilon_0)^2}{m_e^{1/2} e^4}. \tag{8}$$

However, Fourier's law may break down if the temperature gradient is very steep, as electrons may travel large distance before colliding and therefore depositing energy away from the gradient. This is referred to as non-local transport and may be present in laser-produced plasmas as a result of their extremely high energy fluxes.[20]

The mobile charges in plasmas interact in very novel ways with magnetic fields. This is particularly important in space plasmas (interaction with the Earth's, Sun's, galactic, *etc.* magnetic fields) and laboratory plasmas (magnetic confinement fusion devices, magnetrons, *etc.*). In particular, the magnetic field affects how electromagnetic waves behave in a plasma and alters the collective motion of plasma. However, the magnetic fields are usually insignificant in the typically rapid and intense interactions of short wavelength lasers and so are ignored in this work.

1.1.2 Interaction with radiation

Free electrons in a plasma oscillate about the ions, which remain largely stationary due to inertia. The resonant plasma frequency is given by

$$\omega_p = c\sqrt{\frac{n_e e^2}{m_e c^2 \varepsilon_0}}. \tag{9}$$

The phase of an electromagnetic wave propagating right and left respectively through a medium is given by $\exp(i[\tilde{n}kx \mp \omega t)$, where $\tilde{n}$ is the refractive index. The plasma frequency is added to the usual dispersion relation for electromagnetic waves, so that in a collisionless plasma the relation becomes $\omega^2 = c^2k^2 + \omega_p^2$. Therefore the index of refraction $\tilde{n} = ck/\omega$ due to these collective effects is given by

$$\tilde{n} = \sqrt{1 - \frac{\omega_p^2}{\omega^2}}. \tag{10}$$

Additional collective absorption effects due to collisions or magnetization, such as Landau damping or whistler waves may occur, but are not discussed here.

The refractive index implies that when an electromagnetic wave is incident on a plasma, it is reflected if its frequency is below the plasma frequency. Consequently, for a given frequency of radiation, there is a critical electron density above which it cannot propagate. This critical density for a given photon energy ϵ_γ is given by

$$n_c\,[10^{23}\text{ cm}^{-3}] = 7.252 \times 10^{-3}(\epsilon_\gamma\,[\text{eV}])^2. \tag{11}$$

Visible light ($\epsilon_\gamma \sim 2$ eV) is reflected at densities of around 10^{21} cm^{-3}. Therefore, in most laser plasma experiments, light is reflected from an outwardly expanding low density plasma plume and heat is conducted to the main target by electrons. Plasmas at solid material densities ($n_e > 10^{23}$ cm^{-3}) can only be created and heated directly by photons in the VUV range or above ($\epsilon_\gamma \gtrsim 12$ eV).

The amplitudes of charged particles' oscillations depend on the strength of the driving electric field. If the strength of the electromagnetic field changes during a single period of oscillation, the acceleration in each phase will not cancel out and the particle will not return to its starting position. This effect is called the ponderomotive force, given by

$$\vec{F}_{\text{ponderomotive}} = -\frac{e^2\hbar^2 c}{4\varepsilon_0 m c^2 \epsilon_\gamma^2}\nabla I, \tag{12}$$

where I is the intensity of radiation. We have used the following relation for the electic field $\mathcal{E}$ in an electromagnetic wave: $\mathcal{E}^2 = I/c\varepsilon_0$, derived from the Poynting vector.

In addition to the collective effects we have discussed, the individual interactions of photons with particles are important in plasmas. Radiation is attenuated due to absorption by plasmas at a rate given by

$$\frac{dI}{dx} = -\tau I, \tag{13}$$

where $\tau(\epsilon_\gamma)$ is the opacity. It is usual to relate the opacity to some absorption coefficient $\kappa(\epsilon_\gamma)$ through the relation $\tau = N\kappa$, where N is the density of absorbing material.

Many microscopic processes contribute to the opacity, each with its own absorption coefficient; they are discussed further in §3.3. Photons may scatter from free electrons through a Compton process. A free electron may also absorb a photon, but an ion must be present to conserve momentum; this is referred to as inverse

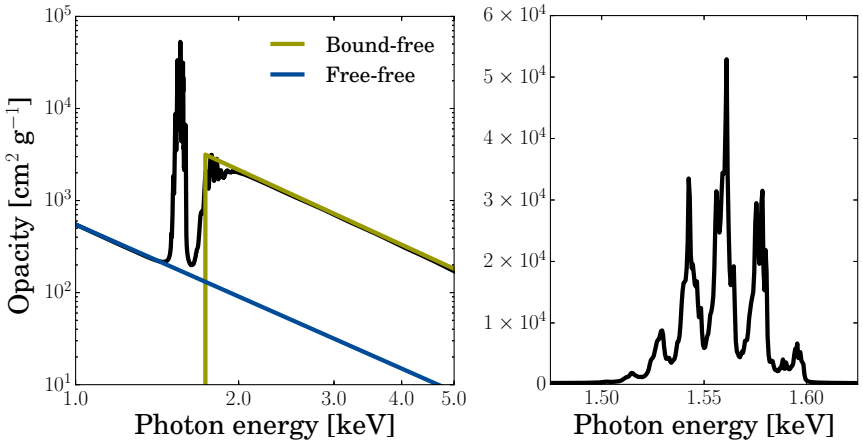

Figure 1: The opacity of aluminium at a density of 1 g cm^{-3} and temperature 100 eV as a function of photon energy, calculated by the TOPS code of the Los Alamos National Laboratory (LANL).[21] The photon energy dependence of the bound-free and free-free opacity is shown. The second plot shows the region of bound-bound transitions in higher resolution.

bremsstrahlung or "free-free" absorption. A photon with sufficient energy may be absorbed by atoms to photoionize a bound electron ("bound-free" absorption). Photons resonant with an atomic transition may be absorbed and excite bound electrons from one quantum state to another ("bound-bound" absorption).

An example of the photon energy dependence of the opacity of an aluminium plasma with a given temperature is given in Figure 1, along with the approximate behaviour of the absorption coefficients of these processes. We see a baseline opacity from free-free absorption, $\propto \epsilon_\gamma^{-3}$, which occurs above the plasma frequency. We see an absorption edge due to bound-free absorption, $\sim \epsilon_\gamma^{-3}$, which corresponds to the minimum threshold energy. Other resonant processes smear out the edge. Finally, we see that the bound-bound absorption resonances have some width due to Doppler and Stark broadening - the motion of ions and perturbing free electrons give the atomic transitions a range of energies. Compton scattering is insignificant to the total opacity in this case.

Bound-free absorption dominates the opacity of neutral materials (at low temperatures) in the EUV and soft x-ray range because the photon energies are just above the first absorption edge. For this reason, lasers in this spectral range can only propagate freely through a vacuum, which complicates experimental setups. However, as the temperature increases, the lower lying ionization stages become depleted and the edge disappears thus lowering the opacity. EUV lasers must therefore be generated by plasmas hot enough to be transparent in this spectral range

and with a density low enough that free-free absorption is insignificant. Solid-state reflective optics for this spectral range are composed of metals or semiconductors, whose outer valence electrons are effectively not bound to atoms and can therefore not contribute to bound-free absorption.

Every atomic process has an associated inverse which balances it in equilibrium, as discussed in §3.3. Therefore, absorption is complemented by the emission of radiation. Lasers are not in a state of thermodynamic equilibrium and therefore they typically produce states of matter which are themselves not in thermodynamic equilibrium.

1.1.3 Hydrodynamic motion

The collective motion of plasma is governed by fluid mechanics.[22] The equations of motion may be expressed through a set of conservation laws, formulated as hyperbolic partial differential equations. A conservation law for a set of quantities $\vec{y}$ may be written as

$$\frac{\partial \vec{y}}{\partial t} + \nabla . \vec{J}(\vec{y}) = \vec{s}, \tag{14}$$

where $\vec{J}$ are the associated fluxes and $\vec{s}$ are appropriate source terms. The conserved quantities for a continuous fluid are densities of mass N, momentum $N\vec{v}$ and energy ε, with $\vec{v}$ the local fluid velocity. The correspoding conservation laws[23] are

$$\frac{\partial}{\partial t}\begin{pmatrix} N \\ N\vec{v} \\ \varepsilon \end{pmatrix} + \nabla . \begin{pmatrix} N\vec{v} \\ N\vec{v} \otimes \vec{v} - \mathbb{I}p \\ \vec{v}(\varepsilon + p) \end{pmatrix} = \begin{pmatrix} 0 \\ \vec{F} \\ \Phi \end{pmatrix}, \tag{15}$$

where p is the pressure, $\vec{F}$ is an externally applied force and Φ is an energy flux. These are typically referred to as the Euler equations for plasmas or the Navier-Stokes equations, where $\vec{F}$ contains a viscosity term, for condensed fluids. These equations are notoriously difficult to solve mathematically and lead to a range of nonlinear and turbulent effects. In plasmas the situation may be complicated because of the large range of densities and pressures which occur. Typically, a plasma is considered to consist of several fluids: electrons and ions are treated separately and interact through collisions.

The Euler equations require "closure" in the form of expressions for the relation of pressure and energy to mass density. Hydrodynamic simulations of plasma require an accurate equation of state for quantities such as Z^*, used to determine the electron

pressure, as a function of the total mass density and temperature. The assumption of thermodynamic equilibrium, discussed in Chapter 3, may enable fast calculation of equation of state. The validity of such assumptions for plasmas created by EUV lasers, which operate manifestly out of equilibrium, is also discussed.

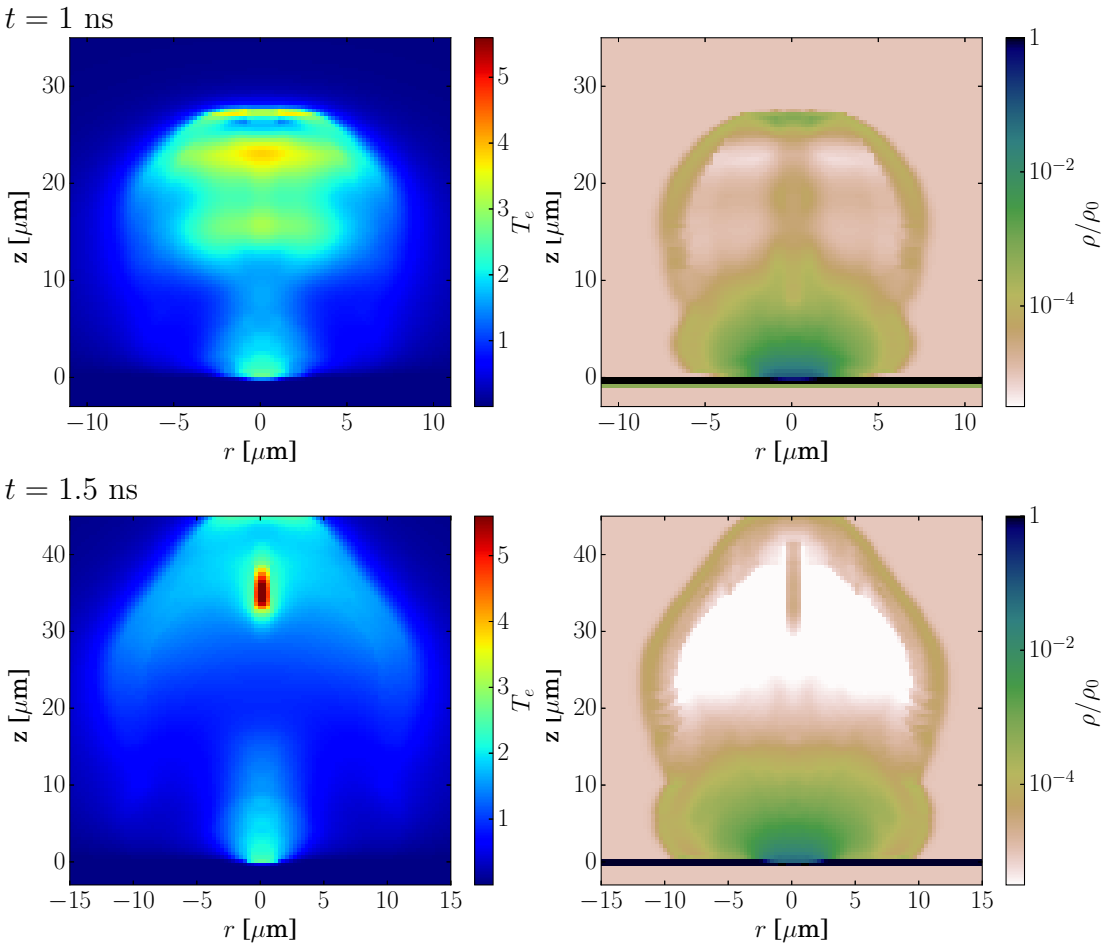

Figure 2: Electron temperature T_e (left) and density ρ (right) profiles simulated by `POLLUX` at times indicated. An EUV laser (photon energy 26.5 eV), incident from the top of page centered on $r = 0$, with a Gaussian profile of width 1 μm and peak intensity 10^{10} W cm^{-2} (centered on $r = 0$) is incident on solid density (labelled by the symbol ρ_0) plastic (parylene-N) located at $z = 0$.

The propagation of radiation, whether from an external source or the plasma itself, appears in the Φ term and is important to plasma simulations. Fluid motion of laser plasmas is typically simulated using a radiation-hydrodynamic code. Space is discretised in up to three dimensions, in the desired co-ordinate system. The radiation field is modified through refraction by ray tracing through the plasma's refractive index and through absorption and emission by computing opacities and emissivities. The fluid motion and local parameters are calculated through the Euler

equations.

To solve the set of Euler equations for a laser-produced plasma, a hydrodynamic code POLLUX was written at the University of York.[24] The three conservation laws of Equation (15) are solved in a 2 dimensional cylindrical geometry (with radial distance r and height z); the system is symmetric about the z-axis (*i.e.* independent of azimuthal coordinate θ). Conventionally, the laser propagates in the negative z direction. The spatial dimensions are discretised into a grid, which evolves in time to resolve the plasma expansion. The interaction of a laser beam is modelled via bound-free and bound-bound absorption up to the critical surface. POLLUX uses an equation of state model provided by the CHART-D package developed at Sandia National Laboratories.[25] The distribution of ionization and excitation stages, required to obtain quantities like Z^*, is modelled assuming local thermodynamic equilibrium (LTE), as discussed in §3.5. POLLUX outputs many plasma parameters, such as ion and electron densities and temperatures, velocities, *etc.* on its spatial grid at regular time intervals; examples at two times are shown in Figure 2. Like many hydrodynamic codes, POLLUX cannot directly simulate a vacuum because a zero material density leads to numerical instabilities. The vacuum regions are set to a small, but finite density value, such as 10^{-5} of solid.

1.2 Lasers

Conventional lasers create photons by optical transitions between two atomic levels. Through the process of stimulated emission (discussed in more detail in §3.3.3) initial photons begin to produce additional photons in a chain reaction. This occurs provided that a population inversion exists and therefore emission of new photons matches or exceeds the rate of their absorption.[26] The requirement for population inversion is given by

$$\Delta N \equiv \left(N_2 - \frac{g_2}{g_1} N_1 \right) > 0, \tag{16}$$

where N_1, N_2 are the densities of atoms in the lower and upper levels of the lasing transition and g_1, g_2 are their degeneracies. The two atomic levels are separated by the laser photon energy ϵ_γ, so that in thermodynamic equilibrium at temperature T the Boltzmann ratio gives $N_2/N_1 = \exp(-\epsilon_\gamma/T) < 1$. The upper lasing level must therefore be "pumped" to achieve population inversion. At least one or more additional levels are needed to achieve a population inversion, as otherwise the rate of emission of photons cannot exceed the rate of absorption; radiation interacting with a two-level atom drives Rabi oscillations,[27] which cannot directly lead to lasing.

Once a population inversion is achieved, there is a net gain of radiation intensity I given by

$$\frac{dI(\epsilon_\gamma)}{dz} = \left[\frac{B_{2\to1}}{c} \epsilon_\gamma f(\epsilon_\gamma) \Delta N \right] I(\epsilon_\gamma), \tag{17}$$

where the term in square brackets is the gain coefficient, $B_{2\to1}$ is the stimulated emission coefficient and $f(\epsilon_\gamma)$ is the spectral lineshape of the transition, which obeys the normalisation condition $\int_0^\infty f(\epsilon_\gamma) d\epsilon_\gamma = 1$. This lineshape arises because the energy split of the two atomic levels is not precisely constant for an ensemble of atoms due to effects such as Doppler shifts. This treatment shows that the acronym for Light Amplified by Stimulated Emission of Radiation does indeed provide a succinct description of its operation.

When the radiation intensity in an amplifier is relatively low, the gain coefficient in Equation (17) takes its small-signal (intensity-independent) value and the intensity grows exponentially. As the intensity grows, the gain becomes saturated as atoms in the upper lasing level are depleted. For example, if the laser transition is homogeneously broadened, the population inversion is effectively reduced to

$$\Delta N(I) = \frac{\Delta N(0)}{1 + I/I_{\text{sat}}}, \tag{18}$$

where I_{sat} is the saturation intensity. From Equation (17), we see that the growth in intensity transitions from exponential to linear growth above the saturation intensity.

Optical lasers typically operate with the gain medium inside a cavity. The beam is amplified as it oscillates between mirrors at two ends of the cavity. However, reflective optics at short wavelengths are extremely difficult to realise and have low overall reflectivities at best, as discussed in §2. Furthermore, for short wavelength lasers the gain is realised only for shorter periods of time than a cavity round-trip. Therefore, extreme ultraviolet and soft x-ray lasers operate on the amplified spontaneous emission (ASE) principle,[28] rather than a true laser oscillator.

In order to generate short wavelength laser beams, we require that atomic energy levels be spaced widely in energy. This occurs readily for highly charged ions with a high atomic number Z. These ions have a large central potential and few electrons to screen the nuclear charge, leading to the large required energy spacing. For example, the energy levels of hydrogen-like ions scale as Z^2. For this reason, and as low charge ions have a high opacity, short wavelength lasers operate in plasmas; the gain medium in free-electron lasers is also a highly energetic state of matter comparable to a plasma. In order to produce the coherent and directional beam of a typical laser, the gain medium must have a large extent in one dimension and be limited in the others. In this section, we discuss approaches to generating such a plasma and achieving population inversion.

Laser light has many attractive properties, which make them ideal for many scientific and industrial applications. It is extremely monochromatic, as they operate on quantised energy levels; despite broadening by dynamic and quantum effects, their wavelength spread is narrow. Laser beams are strongly collimated, with typical divergences of a few milliradians. In part due to this small divergence, laser light is able to reach extremely high intensity. Finally, laser light is coherent - its phase has a well defined relatonship. It should be noted that many intense sources of short wavelength radiation exist, which are not lasers. They can attain some of the aforementioned properties by extensive spatial or wavelength filtering, strong focusing, *etc.* They have the potential advantages of being more compact or cheaper; they may also occur naturally. Though usually more widely applicable, the treatment of interactions in this work assumes that radiation has laser-like properties.

1.2.1 Collisionally pumped lasers

The high energy densities required to create a plasma may be readily reached by optical lasers. They are able to quickly deposit a large amount of energy, which

creates the non-equilibrium atomic level distribution required for lasing. In practice, two separate types of laser pulse are used in tandem - a long prepulse used to setup a relatively slowly varying plasma plume and a short, intense pulse to deliver the bulk energy. Once the energy is deposited, electron collisional processes, as described in §3.3.3, populate the upper lasing levels.

To produce a spatially extended plasma, optical laser light is focused onto a target in a long narrow line - this can be achieved by adding a cylindrical lens to the focusing optics or by employing a tilted mirror. An example of such an experimental setup is shown in Figure 3. By manipulating the angle of incidence of the short pulse, the optimal electron density region may be selected, leading to high energy conversion efficiencies.[29] Elements which form metallic bonds or salts are typcially chosen as the gain medium in such setups because they are reasonably dense, can be machined to precision, are suitable for vacuums and have the requisite high atomic numbers. Alternatively, the same optical setup may be used with a gas cell target[30] instead of a plane slab of material.

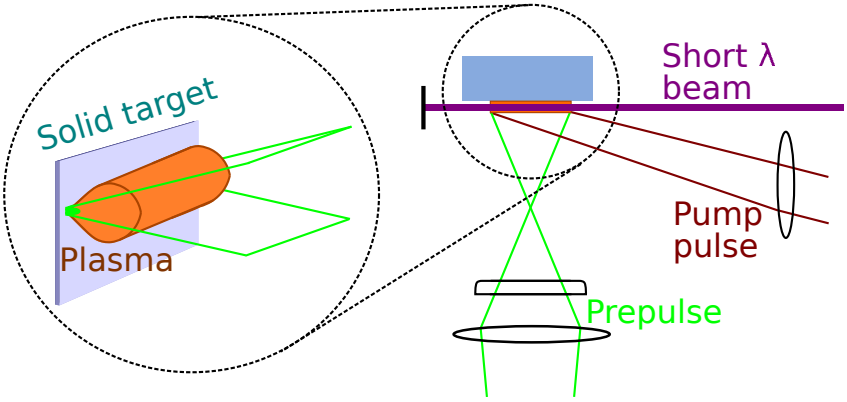

Figure 3: A typical experimental setup used to achieve lasing from solid density targets[29] located inside a vacuum chamber. A long initial optical prepulse is focused by a spherical and a cylindrical lens into a line at a solid slab target to create a plasma. A second, more intense pulse is then focused at a variable angle in order to create a population inversion.

A slightly alternative geometry used to produce a high aspect ratio plasma column from solid matter involves a microcapillary. A cylinder may be drilled into solid material, into which two co-propagating laser beams are sent. The first, long, low-power pulse is used to create an initial plasma as before; the second, intense pulse creates the population inversion. The microcapillary additionally acts as a waveguide for the resulting soft x-ray radiation.[31]

Element	Isoelectronic sequence	Transition	Photon energy [eV]	Reference
Nb	Ni	4d $^1S_0$ →4p $^1P_1$	60.7	[32]
Li	H	2p $^2P_0$ →1s $^2S_1$	91.8	[31]
Xe	Pd	5d $^1S_0$ →5p $^1P_1$	29.7	[30]
Ru, Pd, Ag	Ni	4d $^1S_0$ →4p $^1P_1$	75.1, 84.3, 89.2	[29]

Table 1: A review of the parameters of several experimentally achieved collisionally pumped soft x-ray lasers.

Collisionally pumped short wavelength lasers typically operate on transitions of closed-shell ions. Their ionization stages have relatively high ionization energies, which leads to a stability of the distribution of ionization stages over a large temperature and density range. Examples of experimental realisation of such collisionally pumped lasers are given in Table 1 in chronological order, showing progress towards higher photon energies and saturated laser output.

1.2.2 Capillary Discharge Lasers

The energy required to achieve the high ionization stages and population inversion for lasing may be delivered to a plasma by an electric current discharge. A successful scheme involves confining a low-density gas to be used as the gain medium in a ceramic capillary. The gas is first weakly ionized by a radio frequency (RF) discharge, which is widely used as an efficient method of plasma creation;[33] this greatly increases its electrical conductivity. A very high electrical current is quickly ramped up between electrodes at two ends of the plasma cylinder - it typically rises from 0 to $\sim$ 20 kA within tens of nanoseconds.[34] This current heats and further ionizes the plasma; it is large enough that the magnetic pressure due to the Lorentz force $\vec{F} = \vec{j} \times \vec{B}$ causes compression of the plasma column (similar to a z-pinch).

The plasma's compression is aided by temperature-driven pressure gradients, leading to a large increase in electron density. The plasma becomes quantitatively similar to that produced by optical pumping. Electron collisions strongly pump excited levels to produce a population inversion. The resultant laser beam is extremely collimated. It exits the chamber with the low-pressure gas, used as the gain medium, through a narrow pinhole. A high grade vacuum can then be maintained by differential pumping, so that the beam is not attenuated by neutral gas. The choice of gas as the gain medium and discharging capacitors as the energy delivery method allows high repetition rates to be achieved very reliably and cheaply.

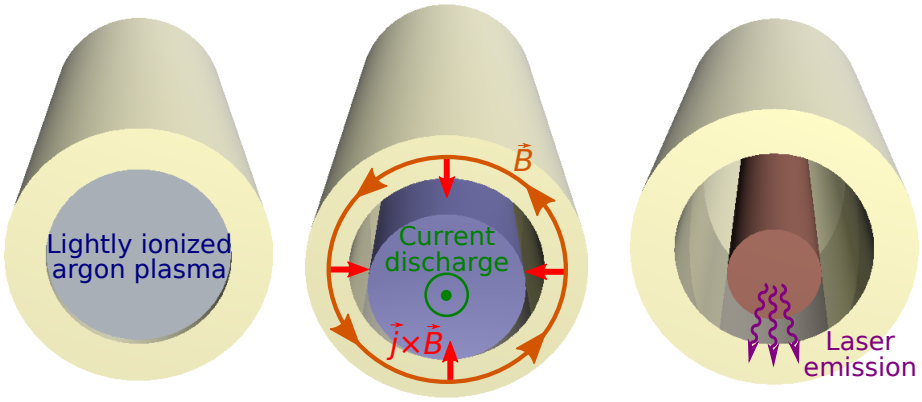

Figure 4: Schematic diagram of the lasing cycle of a typical capillary discharge laser. A ceramic capillary contains a gas which is lightly ionized by RF electrodes. A current is discharged, heating and compressing the plasma. Electron collisions create a population inversion and lasing occurs.

The relative ease with which capillary discharge lasers are able to operate motivates their continued development[35] and exploration of potential applications[36] in science and industry. One of the leaders in this field is the Engineering Research Center for Extreme Ultraviolet Science and Technology[37] at Colorado State University, with other contributing partners. As part of the work presented here, a collaboration has been undertaken to further develop argon-based capillary discharge lasers and conduct experiments with them; they are discussed further in §5.

1.2.3 X-ray Free-Electron Lasers

An accelerating charge radiates energy, whose power P is given for arbitrary motion by the relativistic Larmor formula,[38]

$$P = \frac{e^2\gamma^2}{6\pi\varepsilon_0 m^2 c^3}\left|\frac{dp_\mu}{dt}\frac{dp^\mu}{dt}\right|, \tag{19}$$

where the physical constants have their usual meanings, the relativistic factor $\gamma = (1 - v^2/c^2)^{-1/2}$ and p is the relativistic 4-momentum of the accelerating charge. This formula implies that a charge radiates more energy as its speed or acceleration increases. The special case of an accelerating charge in circular motion is usually referred to as synchrotron radiation; it limits the performance of such particle accelerators, since the particles experiencing a centripetal acceleration tend to radiate energy and decelerate. In this case, for a circle of radius r, the spectrum of radiation peaks at a photon energy $\epsilon_\gamma^{\mathrm{MAX}} \sim \gamma^3/r$. Therefore, this usually undesirable process

can be harnessed to generate arbitrarily short wavelength radiation. Specially-built synchrotron facilities, such as Diamond Light Source at the Rutherford Appleton Laboratory, have found a wide range of applications; however, such sources are not strictly lasers, because the radiation escapes tangentially before it is able to stimulate further emission.

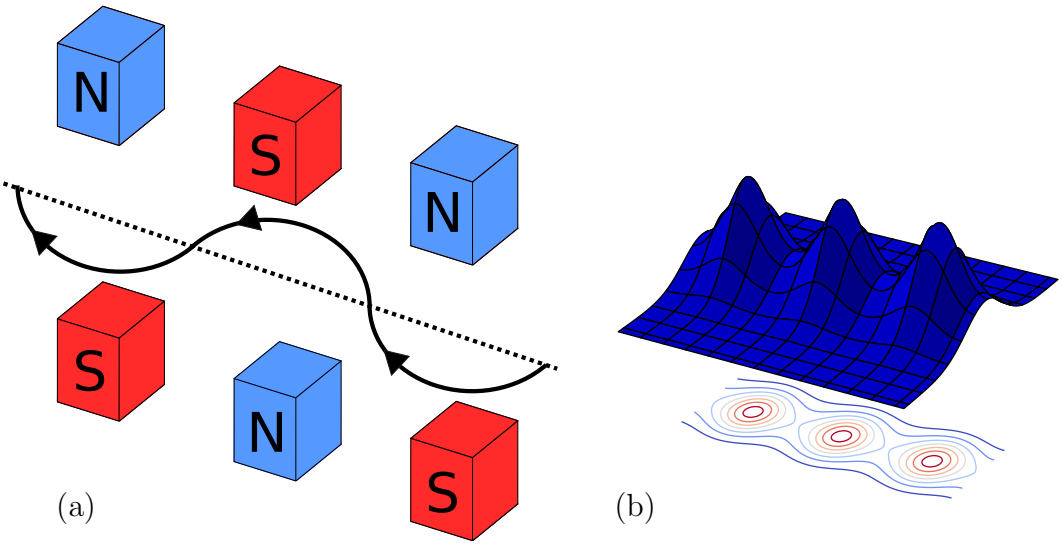

Figure 5: (a) Schematic diagram of an undulator, with the magnetic fields directed vertically and oscillation in the perpendicular plane. (b) Schematic diagram of microbunching. The electron density profile initially varies slowly in the direction of beam propagation, but coherent radiation causes wavelength-sized bunches to form as pictured.

Significant stimulated emission of synchrotron radiation (and therefore lasing) may be achieved if the radiation propagates along the same axis as the charged particles. This situation is realised by alternating magnetic fields in so-called undulators or wigglers, as shown in Figure 5a. Electrons from a conventional linear accelerator encounter regions of alternating field, so that although their bulk motion remains linear, they oscillate transversally. Self-amplified sponatneous emission occurs if the wavelength of emitted radiation λ_γ is resonant with the undulator period λ_u through the relation[39]

$$\lambda_\gamma = \frac{\lambda_u}{2\gamma^2}\left(1 + \frac{e^2 B^2 \lambda_u^2}{8\pi^2 (mc)^2}\right), \tag{20}$$

where B is the peak on-axis magnetic field. As a uniform electron bunch passes through the undulator, it begins to form microbunches spaced by λ_γ as shown in Figure 5b. As these microbunches develop, the coherent radiation is amplified exponentially until it reaches saturation, similarly to the gain of a conventional laser.

An undulator which is built specifically to create coherent beams of radiation in this way is termed a free-electron laser (FEL).

We see that the photon energy $\epsilon_\gamma = hc/\lambda_\gamma$ can be scaled up, into the x-ray range by increasing the γ factor; the current record of $\gamma \sim 2 \times 10^5$ is held by the Large Electron-Positron Collider.[40] Most FELs have fixed magnetic field strengths, but have accurate actuators to make microscale adjustments to λ_u to "tune" the output wavelength and to respond to the beam conditions.

Although free-electron lasers working in the x-ray range (XFEL) have only recently been demonstrated, there is a large scientific interest in their use. The largest currently operating XFEL is the Coherent Light Source at the Stanford Linear Accelerator.[41] The European XFEL[42] project is under construction in Hamburg as part of a collaboration of 11 countries.

1.2.4 Lasing without inversion

We have mentioned the large energy density required to obtain a population inversion. The pump power required for inversion depends on the broadening type, but typically scales as some large power of the laser's photon energy.[43] It would therefore be desirable to somehow create laser gain, without requiring to maintain a costly population inversion - the concept referred to as lasing without inversion (LWI). We see from Equation (17) that this would be achieved if the atoms in the lower level (with density N_1) were to be prevented from absorbing light. One proposed scheme envisions that atoms in the upper and lower lasing levels have motion relative to one another. This means that light emitted by the upper level is Doppler-shifted away from the absorption resonance in atoms of the lower levels; once they emit a photon, they recoil and are themselves shifted out of resonance.

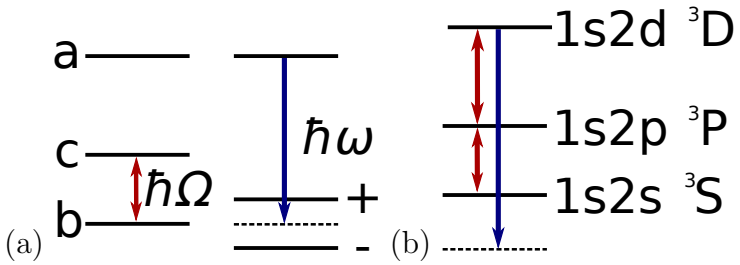

Figure 6: (a) A system with atomic levels a, b, c is perturbed by radiation with photon energy $\hbar\Omega$. This transforms the system to the basis a, $+$, $-$, and lasing can occur with photon energy $\hbar\omega$. (b) LWI proposal using a virtual energy level in helium[44] by driving Rabi oscillations between the levels shown.

Quantum coherence effects may be utilized to shift the atomic system from the usual basis (referred to as "bare") to a "dressed" basis. An external radiation field, typically from an optical laser, can drive detuned Rabi oscillations which introduce an asymmetry and shift to new basis, as sketched in Figure 6a. A scheme proposed to achieve lasing via virtual atomic levels[44] is shown diagramatically in Figure 6b. An Nd:YAG laser (λ =1064 nm) and its second harmonic can drive Rabi oscillations on the two transitions shown in helium (shorter-wavelength lasers can be used similarly in other atoms of the helium isoelectronic sequence). Transient amplification can then be achieved at λ = 266 nm. Although we do not discuss the full quantum mechanical treatment of LWI, the concept may allow increasingly intense, efficient or shorter-wavelength lasers to be produced.

2 Optical theory

The wavelike properties of light are important to the propagation, focusing and manipulation of laser beams, particular for wavelength-scale structures. Geometrical optics allows an intuitive model of light propagation on large scales, but fails to describe a laser beam's behaviour at its focus, the reflection from a structured multilayer and other interference effects. For example, light cannot be focused to a spot smaller than its diffraction limit, which is proportional to the photons' wavelength.[45] This motivates a wave optics approach to modelling EUV laser beams. This chapter outlines the mathematical background to this approach, gives examples of focusing optics and presents wave phenomena used in this work.

The Huygens-Fresnel principle states that each point on a propagating wavefront is the source of spherical waves. The wave amplitude at a point on a wavefront depends on the amplitude at every point on a previous wavefront. This is a natural consequence of Feynman's interpretation of quantum mechanics,[46] where particles explore all possible paths between two points. The "wave" in this case corresponds to the quantum mechanical concept of a wavefunction, whose modulus squared is the probability of detecting a particle. This accounts for the fact that the same integrated intensity profile is observed for a given number of photons, whether the photons have travelled in a tight nanosecond bunch or one by one over many years.

2.1 Fresnel diffraction

A beam of coherent light may be modelled by considering the propagation of a wave amplitude $u \in \mathbb{C}$ through space.[47] The corresponding intensity is given by $I(x, y, z) = P|u(x, y, z)|^2$, where P is the beam power. The wave amplitude u for a plane with co-ordinates x, y and the wave amplitude $\tilde{u}$ for a parallel plane a distance z away with co-ordinates $\tilde{x}, \tilde{y}$ are related by the Fresnel diffraction integral

$$\tilde{u}(\tilde{x}, \tilde{y}) = \mathcal{N} \int_{-\infty}^{\infty} \int_{-\infty}^{\infty} u(x, y) \frac{\exp(ik\rho)}{\rho^2} dx dy, \tag{21}$$

where $k = 2\pi/\lambda$ is the wavenumber of the light and ρ is the geometric distance from $(x, y, 0)$ to $(\tilde{x}, \tilde{y}, z)$; in Cartesian co-ordinates as above, $\rho^2 = (x - \tilde{x})^2 + (y - \tilde{y})^2 + z^2$. $\mathcal{N}(z)$ is a normalization factor to ensure energy conservation, which obeys the equation

$$\mathcal{N}^2 \int_{-\infty}^{\infty} \int_{-\infty}^{\infty} |\tilde{u}(\tilde{x}, \tilde{y})|^2 d\tilde{x} d\tilde{y} = 1. \tag{22}$$

In cylindrical polar coordinates the diffracted amplitude becomes

$$\tilde{u}(\tilde{r},\tilde{\theta}) = \mathcal{N}\int_0^{2\pi}\int_0^{\infty} u(r,\theta)\frac{\exp(ik\rho)}{\rho^2} r dr d\theta, \tag{23}$$

with $\rho^2 = \tilde{r}^2 + r^2 - 2r\tilde{r}\cos(\theta+\tilde{\theta}) + z^2$. This problem is usually analytically and computationally untenable for both co-ordinate systems due to the square root in the calculation of ρ for the exponential, unless it is expanded using a Taylor series

$$\rho \approx z + \frac{(x-\tilde{x})^2 + (y-\tilde{y})^2}{2z} + O(4) = z + \frac{\tilde{r}^2 + r^2 - 2r\tilde{r}\cos(\theta+\tilde{\theta})}{2z} + O(4), \tag{24}$$

where $O(4)$ refers to x^4 and other higher-order terms. This expansion is valid for $z \gg x, y$. It is convenient to drop all terms which do not depend on the two co-ordinates of the first plane, as in the exponent they naturally factor out of Equations (21) and (23) and introduce only a phase factor which does not affect the final intensity. Therefore, we define a reduced geometric distance to be used for the calculation of the complex exponential in the Fresnel integral,

$$\rho_- = \frac{x^2 + y^2 - 2x\tilde{x} - 2y\tilde{y}}{2z} = \frac{r^2 - 2r\tilde{r}\cos(\theta+\tilde{\theta})}{2z}. \tag{25}$$

2.1.1 1-Dimensional Case

The initial amplitude in Equation (21) may be symmetric in one of the Cartesian dimensions (*e.g.* y), such as for an infinitely long slit or grating. The integral over y in Equation (21) can then be factored out and with the transformation $y' = y - \tilde{y}$ becomes simply $\int_{-\infty}^{\infty}\exp(iky'^2/2z)dy' = \exp(i\pi/4)\sqrt{2\pi z/k}$, which is a normalization factor and a constant global phase.

The remaining integral can then be carried out keeping the x terms in the expansion in Equation (25), provided that z is sufficiently large. In particular, a further simplification can be made if the diffracted image is much larger than the source, and consequently $\tilde{x} \gg x$. Then, the term in x^2 can be dropped and the usual Fraunhofer diffraction equation emerges,

$$\tilde{u}(\tilde{x}) = \mathcal{N}\int_{-\infty}^{\infty} u(x)\exp\left(-ik\frac{x\tilde{x}}{z}\right)dx = \mathcal{F}[u(x)], \tag{26}$$

where $\mathcal{F}$ is the Fourier transform. It is typically carried out numerically by a Fast Fourier Transform algorithm, as discussed in Appendix B.5.

Of great interest is an amplitude which is symmetric in θ around the propagation axis, such as a circular beam being focused by a lens on axis. Equation (23) may

then be simplified by the substitution $\theta' = \theta + \tilde{\theta}$ and the two terms in the exponential from Equation (25) may be treated separately;

$$\tilde{u}(\tilde{r}) = \mathcal{N} \exp\left(ik\left[z + \frac{\tilde{r}^2}{z}\right]\right) \int_0^\infty r u(r) \exp\left(ik\frac{r^2}{2z}\right) \int_0^{2\pi} \exp\left(-ik\frac{r\tilde{r}\cos(\theta')}{z}\right) d\theta' dr. \tag{27}$$

The angular integral is a standard form known as Bessel's first integral,[48]

$$\int_0^{2\pi} \exp\left(\pm i\xi\cos\theta'\right) d\theta' = 2\int_0^{\pi} \exp\left(\pm i\xi\cos\theta'\right) d\theta' = 2\pi J_0(\xi), \tag{28}$$

where $J_0(\xi)$ is the zeroth Bessel function of the first kind. Equation (27) then reduces to

$$\tilde{u}(\tilde{r}) = \mathcal{N} \int_0^\infty \left[r u(r) \exp\left(ik\frac{r^2}{2z}\right)\right] J_0\left(k\frac{r\tilde{r}}{z}\right) dr. \tag{29}$$

This amounts to the so-called Hankel transform[49] of the function in square brackets, which is the radially symmetric version of the Fourier transform commonly associated with diffraction patterns using $J_0(x)$ instead of $\exp(ix)$ as the basis function.

2.1.2 2-Dimensional Case

We aim to simulate an optical element inclined at an angle α to the axis of propagation of a circular beam, therefore breaking the angular symmetry. In order to define ρ and make any suitable approximations, we begin for simplicity in Cartesian co-ordinates and then transform to polars. The point P_1 with co-ordinates $(X_1, Y_1, 0)$ lies in the starting plane, which has an origin at O_1 and the usual polar co-ordinate system. The point P_2 with co-ordinates (X_2, Y_2, Z_2) and origin at O_2 lies on the focal plane. The geometric distance ρ obeys

$$\rho^2 = (X_2 - X_1)^2 + (Y_2 - Y_1)^2 + Z_2^2. \tag{30}$$

O_2 is a distance z along a line that is inclined at an angle 2α to the normal of the starting plane. The focal plane is also inclined at an angle β to the starting plane; the focal plane would be normal to the new propagation axis if $\beta = 2\alpha$, but is allowed to vary to match experimental conditions. As illustrated in Figure 7, this leads to the co-ordinate transformations in Table 2.

Substituting the transformations into Equation (30), we obtain

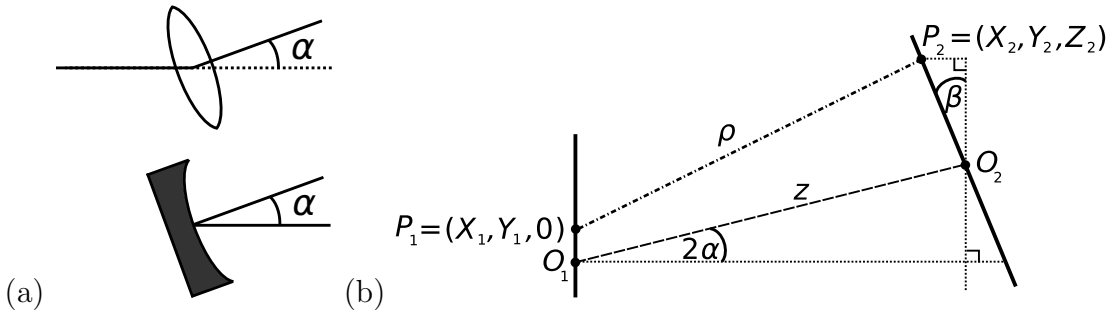

Figure 7: (a) An example of a single focusing optic at an angle α to the propagation axis. In the case of a curved mirror, it is possible to "unroll" the optical system to be equivalent to the transmissive optic, pictured above. (b) The co-ordinate system for diffraction through the optical system.

Cartesian	Polar
X_1	$r\cos\theta$
Y_1	$r\sin\theta$
X_2	$\tilde{r}\cos\tilde{\theta}\cos\beta + z\sin(2\alpha)$
Y_2	$\tilde{r}\sin\tilde{\theta}$
Z_2	$z\cos(2\alpha) - \tilde{r}\cos\tilde{\theta}\sin\beta$

Table 2: Co-ordinate transformations for the off-axis focusing optic.

$$\begin{aligned}\rho^2 =&\tilde{r}^2\cos^2\tilde{\theta}\cos^2\beta + 2\tilde{r}z\cos\tilde{\theta}\cos\beta\sin(2\alpha) - 2r\tilde{r}\cos\tilde{\theta}\cos\theta\cos\beta - 2rz\cos\theta\sin(2\alpha)\\ &+z^2\sin^2(2\alpha)+r^2\cos^2\theta+\tilde{r}^2\sin^2\tilde{\theta} - 2r\tilde{r}\sin\tilde{\theta}\sin\theta+r^2\sin^2\theta+z^2\cos^2(2\alpha)\\ &-2\tilde{r}z\cos\tilde{\theta}\cos(2\alpha)\sin\beta + \tilde{r}^2\cos^2\tilde{\theta}\sin^2\beta,\end{aligned} \tag{31}$$

where elements highlighted in red do not depend on the initial co-ordinates and those highlighted in blue can be readily factorised using $\sin^2 x + \cos^2 x \equiv 1$. We find the reduced geometric distance ρ_-, similarly to Equation (25), by taking the first-order Taylor approximation to the square root ($z \gg r$) and then discarding z and those parts shown in red. We therefore have for the reduced geometric distance

$$\rho_- = \frac{r^2}{2z} - r\cos\theta\sin(2\alpha) - \frac{r\tilde{r}}{z}\left[\cos\tilde{\theta}\cos\theta\cos\beta + \sin\tilde{\theta}\sin\theta\right], \tag{32}$$

which reduces to the 1-Dimensonal case for $\alpha, \beta = 0$. When calculating the diffraction pattern in this case, the focal spot or some element of interest may be shifted away from the origin O_2. To offset the pattern, for example along the $\tilde{x}$ axis, we replace $\tilde{r}\cos\tilde{\theta} \to \tilde{r}\cos\tilde{\theta} + x_0$ in Equation (32), but leave all other terms unchanged, or *vice versa* for $\tilde{y}$.

To solve the diffraction integrals described above, a code called `SAFE2DIP`: Simple Algorithm for FrEsnel diffraction 2 DImensional Polar has been written as part of this work. Discretising the $(\tilde{r}, \tilde{\theta})$ plane and computing a double integral at each point is readily parallelised and can be easily carried out over the dozens of threads normally available on a modern CPU cluster. Specifically, the code is written in `C` and parallelised with `OpenMP`. For computational stability, the complex exponential $\exp(ik\rho_-)$ is split into a product of three exponential components, one for each term in Equation (32).

Interest in numerical computation of the Fresnel integrals of the type $\int \cos[\cos(x)]\, dx$ has begun in the 1950s.[50] The integrals above can be carried out numerically using a Newton-Cotes type formula, with the necessary number of nodes found to be given by $0.025(\tilde{r} - 10\ \mu\text{m})$. By performing numerical experiments, we find that in this case the complexity of the Clenshaw-Curtis method is not justified in achieving a significant speed up. For this type of integral, Ehrenmark[51] suggests the modified Newton-Cotes type formula

$$\int_{x_1}^{x_2} f(x)dx = Af(x_1) + Bf\left(\frac{x_1 + x_2}{2}\right) + Af(x_2), \tag{33}$$
$$A = \frac{x_2 - x_1 - \frac{1}{\omega}\sin[(x_2 - x_1)\omega]}{2(1 - \cos[(x_2 - x_1)\omega])},$$
$$B = x_2 - x_1 - 2A,$$

where ω is taken at each step to be half the average argument of the trigonometric component of $f(x)$ between x_1 and x_2. For instance, when evaluating $\int_a^b \cos[f(x)]dx$ for $f(a) = 2$ and $f(b) = 4$, the value $\omega = 3$ may be chosen in evaluating Ehrenmark's formula.

Evaluating integrals via a summation of very many terms can lead to floating point errors. One simple algorithm for reducing these rounding errors due to Kahan[52] takes advantage of the fact that addition is not commutative on computers. Care must be taken to ensure that the compiler used is not overly aggressive in implementing commutative simplifications.

Several examples of `SAFE2DIP` calculations are shown in Figure 8, for increasing curved mirror tilt angles. The profile is symmetric in the case $\alpha = \beta = 0$, and we observe good agreement with a 1-dimensional code solving Equation (29); the latter has also been successfully compared to an online resource.[53] We see that the increasing tilt angle leads to a spreading of the focal spot. In all three plots, the intensity is scaled with respect to its maximum value, although the absolute value of this maximum decreases as the tilt angle is increased. In each case, a value of the

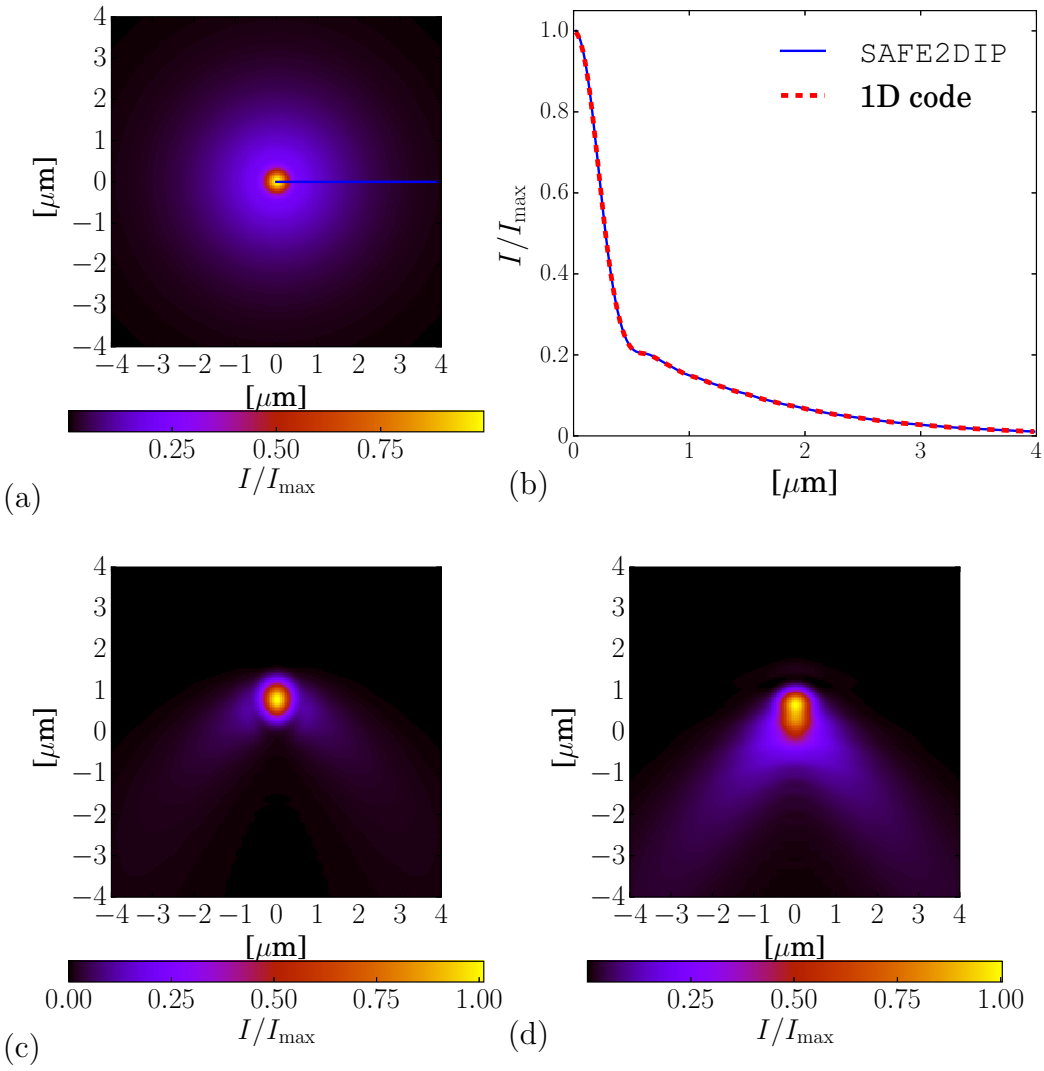

Figure 8: Results from SAFE2DIP calculations for a capillary discharge laser with a wavelength of 46.9 nm reflected by a curved multilayer mirror, as discussed in Chapter 5. The angles are (a) $\alpha = \beta = 0°$; (c) $\alpha = 2°$, $\beta = 4°$; (d) $\alpha = 3°$, $\beta = 6°$. A line out (b) from the centre of the radially symmetric case (as shown) is compared to a 1 dimensional code.

offset x_0 has been chosen so that the peak is approximately centered.

It is important to note that the scale of diffraction patterns is set by the wavelength of light in question through its relation to the wavenumber, $\lambda = 2\pi/k$. For example, the smallest features of diffraction patterns and therefore the diffraction limit of optical instruments have a size comparable to the wavelength. This has important implications for working with short wavelength radiation, because the margins of error on the positioning of optics are correspondingly much smaller than for visible light.

2.2 Multilayer Mirrors

The refractive index of solids and plasmas is generally complex, where the real part corresponds to the usual wave slowing and the imaginary part corresponds to an opacity. It is usually referred to in the literature in terms of β and δ coefficients,

$$\tilde{n} = 1 - \delta + i\beta, \tag{34}$$

where β is sometimes also called the extinction coefficient (and may confusingly be labelled k). Refraction at the interface of two regions of refractive index, $\tilde{n}_1$ and $\tilde{n}_2$, is governed by a generalised version of Snell's law (if the electromagnetic wave remains transverse[54,55])

$$\tilde{n}_1 \sin\tilde{\eta}_1 = \tilde{n}_2 \sin\tilde{\eta}_2, \tag{35}$$

where $\tilde{\eta}_1, \tilde{\eta}_2 \in \mathbb{C}$. The geometric angles made by the rays with the normal are given by $\eta = \mathrm{Re}\{\tilde{\eta}\}$.

At the interface of two media with different refractive indices, reflection and transmission is governed by similarly complex versions of the usual Fresnel equations. The reflection amplitude coefficient for waves with perpendicular and parallel polarization relative to the plane of incidence are given respectively by[45]

$$\mathfrak{r}_{\perp,\parallel} = \frac{\tilde{n}_{1,2}\cos\tilde{\eta}_1 - \tilde{n}_{2,1}\cos\tilde{\eta}_2}{\tilde{n}_1\cos\tilde{\eta}_{1,2} + \tilde{n}_2\cos\tilde{\eta}_{2,1}}. \tag{36}$$

The total reflectance (for intensity, rather than the wave amplitude) is given by $\mathtt{R} = |\mathfrak{r}|^2$. A similar expression exists for the transmission amplitude coefficient $\mathfrak{t}$ and transmittance $\mathtt{T} = 1 - \mathbb{R}$.

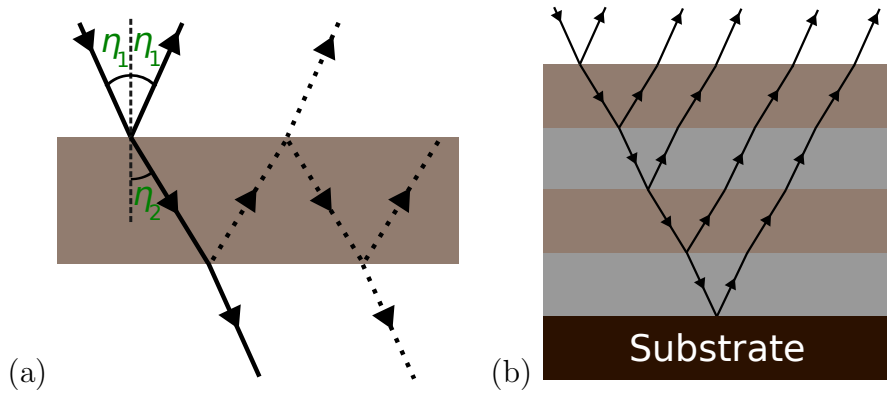

(a) (b)

Figure 9: (a) A medium of refractive index $\tilde{n}_2$ immersed in a medium with index $\tilde{n}_1$, showing the repeated reflections between the interfaces. (b) Reflections from a multilayer stack of refractive slabs, terminating at an opaque substrate.

A multilayer mirror is constructed by stacking successive compounds of alternating refractive indices, so that small reflections from each interface sum to a large reflectivity. In addition to the transmission and reflection coefficients, each layer of thickness z adds a phase factor of $\exp(2ik\tilde{n}z\cos\eta)$ to the propagating wave. Reflections of this type occur between high-low and low-high refractive boundaries, which implies that a wave incident on a slab of index $\tilde{n}_2$ "sandwiched" between slabs of index $\tilde{n}_1$ will continuously be reflected between the two boundaries as shown in Figure 9a, with decreasing amplitude; this is modelled by the use of the formula for an infinite geometric sum.

The software package `IMD`[56] solves Equations (34) to (36) for a user-specified stack of refractive layers, to obtain the reflectance, phase and many other parameters as a function of polarization, wavelength and incidence angle. It contains a comprehensive library of materials, also allowing extrapolation outside of the known parameter range and user-specified optical properties. The software is freely available, but requires the licensed IDL language to be installed.[57]

2.3 Talbot patterns

Suppose that the amplitude in Equation (21) at $z = 0$ is uniform in y and periodic in the x dimension, so that it is defined on the interval $\{x \in \mathbb{R} | 0 \leq x < b\}$ and then repeats itself infinitely in both directions. It can then be represented by a Fourier series, such that[58]

$$u(x) = \sum_m A_m \exp\left[2\pi i \left(\frac{mx}{b}\right)\right], \tag{37}$$

where $m \in \mathbb{Z}$ and A_m are the Fourier coefficients. The sum runs to infinity, but we truncate it at some value M, which effectively makes the function $u(x)$ discrete at points spaced by b/M. By carrying out the integral in Equation (21) with the paraxial approximation $\rho \approx z + \frac{1}{2z}(x - \tilde{x})^2$, the wave amplitude becomes

$$\tilde{u}(\tilde{x}) = \sum_m A_m \exp\left[i\pi\lambda z \left(\frac{m^2}{b^2}\right)\right] \exp\left[2\pi i \left(\frac{m\tilde{x}}{b}\right)\right], \tag{38}$$

where the global phase prefactor has been dropped as usual. If z is set to the so-called Talbot distance

$$z_T = \frac{2b^2}{\lambda}, \tag{39}$$

the first exponential in Equation (38) becomes $\exp(2\pi i m^2) = 1$, since m and hence m^2 are integers. This means that the same wave amplitude repeats every Talbot distance.

To calculate the wave amplitude up to the first Talbot distance, the sum in Equation (38) can be recast as an inverse discrete Fourier transform of the Fourier coefficients and the quadratic phase coefficients. If $\tilde{x}$ is discretised on the same grid as x, so that $\tilde{x} = pb/M$, Equation (38) becomes

$$\begin{aligned}\tilde{u}_p &= \sum_m A_m \exp\left[i\pi\lambda z\left(\frac{m^2}{b^2}\right)\right]\exp\left[2\pi i p m/M\right] \\ &= \mathcal{F}^{-1}\left\{A_m \exp\left[i\pi\lambda z\left(\frac{m^2}{b^2}\right)\right]\right\}. \end{aligned} \tag{40}$$

The resulting wave amplitude at distance z can then be calculated through the simple algorithm:

Define u

$\downarrow$

Calculate $\mathcal{F}$

$\downarrow$

Multiply element m by $\exp[i\pi\lambda z m^2/b^2]$

$\downarrow$

Calculate $\mathcal{F}^{-1}$

This approach can be readily extended to two dimensions by defining $u(x, y)$ on a square interval of length b, using two-dimensional Fourier routines and adding a factor $\exp[i\pi\lambda z n^2/b^2]$ to Equation (40) for the y dimension.

The 1-dimensional approximation is valid only if there is very little variation far into the y dimension, while also repeating sufficiently many times in x. This effect is named after Talbot,[59] who first observed it for diffraction gratings. It is common to plot the intensity as a function of x and z to produce a so-called "Talbot Carpet", as shown in Figure 10. The figure shows that not only does the pattern repeat at $z = z_T$, but it also repeats, albeit with a linear shift, at $z_T/2$ and appears scaled at other integer multiples of the Talbot distance.

In the 2-dimensional case, a sufficient number of apertures must be illuminated in both dimensions in order for the diffraction pattern to approach the idealised Talbot pattern. With a finite number of apertures, the wave amplitude deviates from the

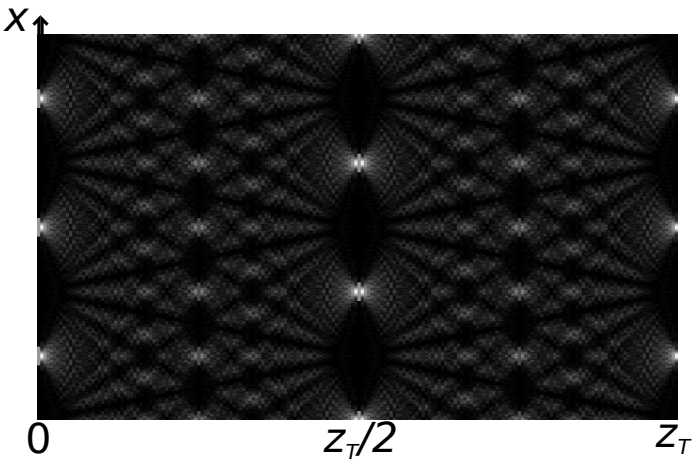

Figure 10: Relative intensity of diffracted light from an infinite array of slits repeating in the x direction (three are shown) at successive planes in the z direction. This type of plot is a so-called "Talbot Carpet". This figure has been created using the algorithm presented in this section.

Talbot pattern with increasing z. Nonetheless, with a grid of approximately 10×10 apertures, a Talbot pattern is produced at the first Talbot distance.

Talbot patterns which contain the requisite number of apertures are resilient to point defects in the initial mask. In this case, the initial wave amplitude is given by $u_0 + u_1$, where u_0 is the idealised periodic amplitude of Equation (37) and u_1 is a perturbation localised to one or more of the apertures. Diffraction is linear, so we consider the two components individually; $\tilde{u}_0$ is the familiar Talbot pattern, while $\tilde{u}_1$ is divergent and hence this wave amplitude decreases with propagation distance. Therefore, the final wave amplitude tends to $\tilde{u}_0$ and the perturbation decays away, provided that it is small compared to the repeating pattern.

Printing 2-dimensional structures using EUV lasers has shown the above resilience to imperfections experimentally.[60] For example, a fairly severe 1% deviation was introduced by intentionally replacing several apertures with "incorrect" shapes. The image at the first Talbot distance showed no signs of the defects. Moving to further Talbot planes has also been verified to improve the final profile.

2.4 Focusing optics

Most types of glass and crystals typically used for optical applications are transmissive for photon energies < 8 eV.[61] For most EUV applications, the photoionization cross section makes it impossible to use refractive optics due to the high corresponding absorption. In fact, solid refractive optics are used to focus x-rays above

approximately 5 keV, where the photoionization cross section drops sufficiently not to absorb the majority of the beam or become destroyed by a single shot. The refractive index in this photon energy range is extremely close to unity, so stacks of hundreds of single parabolic lenses are assembled into a Compound Refractive Lens (CRL); beryllium CRLs have been successfully used to focus 8.2 keV photons at LCLS.[62]

Here, we discuss the challenging approaches to efficiently focus EUV radiation to intensities sufficient to ablate material or create warm dense matter. Multilayer mirrors are able to reflect normally incident light in the EUV region; several curved geometries may be exploited. Grazing incidence mirrors are extremely efficient to high photon energies, therefore suitable to be used to transfer beams and also focus. Crystals which "reflect" x-rays at grazing angles by the Bragg process (in fact a type of diffraction) are used as optical elements in x-ray spectroscopy, but are not discussed here. If reflection is not possible or undesirable, diffraction effects may also be used to focus light over a wide range of wavelengths down to the EUV and soft x-ray, provided that the optical material absorbs the radiation sufficiently well to create an appropriate aperture. A Fresnel zone plate (FZP) is an example of such an aperture and is described below.

Regardless of its type, the distances of an object and image (u and v respectively) created by a thin focusing optic of focal length f obey the equation

$$\frac{1}{u} + \frac{1}{v} = \frac{1}{f}. \tag{41}$$

With the wave amplitude formulation of light propagation, the phase variation imparted on a beam by an optic is the parameter responsible for focusing. A wave expanding from a point has a spherical wavefront; consequently, to focus light to a point, a converging spherical phase must be imparted to it. Equation (41) can be seen to represent an initial wave with expanding radius u transformed into a final wave with converging radius v by an optic of focal length f.

2.4.1 Curved Mirrors

Arrangements of mirrors can focus light by introducing a path difference and hence phase shift based on their shape. The simplest possible focusing element is a single concave spherical mirror, placed and centred on the optical axis. For a beam propagating along the z-axis, a spherical mirror aligned with the axis and with a radius of curvature R_c has a surface given by the equation $x^2 + y^2 + z^2 = R_c^2$. If

the mirror is tilted by an angle α in, for example, the x direction, we can transform the co-ordinate system using the usual rotation matrix to give $x = x' \cos\alpha - z' \sin\alpha$ and $z = z' \cos\alpha + z' \sin\alpha$. Transforming to polar co-ordinates, we have the phase change due to a spherical mirror with transverse radius R_m given by

$$u_{ref}(r,\theta) = \exp(-2ik\sqrt{R_c^2\cos^2\alpha - r^2 + 2R_c r\cos\theta\sin\alpha})\Theta(r - R_m)u_0(x,y), \quad (42)$$

where Θ is the Heaviside step function.

The inherent problem of a single such mirror is that the beam must propagate backwards along the original axis ($\alpha = 0$), or face a large astigmatism due to the $2R_c r\cos\theta\sin\alpha$ term. It also requires reflectance at normal incidence, which is not possible or efficient for all wavelengths. For $\alpha \neq 0$, an extra dimension as detailed above and hence significant additional computing power are required for theoretical calculations. On the other hand, with only a single focusing element the reflective losses, cost and setup time are minimised. Note that due to the law of reflection, the optical axis in this case tilts by 2α.

In the case of a multilayer mirror, the angle of incidence η determines the reflectance $\mathtt{r}$ and the additional phase factor ϕ_{MLM} introduced by the multilayer, adding two additional factors to Equation (42),

$$u_{MLM} = \exp(i\phi_{MLM}(\eta))\mathtt{r}(\eta)u_{ref}. \quad (43)$$

To determine the angle η, we note that the 2-dimensional surface of a mirror is defined by its height relative to the z axis, as $z = f(x,y)$, and so a vector perpendicular to each tangent plane is given by

$$\vec{N} = \begin{pmatrix} \frac{\partial f}{\partial x} \\ \frac{\partial f}{\partial y} \\ -1 \end{pmatrix}. \quad (44)$$

Taking the scalar product, which gives the product of the magnitudes of two vectors with the cosine of the angle between them, with the negative unit vector $-\vec{e}_z = (0,0,-1)^T$ results in

$$\begin{aligned} 1 &= \cos(\eta)|\vec{N}| \\ &= \cos(\eta)\sqrt{\left(\frac{\partial f}{\partial x}\right)^2 + \left(\frac{\partial f}{\partial y}\right)^2 + 1}. \end{aligned} \quad (45)$$

After rearranging to isolate the cosine term and transforming using the trigonometric identity $\arccos(1/\sqrt{a+b+1}) \equiv \arctan(\sqrt{a+b})$, we have

$$\tan(\eta) = \sqrt{\left(\frac{\partial f}{\partial x}\right)^2 + \left(\frac{\partial f}{\partial y}\right)^2}. \tag{46}$$

If the surface is defined in cylindrical polar co-ordinates, $z = f(r, \theta)$, then Equation (46) may be transformed using the relation

$$\left(\frac{\partial f}{\partial x}\right)^2 + \left(\frac{\partial f}{\partial y}\right)^2 = \left(\frac{\partial f}{\partial r}\right)^2 + \frac{1}{r^2}\left(\frac{\partial f}{\partial \theta}\right)^2. \tag{47}$$

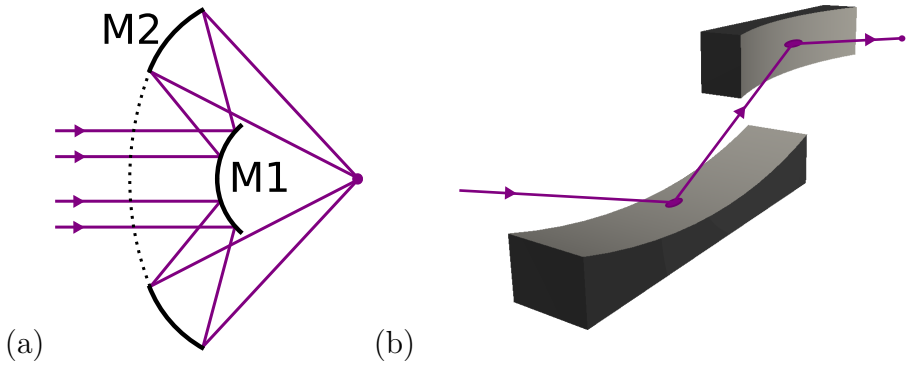

Figure 11: (a) Schwarzschild mirror pair focusing a collimated beam. (b) Kirkpatrick-Baez grazing-incidence mirror pair.

In order to overcome the astigmatism due to the asymmetry of the single tilted spherical mirror, two may be used to form Schwarzschild mirror pair as shown in Figure 11a. Passing through a hole in the spherical mirror M2, the beam is incident onto a smaller mirror M1. A "doughnut" profile is reflected by the first spherical mirror M1 onto the second mirror M2. As a drawback, a central circular part of the profile is not transmitted and part of the remaining beam is occluded by a supporting structure for the first mirror, which intersects the beam. The addition of a second mirror may unfavourably lower the total energy on target, if the reflectivity at the desired wavelength is low. However, the idealised setup has angular symmetry, which is largely unbroken by the addition of the supporting structure for the first mirror, allowing a small focal spot to be achieved and simplifying simulations.

In the case where normal-incidence reflectivities are too low, such as for x-rays, a pair of grazing-incidence Kirkpatrick-Baez mirrors may be used to focus the beam. The mirrors are orientated at 90° and each curved mirror focuses in one direction. The setup is pictured schematically in Figure 11b.

2.4.2 Fresnel zone plates

In the cases where reflective optics are not possible or undesirable, it is possible to focus light by diffracting it through a carefully chosen aperture. From Equation (23), consider the on-axis (with $\tilde{r} = 0$ and therefore θ-symmetric) diffraction pattern at a distance f away from a uniformly illuminated ($u = 1$) circular aperture,

$$\tilde{u}(0) \propto \int_0^\infty r \frac{\exp(ik\rho)}{\rho^2} dr, \tag{48}$$

where the path length $\rho = \sqrt{f^2 + r^2}$ takes a minimum at $\rho_0 = f$. The complex exponential in the integrand oscillates with increasing r from positive to negative, leading mostly to cancellations in the final integral. In particular, the sign of the integrand changes with increasing path length every $\lambda/2$; these regions of alternating phase are termed Fresnel Zones. Applying this condition to find the radius of the m^{th} zone ($m \in \mathbb{R}$), we have that

$$\rho_m = \rho_0 + \frac{m\lambda}{2} \tag{49}$$

$$\sqrt{f^2 + r_m^2} = f + \frac{m\lambda}{2} \tag{50}$$

$$r_m = \sqrt{m\lambda f + \frac{(m\lambda)^2}{4}}. \tag{51}$$

The intensity $I = |\tilde{u}|^2$ can be maximised, and therefore light can be focused, if either the positive (from m even to $m + 1$) or negative (from m odd to $m + 1$) component is filtered out. An example is shown in Figure 12(a), where regions of negative and positive phase are coloured black and white respectively. The area between any two zones $\pi(r_m^2 - r_{m-1}^2) = \pi(\lambda f + (2m - 1)\lambda^2/4)$ is approximately independent of zone number and hence the total positive and negative areas are approximately equal. Therefore, a zone plate transmits 50% of incident light.

For a given wavelength and focal length, there is a limit to the possible size of a Fresnel zone plate; as the zone widths continue to decrease, the technological limit of a manufacturing technique is reached. To estimate the total size of an FZP with N zones and an outer zone width of Δr, we have

$$\begin{aligned} \Delta r \equiv r_N - r_{N-1} &\approx \sqrt{N\lambda f} - \sqrt{N\lambda f}\sqrt{1 - \frac{1}{N}} \\ &\approx \frac{r_N}{2N}, \end{aligned} \tag{52}$$

where we have kept the first two terms of the Taylor expansion of the square root.

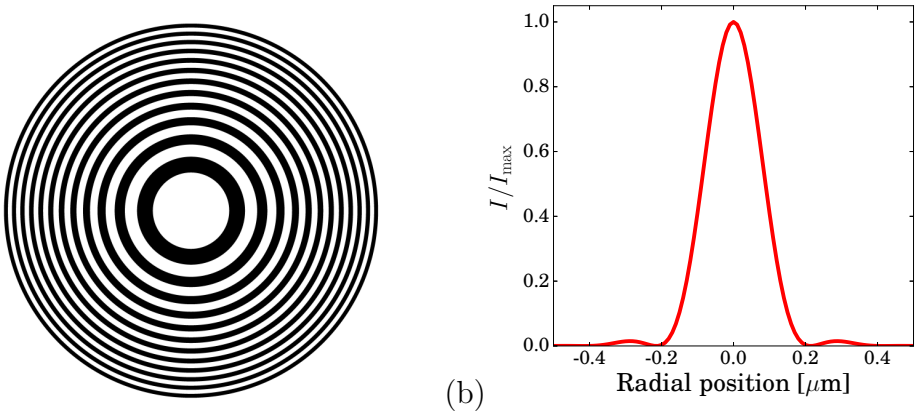

Figure 12: (a) A Fresnel zone plate, where the alternating black and white regions may be equivalently either transmitting or absorbing. (b) The normalised intensity profile at the focal point, with uniform illumination of the zone plate by 46.9 nm light.

The geometric approach ignores the ρ^{-2} factor in Equation (48). We can find more accurate expressions for the zone radii by calculating the intensity from the full diffraction integral up to some arbitrary radial point,

$$\begin{aligned} I(R) &= \left| \int_0^R r \frac{\exp\left(ik\sqrt{f^2+r^2}\right)}{f^2+r^2} dr \right|^2 , \\ &= \left[\int_f^{\sqrt{f^2+R^2}} \frac{\sin kt}{t} dt \right]^2 + \left[\int_f^{\sqrt{f^2+R^2}} \frac{\cos kt}{t} dt \right]^2 , \end{aligned} \tag{53}$$

where we have used Euler's formula and the substitution $t = \sqrt{r^2+f^2}$. We have integrated from $r = 0$, the radius of the zeroth Fresnel zone, so we expect that $I(R)$ will grow with R until r_1 due to a positive contribution to the integral, then decrease until r_2, *etc.* Therefore, the maxima and minima of $I(R)$ correspond to negatve and positive zone radii respectively. These stationary points can be found as usual by finding the roots of $\frac{dI}{dR}\big|_{R=r_m}$, which we evaluate by exploiting the standard rules of definite integrals, obtaining

$$\left.\frac{dI}{dR}\right|_{R=r_m} = \frac{2r_m}{f^2+r_m^2} \int_f^{\sqrt{f^2+r_m^2}} \frac{\sin kt \sin(k\sqrt{f^2+r_m^2}) + \cos kt \cos(k\sqrt{f^2+r_m^2})}{t} dt. \tag{54}$$

We can simplify this by discarding the prefactor, using the identity $\sin A \sin B + \cos A \cos B \equiv \cos(B-A)$ and with the parameterization

$$r_m = \sqrt{b_m^2 - f^2}, \tag{55}$$

where b_m is the m^{th} root of

$$\Delta(x) = \int_f^x \frac{\cos(k[x-t])}{t} dt. \tag{56}$$

By performing numerical experiments for $f \gtrsim 100\lambda$, we confirm that r_m calculated through Equations (51) and (55) agree to better than 0.1%. The former, geometric, equation may therefore be used to bracket the roots of the latter to carry out Brent's algorithm (discussed in Appendix B.4).

3 Thermodynamic properties of plasmas

A sufficiently large plasma (consisting of $> 10^{10}$ particles) can be regarded as a macroscopic thermodynamic system. The second law of thermodynamics states that the entropy of such systems must tend to increase over time.[63] As a consequence, such plasmas tend to redistribute their internal energy to reach an equilibrium, which is typically described by a temperature.

Different populations in a plasma, such as electrons, ions and photons, redistribute their kinetic energy by means of collisions to reach a corresponding energy distribution function, several of which are discussed below. These populations also exchange energy with the bound electrons of ions, interacting with their potential energy; particle number may not be conserved in such interactions, for example as electrons or photons may be captured by the ions. The atomic processes in such interactions and their rates are discussed in this chapter.

By assuming equilibria in the calculation of plasma properties, many theoretical models can be significantly simplified. Properties of a system in equilibrium can be determined from the state of the system at a given time, without needing to take the system's history into account. While such assumptions can greatly speed up and simplify calculations, they require that the time to reach equilibrium be sufficiently shorter than other timescales of interest. The types of thermodynamic equilibria in plasmas and their applicability are discussed in this chapter.

3.1 Energy distribution functions

The motion of particles in a thermodynamic system can be characterised by a statistical velocity distribution $\mathbb{F}(v)dv$ or kinetic energy distribution $f(\epsilon)d\epsilon$; these correspond to particles moving with speeds from v to $v + dv$ and with kinetic energies from ϵ to $\epsilon + d\epsilon$. As with any probability distribution, it is possible to calculate expectation values (referred to as "moments" in this case), defined for some function X as

$$\langle X \rangle = \int_0^\infty X f(\epsilon) d\epsilon. \tag{57}$$

Usually, the moments for a polynomial X are numbered after the power. For any distribution to be a true probability distribution function it must be normalised, and hence we require that the zeroth moment satisfy $\langle 1 \rangle = 1$.

The first moment of the energy distribution is the expectation value of energy, *i.e.* the average kinetic energy of a particle. In this work, we define this as the total

heat capacity of a system of particles,

$$C_V = \langle \epsilon \rangle. \tag{58}$$

The total kinetic energy density ε of such a system (in units of eV cm^{-3}) is then this average energy multiplied by the density of particles: $\varepsilon = NC_V$. Pressure is defined as the flux of momentum p per unit surface area,

$$P = \frac{N}{3} \int_0^\infty vpf(p)dp = \frac{N}{3} \int_0^\infty 2\epsilon f(\epsilon) d\epsilon \tag{59}$$

$$= \frac{2}{3} N \langle \epsilon \rangle, \tag{60}$$

where we have used $\epsilon = p^2/2m$, which holds for nonrelativistic particles, as discussed below.

3.1.1 Maxwell-Boltzmann distribution

In the absence of external forces and if the density of particles and energy is low enough that relativistic and quantum effects can be ignored, a system tends to the Maxwell-Boltzmann distribution in steady state. For particles of mass m at a temperature T, the Maxwell-Boltzmann velocity distribution function is given by

$$\mathbb{F}_{MB}(v, T)\, dv = \sqrt{\frac{2}{\pi}} \left(\frac{m}{T}\right)^{3/2} v^2 \exp\left(-\frac{mv^2}{2T}\right) dv, \tag{61}$$

and the energy distribution by

$$f_{MB}(\epsilon, T)\, d\epsilon = \frac{2}{\sqrt{\pi}} \frac{\sqrt{\epsilon}}{T^{3/2}} \exp\left(-\frac{\epsilon}{T}\right) d\epsilon. \tag{62}$$

The velocity distribution is plotted in Figure 13, showing the characteristing way in which the peak and spread of the distribution increases with temperature. Differentiating the function $\mathbb{F}_{MB}(v)$, we find it peaks at $v = \sqrt{2T/m}$; this is therefore the most probable particle speed. The first moment from Equation (58) gives the Maxwell-Boltzmann heat capacity

$$C_V = \frac{3}{2} T. \tag{63}$$

This leads also to the equation of state of an ideal gas, $p = NT$.

It is clear that $\mathbb{F}_{MB}(v)$ is non-relativistic, as there is a finite probability of having $v > c$. However, even for a modestly high plasma temperature $T = 1$ keV, the Maxwell-Boltzmann distribution predicts that $< 10^{-110}$ of electrons (rest mass $m_e =$

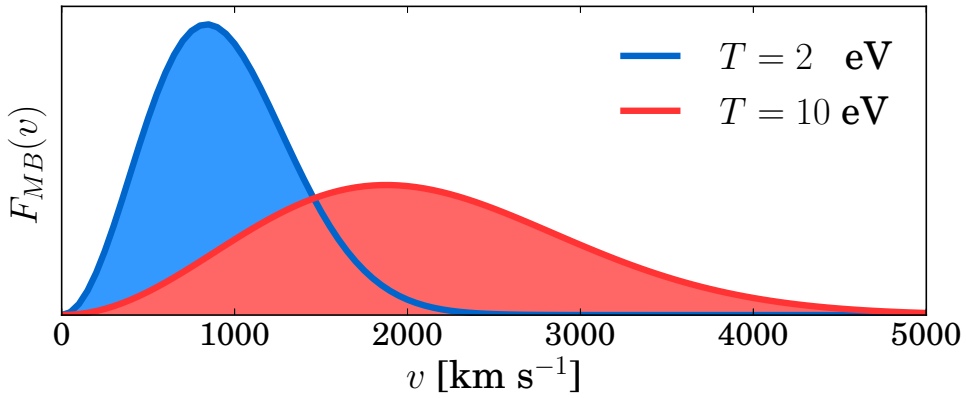

Figure 13: Maxwell-Boltzmann velocity distribution function $\mathbb{F}_{MB}(v)$ plotted for two temperatures as indicated.

511 keV/c^2) have speeds in excess of c; this fraction is proportionally even lower for the more massive ions. Therefore, particles are treated as non-relativistic throughout this text.

Particles require time to exchange energy in order to reach a steady state distribution. An approximate expression has been derived by Spitzer[19] for the time taken by particles in a plasma to reach a steady temperature. The expression due to Spitzer for the time taken by electrons to exchange energy is

$$\begin{aligned} t_{e-e} &= \left[\frac{3}{8ce^4}\sqrt{\frac{m_e c^2}{2\pi}}\right]\frac{T_e^{3/2}}{n_e \Xi} \\ &\simeq 3.3\times 10^5 \frac{T_e^{3/2}}{n_e \Xi}, \end{aligned} \tag{64}$$

and for electrons exchanging energy with ions the time is

$$t_{e-i} = \frac{1}{N_T Z^2}\frac{m_i}{m_e} t_{e-e}, \tag{65}$$

where Ξ is the Coulomb logarithm, a function of the plasma parameter from Equation (3). In standard units, we have $\Lambda = 3.48\times 10^8 T_e^{3/2} n_e^{-1/2}$. For relatively low energy density plasmas, the classical expression for the Coulomb logarithm is

$$\Xi = \ln(\Lambda). \tag{66}$$

However, if plasma conditions lead to $\Lambda < 1$, Equation (66) would lead to unphysically negative equilibration times. The Coulomb logarithm has been extrapolated in such a case to the expression[64]

$$\Xi = \exp\left(\frac{1}{\Lambda}\right)\mathbf{E}_1\left(\frac{1}{\Lambda}\right), \tag{67}$$

where $\mathbf{E}_1$ is the first exponential integral, as outlined in Appendix B.1.

3.1.2 Fermi-Dirac distribution

The Maxwell-Boltzmann distribution is derived assuming that the kinetic energy of a particle can take any arbitrary value and that any number of particles can have the same energy. These assumptions apply only approximately in the case of quantum mechanics: energies of particles are quantized, such as the familiar energy levels of electrons in atoms, and the class of particles called fermions (electrons, protons, ^{3}He atoms) may not occupy the same quantum state as each other. In practice, the densities of particles more massive than electrons are sufficiently low in laboratory plasmas for the Maxwell-Boltzmann distribution to be an accurate model for their motion, as discussed below, and so the discussion here is restricted to electrons.

The wavefunctions of electrons in free space (zero potential) are plane waves with quantized energies,

$$\Psi = \frac{1}{\sqrt{V}}\exp\left(i\vec{k}.\vec{x}\right), \vec{k} = \frac{2\pi}{V^{1/3}}\begin{pmatrix} p_x \\ p_y \\ p_z \end{pmatrix}, \epsilon = \frac{h^2k^2}{8\pi^2 m_e}, \tag{68}$$

where V is the volume in position occupied by the electrons, $\vec{k}$ is their momentum and $\vec{x}$ their position vector, and the symbols p are integers.

The probability of a given energy state being occupied is given by the Fermi distribution,[65]

$$\begin{aligned} F_{FD}(\epsilon, T_e) &= \frac{1}{\exp\left(\frac{\epsilon-\mu}{T_e}\right)+1} \\ &= \frac{1}{2}\left[1 - \tanh\left(\frac{\epsilon-\mu}{2T_e}\right)\right], \end{aligned} \tag{69}$$

where $\mu(T)$ is the chemical potential; we note that at $\epsilon = \mu$ the occupation probability is equal to $\frac{1}{2}$. The temperature dependence of the occupation probability is shown schematically in Figure 14a. To obtain the kinetic energy distribution function, Equation (69) must be multiplied by the density of states $g(\epsilon)d\epsilon$ - in effect, the number of possible states with a given energy. The density of states in k-space is $V|\vec{k}|^2 d|\vec{k}|/\pi^2$, corresponding in terms of ϵ to

$$g(\epsilon)d\epsilon = \frac{G}{n_e}\sqrt{\epsilon}, \tag{70}$$

where it is useful to define the quantity G as the degeneracy of a free electron,

$$G = 4\pi\left(\frac{2m_e c^2}{(hc)^2}\right)^{3/2}. \tag{71}$$

The Fermi-Dirac energy distribution for a gas of free electrons then becomes

$$f_{FD}(\epsilon, T_e) = \frac{G}{n_e}\sqrt{\epsilon}F_{FD}(\epsilon, T_e), \tag{72}$$

which is compared in Figure 14b to the corresponding Maxwell-Boltzmann distribution. We see that the two distributions agree well at high temperatures, but diverge at low temperatures. The Fermi-Dirac distribution has a larger width and peak energy there, as the Pauli exclusion principle prevents many electrons from occupying low-lying energy states.

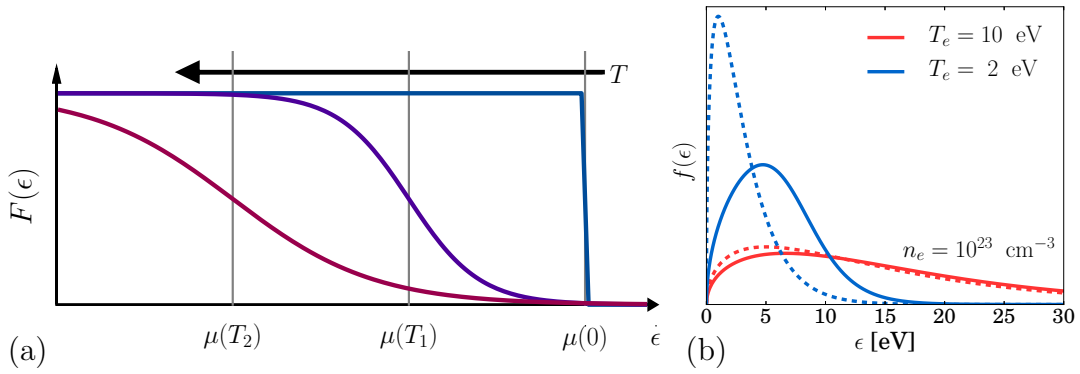

Figure 14: (a) Schematic diagram of the occupation probability $F(\epsilon)$ with increasing temperature ($T_2 > T_1 > 0$). The chemical potential, the point at which $F(\epsilon) = \frac{1}{2}$, is shown for the three temperatures. The occupation probability becomes a smoother function as temperature increases. (b) Comparison of the Fermi-Dirac energy distribution (solid) to the Maxwell-Boltzmann (dashed) at temperatures as indicated for an electron density $n_e = 10^{23}$ cm^{-3}.

The chemical potential is defined as a normalization factor, ensuring that the first moment is unity at each temperature. This leads to its definition through the transcendental equation

$$\langle 1 \rangle = \frac{G}{n_e}\int_0^\infty \frac{\sqrt{\epsilon}}{\exp\left(\frac{\epsilon-\mu}{T_e}\right)+1}d\epsilon = 1. \tag{73}$$

This integral can only be solved exactly in the special case of $T = 0$, when the Fermi distribution becomes a step function of energy, $F_{FD}(\epsilon, 0) = \Theta(\epsilon - \mu)$,

$$\int_0^\infty f_{FD}(\epsilon, 0)d\epsilon = \int_0^{\mu(0)} \frac{G}{n_e}\sqrt{\epsilon}d\epsilon. \tag{74}$$

Equations (73) and (74) define the chemical potential for a given electron density at zero temperature; it is usually termed the Fermi energy E_F,

$$\mu(0) \equiv E_F = \left(\frac{3}{2}\frac{n_e}{G}\right)^{2/3}. \tag{75}$$

At high temperatures, the Fermi-Dirac distribution must tend to the Maxwell-Boltzmann. We therefore require an expression for the chemical potential of a Maxwell-Boltzmann distribution, which we denote by $\bar{\mu}$. If we multiply the top and bottom of the fraction in Equation (69) by $\exp(\mu/T)$, the denominator becomes $\exp(\epsilon/T) + \exp(\mu/T) \approx \exp(\epsilon/T)$, when μ becomes large and negative at high temperatures. Equating this approximate form to the Maxwell-Boltzmann distribution from Equation (62), we have

$$\frac{2}{\sqrt{\pi}}\frac{\sqrt{\epsilon}}{T_e^{3/2}}\exp\left(-\frac{\epsilon}{T_e}\right) \approx \frac{G}{n_e}\sqrt{\epsilon}\exp\left(\frac{\mu-\epsilon}{T_e}\right). \tag{76}$$

This leads, after rearranging, to the Maxwell-Boltzmann chemical potential, with

$$\bar{\mu}(T_e) = T_e \ln\left[\frac{4}{3\sqrt{\pi}}\left(\frac{E_F}{T_e}\right)^{3/2}\right]. \tag{77}$$

For completeness, applying l'Hopital's rule to this function gives $\lim_{T_e\to 0}\bar{\mu}(T_e) = 0$.

Theorems presented in Appendix C show that the chemical potential is bracketed between E_F and $\bar{\mu}$, allowing it to be calculated using Brent's algorithm. However, it is more computationally efficient to approximate it using a series expansion. Fixing $\lim_{T_e\to\infty}\mu(T_e) = \bar{\mu}(T_e)$ and $\mu(0) = E_F$ has allowed the following Padé expansion of the chemical potential:[66]

$$\mu = T_e\frac{\frac{3}{2}\ln(u) + \sum_{i=0}^{7} a_i u^i + a_9 u^9 + a_{10}u^{2.5}}{1 + \sum_{j=1}^{4} b_j u^{2j}}, \tag{78}$$

where $u = (2/3)^{2/3}E_F/T_e$ and the expansion coefficients a and b are given in Table 3.

The heat capacity of a degenerate electron gas, from Equation (58), is given by the transcendental equation

$$C_V = \frac{G}{n_e}\int_0^\infty \frac{\epsilon^{3/2}}{1 + \exp(\frac{\epsilon-\mu}{T_e})}d\epsilon. \tag{79}$$

Coefficient	Value
a_0	$\ln(2/\sqrt{\pi})$
a_1	0.0233056178489510
a_2	1.0911595094936000
a_3	-0.2993063964300200
a_4	-0.0028618659615192
a_5	0.5051953653801600
a_6	0.0419579806591870
a_7	1.3695261714367000
a_9	0.2685157355131100
a_{10}	-1.2582793945794000
b_1	0.0813113962506270
b_2	1.1903358203098999
b_3	1.1445576113258000
b_4	$(2/3)^{2/3}a_9$

Table 3: Coefficients for the Padé expansion of the chemical potential for the Fermi-Dirac distribution given by Equation (78).

Intuitively, an electron gas contains energy even at $T = 0$ as the electrons then occupy energetic states up to the Fermi energy; we obtain $C_V(0) = \frac{3}{5}E_F$ by performing an integral similar to Equation (74). At non-vanishing temperatures, the heat capacity tends to $\frac{3}{2}T_e$ as energy distribution tends to the Maxwell-Boltzmann, as shown in Figure 15b. Likewise, the pressure tends to $\frac{2}{5}NE_F$, termed the degeneracy pressure.

We require Equation (79) to be inverted, to allow the temperature to be calculated as a function of energy density. The strategy for this is similar to the calculation of the chemical potential. It may be calculated by using Brent's method with the bounds $2C_V/3 > T_e \geq 0$. This method was used to calculate $C_V(u)$ at many values of $u = T_e/E_F$, allowing a Padé approximation to be obtained by curve fitting. The coefficients were chosen so that the two asymptotic values of C_V are recovered at $T_e = 0$ and as $T_e \to \infty$.

From the above expressions, the parameters defining a Fermi-Dirac distribution of electrons, including its departure from the Maxwell-Boltzmann, depend on the ratio $n_e/m_e^{3/2}$. Therefore, for more massive particles to achieve a similar level of degeneracy to electrons, their density must be proportionately higher. Electrons are degenerate at densities above one electron per atom at solid material density;

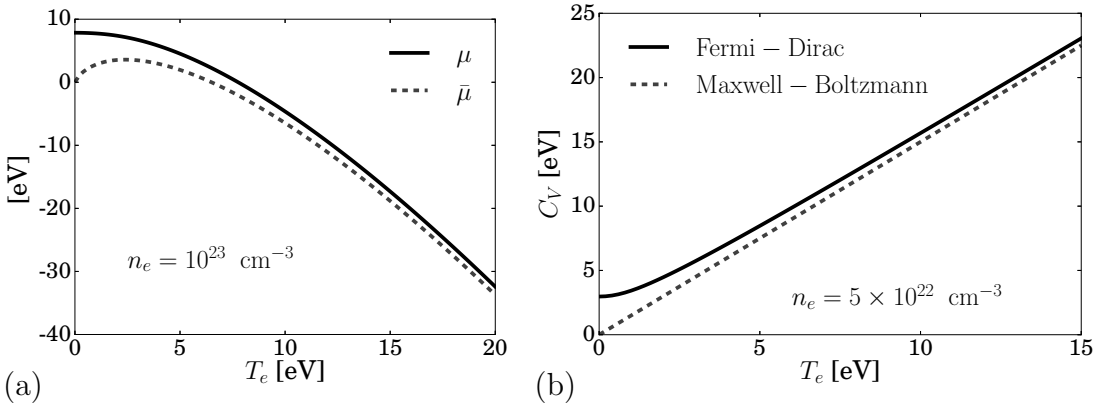

Figure 15: (a) The chemical potential for the Fermi-Dirac distribution $\mu(T_e)$ (solid) and its Maxwell-Boltzmann equivalent $\bar{\mu}(T_e)$ given by Equation (77) (dashed), for a fixed free electron density of 10^{23} cm^{-3}, corresponding approximately to the solid density of many elements. (b) The heat capacity of free electrons as a function of temperature for the distributions as labelled, for a fixed electron density of 5×10^{22} cm^{-3}.

correspondingly, densities of protons or more massive spin-$\frac{1}{2}$ nuclei which are orders of magnitude higher than solid are required before they must start to be modelled by the Fermi-Dirac distribution. Such high densities cannot be reached with current experimental techniques, but have been deduced to be gravitationally confined inside massive stellar objects, such as neutron stars.

3.1.3 Black-body radiation spectrum

Bosons are particles with integer spin; there is no limit to how many may occupy a given energy state. The occupation probability for bosons is given by the Bose-Einstein distribution[65]

$$F_{BE}(\epsilon, T) = \frac{1}{\exp\left(\frac{\epsilon-\mu}{T}\right) - 1}. \tag{80}$$

We are particularly interested in photons. The wavefunctions of free photons are similar to those of free electrons as given in Equation (68), but their energy differs as they are massless:

$$\Psi = \frac{1}{\sqrt{V}} \exp\left(i\vec{k}.\vec{x}\right), \vec{k} = \frac{2\pi}{V^{1/3}} \begin{pmatrix} p_x \\ p_y \\ p_z \end{pmatrix}, \epsilon = \frac{hc|\vec{k}|}{2\pi}. \tag{81}$$

The density of states for photons is identical to that for electrons in k-space, $V|\vec{k}|^2 d|\vec{k}|/\pi^2$, but in terms of ϵ it becomes

$$g(\epsilon)d\epsilon = \frac{8\pi\epsilon^2}{n_\gamma(hc)^3}d\epsilon, \tag{82}$$

with n_γ the density of photons. The energy distribution function is given as usual by $g(\epsilon)F_{BE}(\epsilon, T)$,

$$f_{BE}(\epsilon, T) = \frac{8\pi\epsilon^2}{n_\gamma(hc)^3}\frac{1}{\exp\left(\frac{\epsilon-\mu}{T}\right)-1}. \tag{83}$$

Hot matter in thermodynamic equilibrium radiates photons, usually termed black-body radiation, with the Bose-Einstein energy distribution; since the number of photons is not conserved in such a system, the chemical potential vanishes,[67] $\mu = 0$. The spectral intensity $I(\epsilon_\gamma)$ of black-body radiation is given by the product of the photon energy, density, speed (since we are interested in the power crossing a unit area as opposed to the spatial density) and the Bose-Einstein energy distribution at a particular radiation temperature T_r, so that

$$I_{BB}(\epsilon_\gamma) = \frac{8\pi\epsilon_\gamma^3}{h^3c^2}\frac{1}{\exp\left(\epsilon_\gamma/T_r\right)-1}, \tag{84}$$

where the flux is incident over 4π sr; this spectral intensity is plotted in Figure 16. As usual, an integral of the spectral intensity over the photon energy gives the total intensity of the black-body radiation; in this case $I = 2\pi^5 T_r^4/15h^3c^2$, referred to as the Stefan-Boltzmann law.

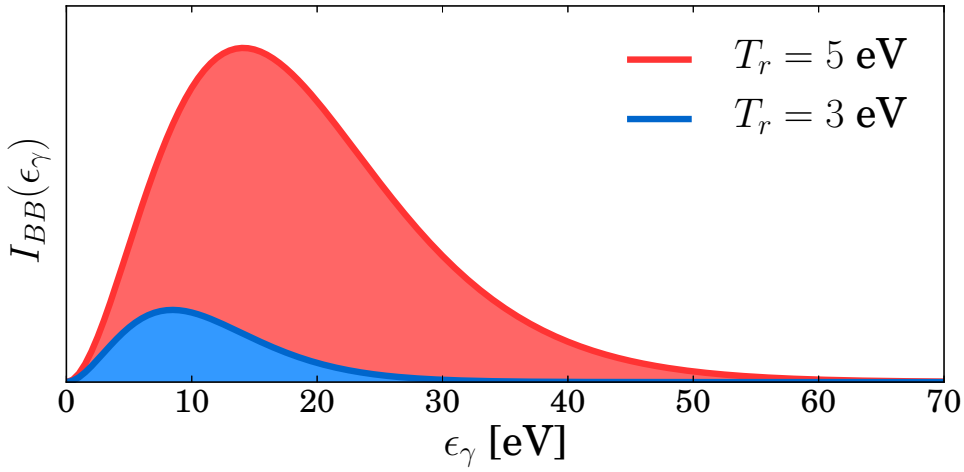

Figure 16: Spectral intensity of black-body radiation from matter with a temperature as indicated.

Unlike electrons, classically photons cannot interact with each other in the absence of any other particles. Therefore, the timescale for photons to equilibrate their energy and attain a black-body distribution is less precise - understandable,

perhaps, as photons do not "feel" time. As a consequence, it is common to encounter a non-equilibrium photon distribution, such as the narrow linewidth of a laser or line emission from a hot plasma.

3.2 Rate equation treatment

We have considered the distribution of kinetic energies of particles in a plasma, but will now consider the distribution of the types of ion present as a function of energy and particle density. The distribution of ions in plasmas are not, in general, in a steady state. Such a statistical distribution can be calculated in the general case by considering the atomic processes in a plasma. The approach followed here is to assemble the populations into a vector $\vec{N}$; its elements are always real and positive. We typically label each element $N_{i,j}$, where i numbers the ionization state and j the atomic level within it, as discussed in Appendix A.2.

Atomic processes are of the form $N_{i,j} \rightarrow N_{i',j'}$, with rates of transfer proportional to the population of origin - in this case, $N_{i,j}$. Therefore, the rate of change of an element of $\vec{N}$ is a linear combination of all elements of the vector; the rates of change of the entire vector can be written as[68]

$$\frac{d\vec{N}}{dt} = M(n_e, T_e)\vec{N}, \tag{85}$$

where $M(n_e, T_e)$ is termed the rate matrix. The nonlinearity of this equation is encapsulated by the fact that n_e and T_e are also typically a function of $\vec{N}$.

The diagonal elements of the rate matrix must be the negative sum of the corresponding column in order to conserve the total number of ions in the system, $M_{mm} = -\sum_{m \neq n} M_{nm}$, as an increase of one type of ion must be precisely balanced by the decrease of another. It is shown in Appendix B.2 that as a consequence of this fact, M is always singular.

Atomic processes involving free electrons have a corresponding transfer of energy to or from the gas of free electrons. The rate of energy transfer is given by the product of the atomic rate and the energy gap of the process. We therefore calculate the rate of kinetic energy change due to collisional processes using the matrix equation

$$\frac{d\varepsilon}{dt} = \sum \bar{M}\vec{N}, \tag{86}$$

where the auxiliary rate matrix $\bar{M}$ is constructed by multiplying each element M_{mn} by the energy difference $E_m - E_n$; the sign is negative if the process is endothermic

and the diagonals are zero. The temperature can then be calculated using the heat capacity

$$\varepsilon = C_V n_e. \tag{87}$$

For the Maxwell-Boltzmann distribution we therefore have $T_e = 2\varepsilon/3n_e$.

Although the negative and positive charges are mobile in a plasma, the bulk remains quasineutral; an external observer would detect no net charge. For each ion there is an appropriate number of electrons and therefore the electron and ion densities are related by

$$n_e = \sum_{i,j} iN_{i,j}. \tag{88}$$

3.3 Atomic processes in plasmas

We will now proceed with a description and discussion of the rates used to populate the matrices M and $\bar{M}$. The rate of an atomic process depends on the density of all reacting particles multiplied by a rate coefficient R, which is a measure of the probability of a reaction occuring. The total rate of a process is given by the product of the densities of

$$\mathcal{R} = R \prod_{j \text{ incoming}} N_j. \tag{89}$$

The rate coefficient of a generalized process with m incoming, l outgoing and n total particles is given by a series of integrals over all possible values of all the particle energies as follows:

$$R = \int_0^\infty d\epsilon_0 \cdots \int_0^\infty d\epsilon_n \delta(S) \mathbb{B} \prod_{j=0}^{m} v_j f(\epsilon_j, T_j) \prod_{k=0}^{l-1} \frac{d}{d\epsilon_k} \sigma(E_{threshold}, \epsilon_0 ... \epsilon_n), \tag{90}$$

where the particle velocities $v_j = \sqrt{2\epsilon_j/m}$, $\sigma(E_{threshold}, \epsilon_0 ... \epsilon_n)$ is the quantum mechanical cross section associated with the process, f is the kinetic energy distribution of the particle and the argument of the delta function acts to impose energy conservation,

$$S = \sum_{j=0}^{m} \epsilon_j - E_{threshold} - \sum_{k=0}^{l} \epsilon_k. \tag{91}$$

The cross section is differentiated $l-1$ times over each outgoing particle; the differential cross section effectively specifies the energy distributions of outgoing particles.

If the interacting particles are fermions, we must ensure that there are sufficient empty energy states for the particle to occupy after the collision. We therefore introduce a so-called Pauli blocking factor

$$\tilde{F}(\epsilon) = 1 - F_{FD}(\epsilon) \tag{92}$$

$$= \exp\left(\frac{\epsilon - \mu}{T}\right) F_{FD}(\epsilon). \tag{93}$$

We introduce one blocking factor for each outgoing electron in Equation (90). They are only necessary if the temperature is low, as the blocking factor tends to unity at high temperatures (when the energy distribution tends to the Maxwell-Boltzmann distribution) where the energy states are only sparsely populated and no blocking occurs. The symbol $\mathbb{B}$ in Equation (90) is used to take these blocking factors into account and has two regimes,

$$\mathbb{B}_{FD} = \prod_{k=0}^{l} \tilde{F}(\epsilon_k),$$

$$\mathbb{B}_{MB} = 1.$$

In this work, we consider the interaction of light and electrons with, or in the presence of, ions. However, due to the significantly lower mass and consequently higher speeds of the electron compared to even the lightest ion, we consider ion to be fixed when calculating rate coefficients and therefore drop integrals containing their energies from Equation (90).

3.3.1 Principle of detailed balance

Atomic processes are reversible on the micro-scale, albeit with differing cross sections. If the cross section of a process is known, the cross section of the inverse rate may be deduced from thermodynamics. By comparing populations in thermodynamic equilibrium, which are in well-defined ratios, relations for cross sections and their inverse can be derived. Once such relations are derived in equilibrium, they apply equally for arbitrary rates, as the quantum mechanics of the interaction do not depend on the populations.

Consider two mutually inverse processes α and β. The rates in equilibrium are, by definition, equal, so that $\prod_j N_j R_\alpha = \prod_k N_k R_\beta$, where the indices j and k run

over the incoming particles of process α and β respectively. The two processes must have an identical number of interacting particles and therefore the variables of integration in Equation (90) are identical, as are the arguments of the delta function. We can therefore equate the integrands in both cases:

$$\mathbb{B}_\alpha \prod_j N_j \prod_{j=0}^{m} v_j f(\epsilon_j, T_j) \prod_{k=0}^{l-1} \frac{d}{d\epsilon_k} \sigma_\alpha = \mathbb{B}_\beta \prod_k N_k \prod_{k=0}^{l} v_k f(\epsilon_k, T_k) \prod_{j=0}^{m-1} \frac{d}{d\epsilon_j} \sigma_\beta. \tag{94}$$

This equality must hold in a hot, non-degenerate plasma. In this case, the blocking factors tend to unity and the energy distribution function takes the form of the Maxwell-Bolzmann distribution for electrons and the black-body distribution for photons. The temperatures are also in equilibrium, $T_e = T_\gamma = T$. We therefore have

$$\begin{aligned} v f_{MB}(\epsilon, T) &= \frac{2}{T^{3/2}} \sqrt{\frac{2}{m\pi}} \exp\left(-\frac{\epsilon}{T}\right) \quad \text{(electrons)}, \\ v f_{BB}(\epsilon, T) &= \frac{2c\epsilon_\gamma^3}{(hc)^2} \frac{1}{\exp(\epsilon_\gamma/T) - 1} \qquad \text{(photons)}. \end{aligned}$$

Finally, we can use thermodynamic equations to relate the different population densities. For instance, the populations of two levels of a given ionization stage are related using Boltzmann statistics: $N_{i,j}/N_{i,j'} = g_{j'}/g_j \exp([E_{j'} - E_j]/T)$, where the g factors correspond to the levels' degeneracies.

This analysis, referred to as detailed balance, provides a recipe for calculating inverse cross sections. Once a process and its (differential) cross section are identified, we are able to use the equilibrium energy distributions, known degeneracy factors and appropriate thermodynamic equilibria to identify the inverse. In the following sections, we will not derive the relations explicitly, but quote them together with their historical names.

3.3.2 Collisional excitation and de-excitation

The high energy and free electron densities typical of a plasma are so large that a significant number of atoms may be excited to very energetic quantum states not typically seen in condensed matter. Bound electrons can be excited or de-excited by the impact of free electrons, symbolically denoted for an atom X by

$$X_{i,j} + e^- \rightleftharpoons X_{i,j'} + e^-.$$

We reserve the term "excitation" exclusively for endothermic transitions, where the level j has lower potential energy than j' and "de-excitation" for the inverse process.

The total rate of collisional excitation is given by

$$\mathcal{R}_{\text{collisional excitation}} = \left[n_e J^{\uparrow}\right] N_{i,j}, \tag{95}$$

where we have used the symbol J for the rate coefficient of this type of process in which $\uparrow$ and $\downarrow$ denote excitation and de-excitation respectively. The rate is proportional to the ion density of origin $N_{i,j}$, as noted in §3.3, with the quantity in brackets appearing in the rate matrix M.

Functional forms for the cross section are typically obtained by fitting known functions to experimental data. Experimentally, the cross section for this process does not depend on the outgoing electron energy. It is useful to write the cross section in terms of a collision strength Ω,

$$\sigma^{\uparrow}(\epsilon_0) = \frac{\Omega(\epsilon_0)}{g_j \epsilon_0}, \tag{96}$$

where g_j is the degeneracy of the original state and ϵ_0 the incoming electron energy.

Typical forms for the collisional cross section, in this case for carbon,[69] have for optically allowed transitions

$$\Omega_a\left(\frac{\epsilon_0}{E_j}\right) = B_0 \ln\left(\frac{\epsilon_0}{E_j}\right) + \sum_{k=1}^{3} B_k \left(\frac{\epsilon_0}{E_j}\right)^{-(k-1)}, \tag{97}$$

and two types of cross section for optically forbidden transitions

$$\Omega_{f1}\left(\frac{\epsilon_0}{E_j}\right) = \sum_{k=1}^{4} B_k \left(\frac{\epsilon_0}{E_j}\right)^{-(k-1)}, \tag{98}$$

$$\Omega_{f2}\left(\frac{\epsilon_0}{E_j}\right) = \sum_{k=1}^{4} B_k \exp\left(-k B_0 \frac{\epsilon_0}{E_j}\right) + B_5 \left(\frac{\epsilon_0}{E_j}\right)^{-2}. \tag{99}$$

To proceed, the associated collisional excitation rate coefficient may be calculated through Equation (90). There is now only a single incoming and outgoing electron, so all the energies in the system are well defined. For the Maxwell-Boltzmann distribution, the integrals of Equation (90) reduce to

$$\begin{aligned} J^{\uparrow} &= \sqrt{\frac{2}{m_e}} \int_0^{\infty} \int_0^{\infty} \sigma(\epsilon_0)\delta(\epsilon_0 - \epsilon_1 - E_j)\sqrt{\epsilon_0} f_{MB}(\epsilon_0, T_e) \mathbb{B}_{MB} d\epsilon_0 d\epsilon_1 \\ &= \frac{2}{g_j T_e^{3/2}} \sqrt{\frac{2}{\pi m_e}} \int_{E_j}^{\infty} \Omega\left(\frac{\epsilon_0}{E_j}\right) \exp\left(-\frac{\epsilon_0}{T_e}\right) d\epsilon_0. \end{aligned} \tag{100}$$

We have carried out the integral over the outgoing electron energy ϵ_1 to obtain the Heaviside step function $\Theta(\epsilon_0 - E_j)$, which has modified the limits. We integrate the logarithmic component by the treatment in Equation (191). We also make use of the integral $\int_{E_j}^{\infty} \exp(-\epsilon_0/T_e) d\epsilon_0 = T_e \exp(-E_j/T_e)$. The other polynomials are integrated by parts, and the exponentials in Ω_{f2} may be combined with the Maxwell-Boltzmann factor and integrated in a similar fashion:

$$J_a^{\uparrow} = \frac{E_j}{g_j}\sqrt{\frac{8}{\pi m_e T_e^3}}\left[\exp\left(-\frac{E_j}{T_e}\right)\left(\frac{B_1 T_e}{E_j} + B_3\right) + \mathbf{E}_1\left(\frac{E_j}{T_e}\right)\left(\frac{B_0 T_e}{E_j} + B_2 - \frac{B_3 E_j}{T_e}\right)\right] \tag{101}$$

$$J_{f1}^{\uparrow} = \frac{E_j}{g_j}\sqrt{\frac{8}{\pi m_e T_e^3}}\left[\exp\left(-\frac{E_j}{T_e}\right)\left(\frac{B_1 T_e}{E_j} + B_3 + \frac{B_4}{2}\frac{T_e - E_j}{T_e}\right) + \mathbf{E}_1\left(\frac{E_j}{T_e}\right)\left(B_2 - B_3\frac{E_j}{T_e} + \frac{B_4 E_j^2}{2T_e^2}\right)\right] \tag{102}$$

$$J_{f2}^{\uparrow} = \frac{E_j}{g_j}\sqrt{\frac{8}{\pi m_e T_e^3}}\left[\sum_{k=1}^{4}\frac{B_k \exp(-kB_0 - E_j/T_e)}{kB_0 + E_j/T_e} + B_5 \exp\left(-\frac{E_j}{T_e}\right) - \frac{B_5 E_j}{T_e}\mathbf{E}_1\left(\frac{E_j}{T_e}\right)\right]. \tag{103}$$

A very general form for optically allowed transitions has been historically suggested by Van Regemorter:[70]

$$J_{VR}^{\uparrow} = \frac{8\pi^{3/2}}{\sqrt{3}} a_0^2 \mathrm{Ry}^2 \frac{f_j}{E_j T_e^{1/2}} \mathbf{G}(E_j/T_e), \tag{104}$$

where f_j is the oscillator strength of the transition, a_0 the Bohr radius and Ry the Rydberg constant. The oscillator strength may be calculated from the overlap integral of the wavefunctions of the higher and lower quantum state, or more commonly, determined by experiment.[71] $\mathbf{G}(E_j/T_e)$ is the so-called Gaunt factor, which is a simplification of the overlap integral. Its functional form is given for differing ranges of its arguments, in this case

$$\begin{aligned} \mathbf{G}(E_j/T_e) &= \frac{\sqrt{3}}{2\pi}\mathbf{E}_1(E_j/T_e); \quad E_j/T_e \to 0, \\ \mathbf{G}(E_j/T_e) &= \frac{1}{5}\exp(-E_j/T_e); \quad E_j/T_e > 1. \end{aligned} \tag{105}$$

The Van Regemorter rate is historically significant and continues to be a good estimate for the collisional excitation rate against which more advanced calculations may be benchmarked. It is useful because it applies to all elements and requires

knowledge of only the oscillator strength. The oscillator strength is easier to determine through theory or experiment than a full cross section.

To compute the rates for degenerate plasmas, we use the Fermi-Dirac distribution and insert a Pauli blocking factor for the outgoing electron into Equation (90). Following the same treatment as above, we are left with the integral

$$J^{\uparrow}_{FD} = \frac{G}{n_e g_j}\sqrt{\frac{2}{m_e}}\int_{E_j}^{\infty}\Omega\left(\frac{\epsilon_0}{E_j}\right)F_{FD}(\epsilon_0, T_e)\tilde{F}(\epsilon_0 - E_j, T_e)d\epsilon_0. \tag{106}$$

There is no further analytic simplification to this integral, and it must be calculated using numerical methods, as detailed in Appendix B.6.

To obtain the cross section of the inverse process, we use micro-reversibility relations;[72] these are derived through the principle of detailed balance. For collisional excitation, this relation is given by

$$g_{j'}\epsilon_0\sigma^{\downarrow}(E_j, \epsilon_0) = g_j(\epsilon_0 + E_j)\sigma^{\uparrow}(E_j, \epsilon_0 + E_j). \tag{107}$$

Substituting this into the integral for the rate coefficient, we can preserve the limits and cross section in the excitation integral by shifting the argument of the energy distribution function through the substitution $\bar{\epsilon_0} = \epsilon_0 - E_j$. For the Maxwell-Boltzmann distribution, $\exp(-\bar{\epsilon_0}/T_e) = \exp(E_j/T_e)\exp(-\epsilon_0/T_e)$, and so we have

$$J^{\downarrow} = \frac{g_j}{g_{j'}}\exp(E_j/T_e)J^{\uparrow}. \tag{108}$$

For degenerate plasmas, the de-excitation coefficient is given by

$$J^{\downarrow}_{FD} = \frac{G}{n_e g_j}\sqrt{\frac{2}{m_e}}\int_{E_j}^{\infty}\Omega\left(\frac{\epsilon_0}{E_j}\right)F_{FD}(\epsilon_0 - E_j, T_e)\tilde{F}(\epsilon_0, T_e)d\epsilon_0. \tag{109}$$

Writing the blocking factors explicitly using the form in Equation (93), we have for the excitation and de-excitation coefficients respectively

$$J^{\uparrow}_{FD} = \frac{G}{n_e g_j}\sqrt{\frac{2}{m_e}}\int_{E_j}^{\infty}\Omega\left(\frac{\epsilon_0}{E_j}\right)\exp\left(\frac{\epsilon_0 - E_j - \mu}{T_e}\right)F_{FD}(\epsilon_0 - E_j, T_e)F_{FD}(\epsilon_0, T_e)d\epsilon_0, \tag{110}$$

$$J^{\downarrow}_{FD} = \frac{G}{n_e g_{j'}}\sqrt{\frac{2}{m_e}}\int_{E_j}^{\infty}\Omega\left(\frac{\epsilon_0}{E_j}\right)\exp\left(\frac{\epsilon_0 - \mu}{T_e}\right)F_{FD}(\epsilon_0 - E_j, T_e)F_{FD}(\epsilon_0, T_e)d\epsilon_0. \tag{111}$$

The factor $\exp(-E_j/T_e)$ may be taken outside the integral for collisional excitation, and hence we see that Equation (108) also holds for degenerate plasmas.

Collisional processes can force each level to transition to any other level in a given ionization stage. Combinatorially, this is akin to the "Handshake Problem"[73] ; this implies that the maximum number of possible transitions for a given ionization stage with n atomic levels is given by $n(n-1)/2$. The practical number of transitions may be significantly lower, as some transitions have vanishing rate coefficients; optically forbidden transitions often have $B_k \to 0$ and oscillator strengths $f_j \simeq 0$.

3.3.3 Spontaneous and stimulated emission

Atoms in excited states decay over time to lower energy states by the process of spontaneous emission of a photon of energy $\hbar\omega = E_j$,

$$X_{i,j} \to X_{i,j'} + \gamma,$$

with a rate given by

$$\mathcal{R}_{\text{sponataneous emission}} = AN_{i,j}.$$

The associated rate coefficient, sometimes referred to as the Einstein A-coefficient, is independent of the surrounding radiation field. It is related to the corresponding oscillator strength f_j by

$$A_j = \frac{2\pi ce^2}{(hc)^2 m_e c^2 \varepsilon_0} E_j^2 f_j. \tag{112}$$

Photons resonant with this radiative transition can be absorbed, or stimulate the emission of an identical (and in quantum terms entangled) photon, which is of course central to the operation of lasers. The total rate of this process is given by

$$\mathcal{R}_{\text{stimulated emission}} = BIN_{i,j},$$

where we denote the Einstein B-coefficient with the symbols $\uparrow$ and $\downarrow$ for absorption and stimulated emission respectively.

Derivation of the relationships between the Einstein coefficients is historically perhaps the earliest use of the detailed balance principle. These relations are given as follows:

$$\frac{A}{B^{\downarrow}} = \frac{2\epsilon_\gamma^3}{(hc)^2}, \tag{113}$$

$$\frac{B^{\downarrow}}{B^{\uparrow}} = \frac{g_j}{g_{j'}}. \tag{114}$$

3.3.4 Collisional ionization and three body recombination

Free electrons of sufficient energy may collisionally excite bound electrons to the energy level of the continuum, thereby ionizing them and releasing an additional electron. Inversely, a free electron may recombine with and ion and in the process "donate" its kinetic energy and liberated potential energy to another free electron in a process called three body recombination. For an ion X, these processes are schematically described as

$$X_{i,j} + e^- \rightleftharpoons X_{i+1,j'} + e^- + e^-.$$

We assume that generally only the outermost electron is ejected by an ionizing collision and all others are unaffected. The excitation state of the inner electrons is therefore preserved. By symmetry, electrons may recombine into any excitation state, but leave the others unaffected.

The rate of collisional ionization is given by

$$\mathcal{R}_{\text{collisional ionization}} = \left[n_e K^{\uparrow}\right] N_i, \tag{115}$$

where $K^{\uparrow}$ is the rate coefficient. This rate coefficient is calculated as usual from Equation (90). For an incoming electron with energy ϵ_0 and two outgoing electrons ϵ_1 and ϵ_2, we have

$$K^{\uparrow} = \sqrt{\frac{2}{m_e}} \int_0^{\infty} \int_0^{\infty} \int_0^{\infty} \sqrt{\epsilon_0} \frac{d\sigma^{\uparrow}}{d\epsilon_1} f\left(\epsilon_0\right) \delta(\epsilon_0 - E_i - \epsilon_1 - \epsilon_2) \mathbb{B} d\epsilon_0 d\epsilon_1 d\epsilon_2. \tag{116}$$

Once again, we integrate over one of the outgoing electron energies ϵ_2, yielding a step function and shifting the limits. Thus, for the Maxwell-Boltzmann distribution function the integral simplifies to

$$K^{\uparrow} = \sqrt{\frac{2}{m_e}} \int_{E_i}^{\infty} \int_0^{\epsilon_0 - E_i} \sqrt{\epsilon_0} \frac{d\sigma^{\uparrow}}{d\epsilon_1} f_{MB}\left(\epsilon_0\right) d\epsilon_0 d\epsilon_1. \tag{117}$$

The differential cross section by its definition must satisfy

$$\int_0^{\epsilon_0 - E_i} \frac{d\sigma^{\uparrow}(\epsilon_0, \epsilon_1)}{d\epsilon_1} d\epsilon_1 = \sigma^{\uparrow}(\epsilon_0), \tag{118}$$

so that Equation (117) reduces to

$$K^{\uparrow} = \sqrt{\frac{2}{m_e}} \int_{E_i}^{\infty} \sqrt{\epsilon_0} \sigma^{\uparrow}\left(\epsilon_0\right) f_{MB}\left(\epsilon_0\right) d\epsilon_0. \tag{119}$$

We discuss two of the most successful functional fits to the collisional ionization cross section. The so-called BELI cross section is given by[74]

$$\sigma^{\uparrow}(\epsilon_0) = \frac{1}{E_i \epsilon_0}\left[C_0 \ln\left(\frac{\epsilon_0}{E_i}\right) + \sum_{k=1} C_k \left(\frac{\epsilon_0 - E_i}{\epsilon_0}\right)^k\right], \tag{120}$$

where E_i is the ionization potential. This functional form requires precise curve fitting to accurate atomic data for every individual ionization stage.

A very comprehensive study of $\sigma^{\uparrow}$ for many elements was undertaken by Lotz,[75] which suggests for the functional form of the cross section

$$\sigma_L^{\uparrow}(\epsilon_0) = \frac{\ln(\epsilon_0/E_i)}{\epsilon_0 E_i}\left[C_0 + C_1 \exp\left(-C_2 \frac{\epsilon - E_i}{E_i}\right)\right]. \tag{121}$$

The constants C_1 and C_2 are typically small and may be ignored, while remarkably C_0 is the product of ξ, the number of outer-shell electrons of the ion, and a numerical constant which is universal to all elements and ionization stages. This cross section is plotted in Figure 17a. In standard units, the rate coefficient becomes

$$K_L^{\uparrow} = 2.97 \times 10^{-6} \frac{\xi}{T_e^{1/2}} \frac{\mathbf{E}_1(E_i/T_e)}{E_i}. \tag{122}$$

When electrons are ionised from a quantised energy level orbital by monoenergetic radiation, such as an incident laser, their kinetic energy is fixed at $\epsilon_0 = \epsilon_\gamma - E_i$. This sharp distribution can be modelled by a δ-function:

$$f_\delta(\epsilon_0) = \delta(\epsilon_0 - [\epsilon_\gamma - E_i]). \tag{123}$$

The usual approach, applied to the δ-function distribution, leads to the following expression for the rate coefficient:

$$K_\delta^{\uparrow} = C_0 \sqrt{\frac{2}{m_e}} \int_0^\infty \frac{\ln(\epsilon_0/E_i)}{\sqrt{\epsilon_0} E_i} \delta(\epsilon_0 - \epsilon_{electron})\, d\epsilon_0. \tag{124}$$

Here, $\epsilon_{electron}$ corresponds to $E_\gamma - E_i$ in Equation (123). In this case, the photoionized electron has sufficient energy to collisionally ionize, corresponding to $\epsilon_\gamma > 2E_i$. This condition can likewise be enforced by introducing a Heaviside function. The rate coefficient then becomes

$$K_\delta^{\uparrow} = 2.63 \times 10^{-6} \frac{\xi}{\sqrt{\epsilon_{electron}}} \frac{\ln(\epsilon_{electron}/E_i)}{E_i}. \tag{125}$$

As a means of comparing the two rate coefficients, equivalent energy per electron can be taken to be $\epsilon_{electron} = \frac{3}{2} T_e$. A plot comparing Maxwell-Boltzmann

distribuion to the δ-function distribution with this assumption (Equations (122) and (125) respectively) is shown in Figure 17b. The two functions are remarkably similar for low temperatures ($T_e < 2E_i$). However, as the temperature increases, the former overlaps better with the peak of the Lotz cross section. Furthermore, it may be assumed that more energetic electrons tend to equilibrate faster, and so the Maxwell-Boltzmann distribution may be used to good accuracy.

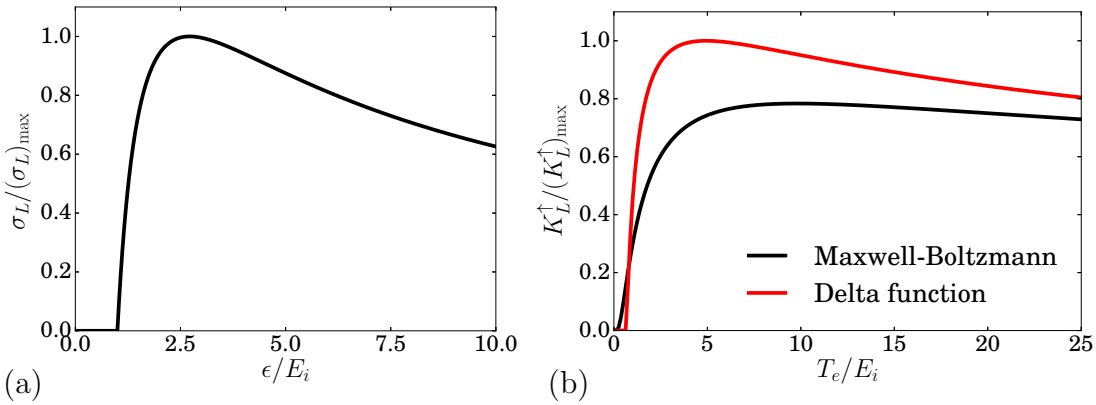

Figure 17: (a) Lotz's[75] collisional ionization cross section, plotted in reduced units as indicated. (b) Comparison of the collisional ionization rate due to the Lotz cross section for the Maxwell-Boltzmann and $\delta(\epsilon_0 - \epsilon_{electron})$ energy distributions, with $\epsilon_{electron} = \frac{3}{2}T_e$, as indicated.

The calculation of the collisional ionization coefficient for a degenerate plasma now requires two blocking factors for outgoing electrons. As a consequence, Equation (118) cannot be used to integrate the differential cross section and therefore we cannot use a formula such as that of Lotz for the total cross section. We therefore have for the collisional ionization coefficient

$$K_{FD}^{\uparrow} = \sqrt{\frac{2}{m_e}} \int_{E_i}^{\infty} \int_{0}^{\epsilon_0 - E_i} \sqrt{\epsilon_0} \frac{d\sigma^{\uparrow}}{d\epsilon_1} f_{FD}\left(\epsilon_0\right) \tilde{F}(\epsilon_1, T) \tilde{F}(\epsilon_0 - \epsilon_1 - E_i, T) d\epsilon_0 d\epsilon_1. \quad (126)$$

This rate coefficient is problematic to compute, as the blocking factors preclude an analytic solution. More importantly, additonal information about the process must be known, in the form of the differential cross section. In effect, the total cross section does not provide enough information about the distribution of energies of the outgoing electrons, which is necessary to fully take account of blocking factors.

One suggested formula for the differential cross section is due to Mott, with reasonable agreement to experimental results:[76,77]

$$\left(\frac{d\sigma^{\uparrow}}{d\epsilon_1}\right)_{Mott} = \frac{4\pi a_0^2 \mathrm{Ry}^2}{\epsilon_0}\left[\frac{1}{(\epsilon_1+E_i)^2}+\frac{1}{(\epsilon_1-\epsilon_0)^2}-\frac{1}{(\epsilon_1+E_i)(\epsilon_1-\epsilon_0)}\right], \tag{127}$$

where a_0 is the Bohr radius and Ry the Rydberg constant. The Mott cross section is nonzero for ϵ_1 on the interval $\{0, \epsilon_0 - E_i\}$. It is symmetric about the middle of this interval, as the two emergent electrons are indistinguishable particles. The Mott cross section peaks at the two ends of its domain, which means that electrons are most likely to emerge from collisional ionization in pairs: one fast and one slow.

When integrated as in Equation (118), the Mott cross section is not consistent with experimentally derived cross sections or even the broadly applicable Lotz formula: its integral does not produce a logarithmic dependence. However, it is possible to use the functional form and properties of the Mott cross section to deduce one which is compatible with experiments. Consider the indefinite integral

$$\int \frac{1}{(x+a)(x+b)}dx = \frac{\ln\left(\frac{x+a}{x+b}\right)}{(b-a)}. \tag{128}$$

After applying the limits in Equation (118) and comparing to the first term in Equation (120), we have

$$\int_0^{\epsilon_0-E_i} \frac{1}{(\epsilon_1+a)(\epsilon_1+b)}d\epsilon_1 \equiv \frac{\ln\left(\frac{\epsilon_0-E_i+a}{\epsilon_0-E_i+b}\frac{b}{a}\right)}{(b-a)} = \frac{\ln\left(\frac{\epsilon_0}{E_i}\right)}{E_i},$$

which allows the constants a and b to be solved for. The polynomial depnedence in Equation (120) can be achieved by considering the integral

$$\int_0^{\epsilon_0-E_i} \epsilon_1^{k-1}d\epsilon_1 = \frac{1}{k}(\epsilon_0-E_i)^k. \tag{129}$$

Finally, the expression must be "mirrored" to be symmetric about the centre of its domain just as the Mott cross section.

Lemma. *A function $f(x)$ defined on the interval $0 \leq x \leq L$ may be made symmetric about $L/2$, while preserving its definite integral over the interval.*

Let $\bar{f}(x) = \frac{1}{2}[f(x)+f(L-x)]$. To be symmetric about $L/2$, the value of a function at a point must equal the value at a point equidistant from $L/2$; for a point x_1, such an equidistant point must satisfy $L/2 - x_1 = L/2 + x_1$. Therefore, since $\bar{f}(x) = \bar{f}(L-x)$ by construction, this condition is satisfied. Finally, $\int_0^L f(L-x_1)dx_1$ may be simplified by the substitution $x_2 = L - x_1$, giving $-\int_L^0 f(x_2)dx_2 = \int_0^L f(x_2)dx_2$. Therefore, the definite integral is preserved by $\bar{f}(x)$.

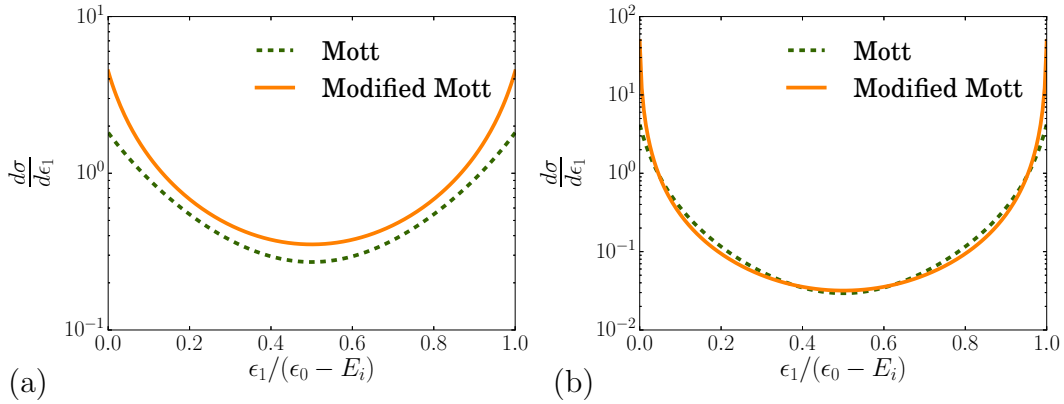

Figure 18: Comparison of the cross sections as indicated, given by Equation (127) and (130), for $E_i = 24.6$ eV, (a) $E_0 = 100$ eV and (b) $E_0 = 500$ eV, without the normalization constant.

As part of this work, we have produced the following expression for the collisional ionization differential cross section:

$$\frac{d\sigma^{\uparrow}}{d\epsilon_1} = \frac{1}{2E_i\epsilon_0}\left[\frac{C_0E_i}{(\epsilon_1+a)(\epsilon_1+b)} + \frac{C_0E_i}{(\epsilon_0-\epsilon_1-E_i+a)(\epsilon_0-\epsilon_1-E_i+b)} + \sum_{k=1} kC_k\frac{\epsilon_1^{k-1}+(\epsilon_0-\epsilon_1-E_i)^{k-1}}{\epsilon_0^k}\right], \tag{130}$$

with the quantities

$$a = \frac{1}{2}\left(\sqrt{\epsilon_0^2+4E_i^2}-\epsilon_0\right),$$
$$b = a + E_i.$$

This expression is compared to the Mott cross section for two values of ϵ_0 in Figure 18. We observe a reasonable similarity between the two functions. The equivalent differential cross section for the Lotz formula is given by

$$\frac{d\sigma_L^{\uparrow}}{d\epsilon_1} = \frac{1.32\times10^{-6}\xi}{\epsilon_0}\sqrt{\frac{m_e}{2}}\left[\frac{1}{(\epsilon_1+a)(\epsilon_1+b)} + \frac{1}{(\epsilon_0-\epsilon_1-E_i+a)(\epsilon_0-\epsilon_1-E_i+b)}\right]. \tag{131}$$

The Fermi-Dirac collisional ionization rate coefficient can then be calculated through the formula

$$K_{FD}^{\uparrow} = \sqrt{\frac{2}{m_e}}\frac{G}{n_e}\int_{E_i}^{\infty}\int_0^{\epsilon_0-E_i}\epsilon_0\frac{d\sigma^{\uparrow}}{d\epsilon_1}F_{FD}\left(\epsilon_0,T_e\right)\tilde{F}(\epsilon_1,T_e)\tilde{F}(\epsilon_0-\epsilon_1-E_i,T_e)d\epsilon_0 d\epsilon_1. \tag{132}$$

Again, there is no analytical form for this integral, requiring solution by numerical methods as detailed in Appendix B.6.

The rate of three body recombination process requires two incoming electrons and therefore has a quadratic dependence on electron density,

$$\mathcal{R}_{\text{three body recombination}} = \left[n_e^2 K^{\downarrow}\right] N_i. \tag{133}$$

To calculate the rate coefficient $K^{\downarrow}$, we reuse the collisional ionization cross section via the micro-reversibility relations.[72] For three body recombination, this gives

$$\sqrt{\frac{2}{m_e}} G g_{i+1} \epsilon_1 \epsilon_2 \sigma^{\downarrow}(E_i, \epsilon_1, \epsilon_2) = g_i \epsilon_0 \frac{d\sigma^{\uparrow}}{d\epsilon_1}, \tag{134}$$

where g corresponds to the degeneracy factor of the appropriate atomic level. Applying the general rate coefficient formula in Equation (90) and micro-reversibility from Equation (134) to three body recombination, we have for the rate coefficient

$$K^{\downarrow} = \frac{g_i}{g_{i+1}} \frac{1}{G} \sqrt{\frac{2}{m_e}} \int_{E_i}^{\infty} \int_0^{\epsilon_0 - E_i} \epsilon_0 \frac{d\sigma^{\uparrow}}{d\epsilon_1} \frac{f(\epsilon_1)}{\sqrt{\epsilon_1}} \frac{f(\epsilon_0 - \epsilon_1 - E_i)}{\sqrt{\epsilon_0 - \epsilon_1 - E_i}} \mathbb{B} \, d\epsilon_0 d\epsilon_1. \tag{135}$$

When evaluating this rate coefficient for the Maxwell-Boltzmann distribution this equation simplifies greatly. The square roots in the denominators cancel the same factor in Equation (62), while a product of the exponential factors allows their arguments to add linearly: $\exp(-\epsilon_1/T_e)\exp(-[\epsilon_0 - \epsilon_1 - E_i]/T_e) = \exp(E_i/T_e)\exp(-\epsilon_0)$. As the dependence on ϵ_1 has cancelled out, we are able to use Equation (118) to integrate the differential cross section. The resulting integral is directly comparable to that for collisional ionization and so we have a relation between the two inverse-rate coefficients:

$$K^{\downarrow} = \frac{2}{\sqrt{\pi} T_e^{3/2}} \frac{1}{G} \frac{g_i}{g_{i+1}} \exp\left(\frac{E_i}{T_e}\right) K^{\uparrow}. \tag{136}$$

The micro-reversibility relations may also be applied to the calculation of the degenerate rate coefficient. Inserting the Fermi-Dirac energy distribution and appropriate blocking factor, we have for the three body recombination rate

$$K^{\downarrow} = \frac{g_i}{g_{i+1}} \frac{G}{n_e^2} \sqrt{\frac{2}{m_e}} \int_{E_i}^{\infty} \int_0^{\epsilon_0 - E_i} \epsilon_0 \frac{d\sigma^{\uparrow}}{d\epsilon_1} F_{FD}(\epsilon_1, T_e) F_{FD}(\epsilon_0 - \epsilon_1 - E_i, T_e) \tilde{F}(\epsilon_0, T_e) d\epsilon_0 d\epsilon_1. \tag{137}$$

This may be related to the degenerate collisional ionization coefficient by explicitly using the blocking factor of Equation (93). Consider the product of occupation probabilities and blocking factors in Equation (132),

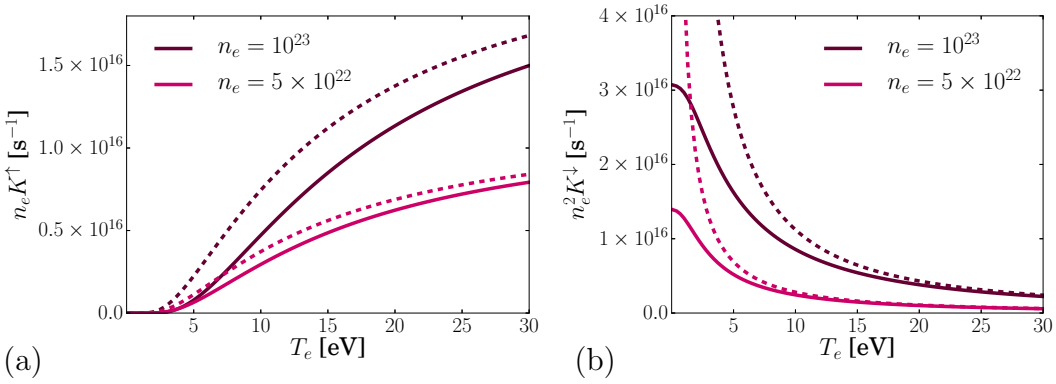

Figure 19: Comparison of (a) collisional ionization and (b) three body recombination rates of neutral carbon, with electron densities as indicated, computed with the Maxwell-Boltzmann (dashed line) and Fermi-Dirac (solid line) energy distributions.

$$F(\epsilon_0)\tilde{F}(\epsilon_1)\tilde{F}(\epsilon_0-\epsilon_1-E_i) = \exp\left(\frac{\epsilon_0-2\mu-E_i}{T_e}\right)F(\epsilon_1)F(\epsilon_0-\epsilon_1-E_i)F(\epsilon_0)$$
$$= \exp\left(-\frac{\mu+E_i}{T_e}\right)F(\epsilon_1)F(\epsilon_0-\epsilon_1-E_i)\tilde{F}(\epsilon_0), \quad (138)$$

where the labels FD and T_e have been dropped for brevity. The factor $\exp(-[\mu + E_i]/T_e)$ may be factored out of the integral in Equation (137), to obtain the relation

$$K^{\downarrow}_{FD} = \frac{g_i}{g_{i+1}}\frac{\exp(\mu/T_e)}{n_e}\exp\left(\frac{E_i}{T_e}\right)K^{\uparrow}_{FD}. \quad (139)$$

This relation also holds for the Maxwell-Boltzmann distribution if the chemical potential is taken to be $\mu = \bar{\mu}$, as defined in Equation (77).

3.3.5 Photoionization and radiative recombination

A photon whose energy exceeds the ionization energy of a given ion, $\epsilon_\gamma > E_i$, may be absorbed and strip off an electron by the process of photoionization,[78] also called bound-free absorption. Inversely, lone electrons recombining with ions must give off their kinetic energy and liberated potential energy via a photon. Schematically, this is

$$X_{i,j} + \gamma \rightleftharpoons X_{i+1,j'} + e^-.$$

The rate of photoionzation is given by

$$\mathcal{R}_{\text{photoionization}} = \left[IL^{\uparrow}\right]N_i, \quad (140)$$

where $L^{\uparrow}$ is the rate coefficient and I is the intensity of radiation. It is useful to group the term in square brackets (which appears in the rate matrix) into a normalised flux $\Phi = IL^{\uparrow}$, in units of s^{-1}.

The intensity is chosen for its experimental relevance, though it is qualitatively different to the usual product of spatial particle densities in Equation (89). Intensities, normally given in units of W cm^{-2} must first be converted into units of eV cm^{-2} s^{-1} by the electric charge constant. We must add an extra factor of ϵ_γ^{-1} to the rate integral calculation as the intensity is in effect the product of the number of photons with their energy. We use the fact that the speed of photons is approximately fixed (if the index of refraction is largely independent of photon energy) to enable us to convert the intensity (in units of eV cm^2 s^{-1}) to the spatial photon density (in units of cm^3) through a factor of c.

The rate coefficient for a given ionization stage is therefore given by

$$L^{\uparrow} = \int_{E_i}^{\infty} \sigma^{\triangle}(\epsilon_\gamma) \frac{f_\gamma(\epsilon_\gamma)}{\epsilon_\gamma} \mathbb{B} d\epsilon_\gamma, \tag{141}$$

where $\sigma^{\triangle}(\epsilon_\gamma)$ is the cross section (the symbols $\triangle$ and $\bigtriangledown$ are used for radiative cross sections to distinguish them from their collisional counterparts), which can be estimated by *ab initio* quantum mechanical calculations or obtained empirically. The energy distribution of photons $f_\gamma(\epsilon_\gamma)$ may be quite arbitrary, but we are particularly interested in black-body radiation, discussed above, and laser pulses which we model by $f_\gamma(\epsilon_\gamma) = \delta(\epsilon_\gamma - E_{laser})$.

An analytical expression for the photoionization cross section of hydrogen-like ions is given by[79]

$$\sigma^{\triangle}_{(\mathrm{Hydrogen-like})}(\epsilon_\gamma) = \frac{6.3 \times 10^{-18}}{Z^2} \left(\frac{E_i}{\epsilon_\gamma} \right)^3. \tag{142}$$

Photoionization cross sections of arbitrary ions tend to decrease above threshold as a similar function of the photon energy, typically between ϵ_γ^{-2} and ϵ_γ^{-3}. Although each ionization stage generally has an independent cross section value, to first order it can be approximated as that of the neutral atom provided that the photon energy is sufficient,

$$\sigma_i^{\triangle} \simeq \sigma_0^{\triangle} \Theta(E_i - \epsilon_\gamma), \tag{143}$$

where Θ is the Heaviside step function.

Lasers in the EUV range, whose photon energy is typicaly just above the first ionization energy of most atoms, have close to maximum photoionization cross sections.

Therefore, at sufficiently high intensities, the rate of photoionization dominates over other collisional and radiative processes.

The inverse process of radiative recombination has a rate given by

$$\mathcal{R}_{\text{radiative recombination}} = \left[n_e L^{\downarrow}\right] N_i. \tag{144}$$

To calculate the rate coefficient we use the detailed balance Milne relations,[78]

$$2 g_{i,j} m_e c^2 \epsilon_0 \sigma^{\triangledown}(\epsilon_0) = g_{i+1,j'} \epsilon_\gamma^2 \sigma^{\triangle}(\epsilon_\gamma). \tag{145}$$

We can substitute this relation into the appropriate form of Equation (90) and shift the integration limits as usual, to obtain

$$L^{\downarrow} = \frac{g_{i+1,j'}}{g_{i,j}} \frac{1}{2 m_e c^2} \sqrt{\frac{2}{m_e}} \int_{E_i}^{\infty} \epsilon_\gamma^2 \sigma^{\triangle}(\epsilon_\gamma) \frac{f(\epsilon_\gamma - E_i)}{\sqrt{\epsilon_\gamma - E_i}} \mathbb{B} d\epsilon_\gamma, \tag{146}$$

where f is now the electrons' energy distribution function. We can obtain an analytic solution for the Maxwell-Boltzmann distribution and the hydrogen-like photoionization cross section, which is known historically as Kramer's formula:

$$L^{\downarrow} = \frac{g_{i+1,j'}}{g_{i,j}} \frac{E_i^3}{Z^2 T_e^{3/2}} \exp\left(\frac{E_i}{T_e}\right) \mathbf{E}_1\left(\frac{E_i}{T_e}\right). \tag{147}$$

The photoionization cross sections can vary somewhat between different ions and even between the ionization stages for a given ion, but the formulae above generally hold to a good degree of accuracy.

3.3.6 Autoionization and dielectronic recombination

An ion where two of the electrons are excited above the ground state, such that the sum of the exctiation energies is greater than the ionization energy of a single electron, may eject an electron through the process

$$X_{i,j''} \rightleftharpoons X_{i+1,j} + e^-.$$

The second excited electron decays to the ground state to facilitate this transition. The total rate of this process, termed autoionization, is given by

$$\mathcal{R}_{\text{autoionization}} = [Q^{\uparrow}] N_{i,j}. \tag{148}$$

As there is only a single free electron participating in the interaction, calculation of the rate coefficient $Q^{\uparrow}$ through Equation (90) would lead only to an integral over a delta function - in effect, all the energies for a given transition are fixed. Therefore,

the simplest approach to obtain the coefficients of autoionization processes for given transitions is to consult tabulated values. In a degenerate plasma, a single factor of $\tilde{F}(E_i - E_{j''})$ must be added to account for Pauli blocking, where $E_{j''}$ is the sum of the excited energies.

The inverse process, called dielectronic recombination, has a rate given by

$$\mathcal{R}_{\text{dielectronic recombination}} = [n_e Q^{\downarrow}] N_{i,j}. \tag{149}$$

The rate coefficient may be deduced directly from the principle of detailed balance and is given in a non-degenerate plasma by

$$Q^{\downarrow} = G \frac{g_{i,j''}}{g_{i+1,j}} \exp(-E_{j''}/T_e) Q^{\uparrow}. \tag{150}$$

Electrons are excited to the levels participating in autoionization by the usual collisional-radiative processes, as discussed above. Similarly, ions may stabilize to the ground state through emission of radiation following dielectronic recombination.

3.3.7 Bremsstrahlung and its inverse

An accelerating charge emits photons in processes such as synchrotron emission. Electrons in a plasma continuously emit such radiation, called bremsstrahlung - German for "braking radiation" - or sometimes referred to as free-free emission, when deflected by collisions with ions. The classical limit of Equation (19) - Larmor's formula - for a single accelerating charge is $P = e^2 a^2 / 6\pi\varepsilon_0 c^3$, where a is its acceleration. A single electron in a plasma generally has $a^2 \propto 1/\sqrt{\epsilon}$, with the constant of proportionality determined by analysis of Coulomb collisions. We quote the classical result[78] for the Larmor radiation from an electron in a plasma, multiply by the density of electrons and integrate over the Maxwell-Boltzmann energy distribution to obtain the spectral intensity of bremsstrahlung radiation,

$$I_{BR}(\epsilon_\gamma) = n_e \int_{\epsilon_\gamma}^{\infty} \frac{e^6}{6\sqrt{6}\pi^2 \varepsilon_0^3 h (m_e c^2)^{3/2}} \left[\sum_{i=1}^{Z} i^2 N_{i,j} \right] \frac{f_{MB}(\epsilon_0)}{\sqrt{\epsilon_0}} d\epsilon_0 \tag{151}$$

$$= \frac{e^6}{3\sqrt{6}\pi^{5/2} \varepsilon_0^3 h (m_e c^2)^{3/2}} \frac{n_e}{\sqrt{T_e}} \exp\left(-\frac{\epsilon_\gamma}{T_e}\right) \sum_{i=1}^{Z} i^2 N_{i,j}. \tag{152}$$

This classical formula has found widespread use, although more complex formulae exist which take account of collective plasma scattering processes,[80] as well as quantum and relativistic effects. The absolute radiated intensity is given as usual by $I = \int_0^\infty I_{BR}(\epsilon_\gamma) d\epsilon_\gamma$.

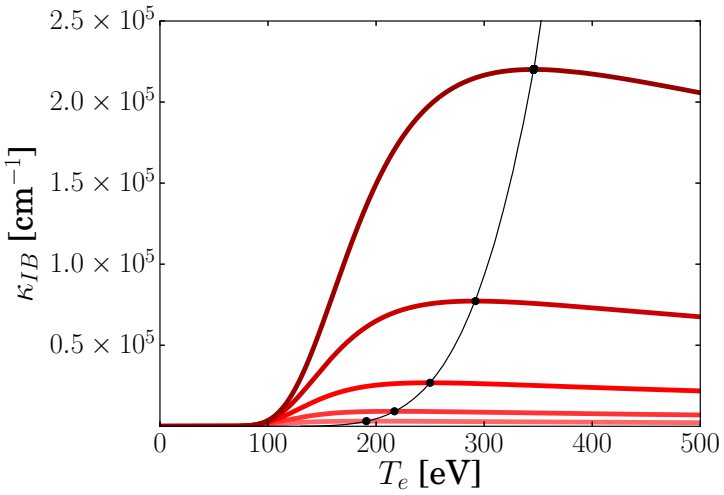

Figure 20: Inverse bremsstrahlung coefficient for photon energy of 50 eV in carbon as a function of temperature for logarithmically spaced densities from 0.1× (light) to 1× (dark) solid density. The peaks are marked by black dots; peak position as a function of T_e is denoted by the black line. The ion populations and electron density are calculated assuming steady state, as detailed in §3.

The unimaginitively named process of inverse bremsstrahlung has a significant impact on the kinetic energy density of electrons. Photons are absorbed by electrons in the presence of ions to conserve momentum, as opposed to a process such as Compton scattering. As with all absorption processes, it is possible to assign an absorption coefficient κ_{IB}, such that the attenuation of intensity and increase of free kinetic energy is given by

$$\frac{dI}{dx} = \frac{d\varepsilon}{dt} = I \int_0^\infty \kappa_{IB}(\epsilon_\gamma) f_\gamma(\epsilon_\gamma) d\epsilon_\gamma. \tag{153}$$

Requiring that emission and absorption be equal in equilibrium (where the radiation takes the black-body spectrum), we arrive using detailed balance at the absorption coefficient:

$$\kappa_{IB} = \frac{1}{6\sqrt{6}\pi^{5/2}} \frac{e^6 (hc)^2}{\varepsilon_0^3 (m_e c^2)^{3/2}} \frac{n_e}{\sqrt{T_e}\epsilon_\gamma^3} \left[1 - \exp\left(-\frac{\epsilon_\gamma}{T_e}\right)\right] \sum_{i=1}^{Z} i^2 N_{i,j}. \tag{154}$$

Other suggestions for the absorption coefficient exist,[81] but the functional dependence on a system's parameters of Equation (154) is universal. In particular, inverse bremsstrahlung becomes less pronounced at higher temperatures and high photon energies (where edge absorption and pair production[78] become dominant). However, the process dominates at low temperatures and high densities and continues

to be significant at intermediate temperatures, where the ions reach high ionization stages.

3.3.8 Continuum lowering

The discussion thus far has assumed that atomic physics in a plasma are identical to that of isolated atoms in free space. In such a case, electrons orbit a central potential and interact only with the nucleus and themselves. Even the presence of neighbouring neutral atoms leaves the energy levels and ionization energies largely unchanged, as long as the density of these atoms is sufficiently low. However, the mobile charges in a hot dense plasma can deform the central atomic potential and hence lower the ionization energy from its vacuum value,

$$(E_i)_{\text{effective}} = E_i - \Delta E. \tag{155}$$

This process is termed "continuum lowering" or "ionization potential depression".

An accurate quantative expression for continuum lowering remains an unsolved problem in plasma physics and the subject of intense debate. One leading expression is due to Stewart and Pyatt:[82]

$$\Delta E_{SP} = \frac{T_e}{2(\langle Z \rangle + 1)} \left[\left(\frac{3(\langle Z \rangle + 1)(i+1)e^3 n_e^{1/2}}{4\pi\varepsilon_0^{3/2} T_e^{3/2}} + 1 \right)^{2/3} - 1 \right], \tag{156}$$

where $\langle Z \rangle = \sum_{i=0}^{Z} i^2 N_{i,j}/n_e$ and i corresponds as usual to the ionization stage. This expression was derived by considering the time-averaged effect of a Fermi-Dirac distribution of free electrons penetrating inside the orbital radius of bound electrons. An alternative model is the modified Ecker-Kröll,[83]

$$\Delta E_{EK} = \frac{ze^2}{4\pi\varepsilon_0} \left(\frac{3}{4\pi(n_e + N_i)} \right)^{1/3}, \tag{157}$$

where the quantity in brackets is also referred to as r_{EK}, the Ecker-Kröll radius.

Before comparing the models to empirical data, we may observe several problems by inspection of these formulae. Quantum effects, such as the deformation of the bound electrons' wavefunctions by mobile charges, do not appear in either expression; by contrast, they appear prominently in collisional rate calculations in the form of the cross sections. Relativistic effects - unimportant for the free electrons - must be considered in the calculation of wavefunctions for high-Z atoms, but they do not appear in these two formulae either. Finally and perhaps most importantly, the expressions contain no time-dependent components; all the above-mentioned

atomic processes have a characteristic timescale, such as the electron equilibration time, and we can expect a similar effect to take place with continuum lowering.

The lowering may be sufficient enough that high-lying atomic levels cease to exist. If the lowering is even higher, entire ionization stages may disappear into the continuum. There are several approaches to incorporating this fact into plasma models. Fictitious and very large ionization rates may be introduced to empty those levels which lie above the continuum. Alternatively, the populations may be "dumped" into the nearest existing higher ionization state, with an accompanying rise of electron density and with the energy by which the continuum is lowered into the kinetic energy of the free electrons.

Experimental studies of continuum lowering have thus far taken emission spectra from dense plasmas and attempted to fit synthetic spectra, generated by collisional-radiative models with a given ΔE model. The disappearance of emission lines above certain temperatures and densities is a strong indication that those levels have disappeared due to contiuum lowering. The Stewart-Pyatt model matches several buried layer experiments,[84] while a version of the modified Ecker-Kröll has successfully matched XFEL experiments.[85] There have been suggestions to explain these differences and address some of the shortcomings of these two models.[86] In particular, the approach considers a view of thermodynamic processes, which range from instant to adiabatic.

3.4 Steady state ionization balance

We can expect a plasma to come into some sort of equilibrium when the left hand side of Equation (85) vanishes, that is $\frac{d\vec{N}_{ss}}{dt} = \vec{0}$. However, it is not possible to invert the rate matrix to find $\vec{N}_{ss}$ in this case, as it is singular; if it were not singular and an inversion were possible, then the only steady state solution would be $\vec{N}_{ss} = 0$. Instead, we impose an additional condition that the total density of ions in the system is fixed to N_T: $\sum \vec{N} = N_T$, or equivalently, as a scalar product $(1 \ \ldots \ 1)^\dagger . \vec{N} = N_T$. This allows us to write

$$M_{br}\vec{N}_{ss} = (0 \ \ldots \ 0 \ \ N_T)^\dagger, \tag{158}$$

where M_{br} is equivalent to the ordinary rate matrix M with the bottom row replaced by ones. An inverse, M_{br}^{-1}, can now be found and Equation (158) inverted to find $\vec{N}_{ss}$.

The system of rate equations in Equation (85) is not linear, however. The rate

matrix M depends on n_e, which is itself calculated from the corresponding ion densities by quasineutrality. This problem is made tractable by recasting to first calculate n_e by using Brent's algorithm to find the roots of

$$n_e - \sum_{i,j} i\vec{N}_{ss}(n_e) = 0, \tag{159}$$

where $\vec{N}_{ss}$ is found at each iteration by the inversion of Equation (158). The ionization fraction as a function of temperature for carbon is compared between the code developed as part of this work, `CRABS`, and a commercial code, `PROPACEOUS` (see §3.6). `CRABS` uses the LAPACK routine `gesv`, which performs the matrix inversion required for Equation (158) through an LU decomposition.[87]

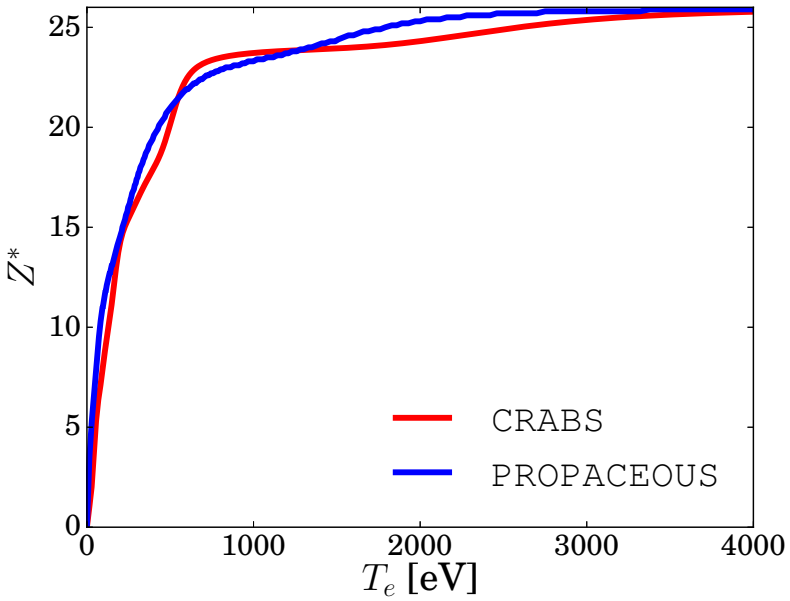

Figure 21: Comparison of the steady state ionization fraction $Z^* = n_e/N_T$ of solid density iron as a function of temperature computed by the code `CRABS`, developed as part of this work, to the commercial code `PROPACEOUS`. The differences arise from the atomic levels, cross sections and in particular the continuum lowering models used by the codes.

The steady state electron density calculated using this method for carbon ions, with the degenerate and non-degenerate rates, is shown in Figure 22. We see that the differences are small without any incoming radiation, as the electrons are never simultaneously cold or dense, as required for the chemical potential to deviate from its Maxwell-Boltzmann value $\bar{\mu}$. However, a strong flux of photoionizing radiation is able to create a very appreciable electron density even at low temperatures and therefore the effects of degeneracy are important.

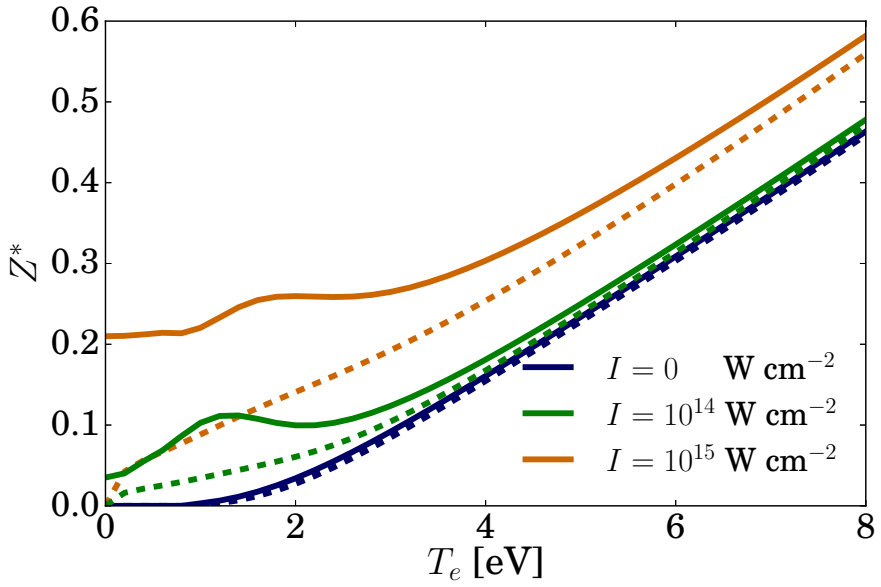

Figure 22: Comparison of the steady state ionization fraction of a carbon plasma (density of 2.23 g cm^{-3}, corresponding to graphite) for Fermi-Dirac (solid) and Maxwell-Boltzmann (dashed) statistics, irradiated by 50 eV photons at intensities indicated.

3.5 Classification of equilibria

It is possible, in principle, to solve the rate matrix equation for the ion populations, electron density and kinetic energy at a grid of different spatial points in a plasma. Such a model may take input, such as the total ion density, the flux of radiation, *etc.* from other calculations. In this approach, it is extremely costly computationally to define the rate matrix at a sufficient number of time points. The plasma quantities in such calculations will always tend to their equilibrium values, which may be obtained by solving Equation (159). This generic plasma state is referred to as the Collisional-Radiative Steady State (CRSS); we will discuss how often this is practically the case in a changing plasma in §4. In both cases, the success of the model depends on the accuracy of atomic levels, cross sections and the continuum lowering model. There are several other types of equilibrium,[88] which lead to useful simplifications in certain specific cases.

If the density in a plasma is low, processes with weaker dependence on electron density tend to dominate. Therefore, spontaneous emission and radiative recombination dominate over three body recombination and collisional de-excitation processes in such a plasma. Only the dominant processes need to be considered. Populations of excited states can then be calculated simply by balancing spontaneous emission

with collisional excitation, $A_j N_{i,j} = n_e J^{\uparrow} N_{i,0}$. Such a plasma is said to be in Coronal Equilibrium (CE), like the relatively hot, low density plasma in a star's corona - the region above its surface which extends into space.

If the plasma density is high, collisional processes dominate over spontaneous emission and radiative recombination. In this case, the collisional rates are precisely in detailed balance. The ion populations are then independent of any cross sections, but the ratios of excited states are given by the Boltzmann relations. The ratios of populations of ionization stages, when the electron distribution is close the Maxwell-Boltzmann, is given by the Saha-Bolzmann equation,[89]

$$\frac{N_{i+1}}{N_i} = G \frac{\bar{g}_{i+1}}{\bar{g}_i} \frac{T_e^{3/2}}{n_e} \exp\left(-\frac{E_i}{T_e}\right), \tag{160}$$

where the effective degeneracies are given by $\bar{g} = \sum_j g_j \exp(-E_j/T_e)$. Such a plasma is said to be in Local Thermodynamic Equilibrium (LTE).

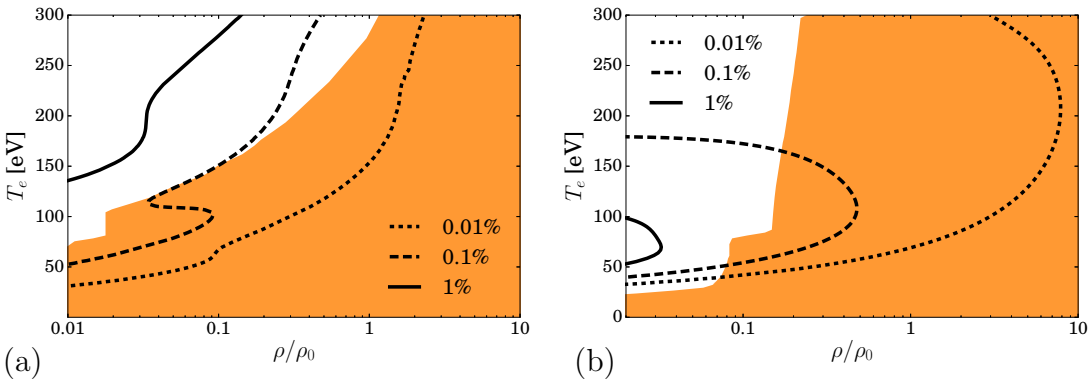

Figure 23: Deviation of relative ionization ($Z^* = n_e/N_T$) in steady state from LTE as a function of electron temperature and density for (a) iron (solid density $\rho_0 = 7.9$ g cm^{-3}); (b) carbon (solid density $\rho_0 = 2.3$ g cm^{-3}) as indicated. The shaded orange region indicates where the McWhirter criterion, given by Equation (161), holds.

McWhirter proposed a criterion[90,91] which allows a quick estimate if a plasma is in LTE, given in standard units by

$$n_e > 1.7 \times 10^{14} \sqrt{T_e} (E_j)^3. \tag{161}$$

This criterion was derived by insisting that the Van Regemorter excitation rate is at least 10× greater than spontaneous emission for some key excited states. Refinements to it have since been proposed.[92] We have evaluated the accuracy of this criteron by comparing it to the deviation of the ionization fraction $Z^* = n_e/N_T$ of LTE from CRSS in Figure 23. We see that it is close to the 0.1% deviation contour,

although for completeness we also require the condition $Z^* \leq ZN_T$ - a maximum of Z electrons are available per ion.

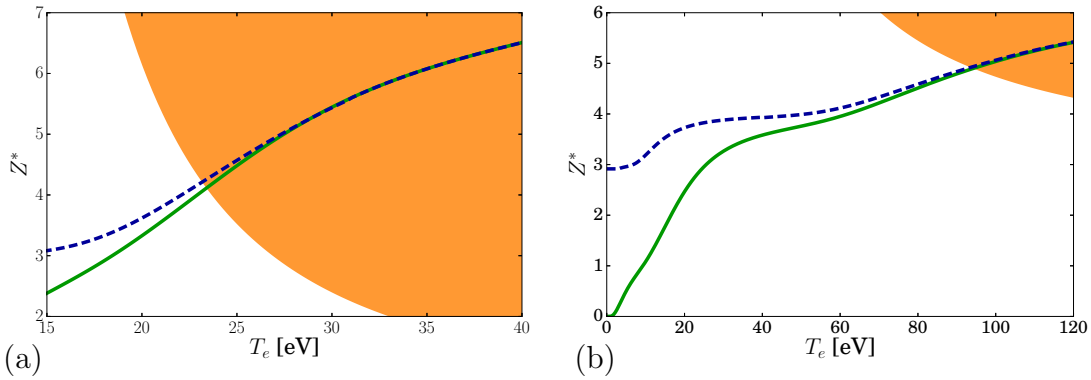

Figure 24: Comparison of steady state relative ionization as a function of electron temperature in the case of no photon irradiation (solid line, equivalent to LTE) and for constant irradiation by photons of energy 50 eV (dashed line) for (a) iron (density $\rho_0/10 = 0.79$ g cm^{-3}) (b) carbon (density $\rho_0/10 = 0.23$ g cm^{-3}), both at an intensity of 10^{15} W cm^{-2}. The shaded orange region indicates the region of validity of LTE as specified by Equation (163).

McWhirter's criterion for LTE interrogates the electron density. We can use a similar approach to McWhirter's in order to estimate if the flux of ionizing photons is low enough for the plasma to remain in LTE. We require that the Lotz rate of collisional ionization is at least $10\times$ greater than the rate of photoionization. We consider the photons to be monochromatic (for example from a laser) with a photon energy ϵ_γ. This condition can then be written as

$$n_e K^{\uparrow}_{i,j} N_{i,j} > 10 \frac{\sigma^{\triangle}}{\epsilon_\gamma} I N_{i,j}. \tag{162}$$

Taking the Lotz formula from Equation (122) for collisional ionization and a hydrogen-like photoionization cross section from Equation (142), we have in standard units,

$$n_e > 1.31 \times 10^8 \frac{\sqrt{T_e} I}{Z^2 \xi E_1(E_i/T_e)} \left(\frac{E_i}{\epsilon_\gamma}\right)^4 \Theta(\epsilon_\gamma - E_i). \tag{163}$$

We have compared the region of validity of this criterion to the CRSS ionization fraction with and without an incident flux of photons in Figure 24.

If the plasma is in LTE and furthermore the radiation field is given by the black-body distribution at the same temperature, the plasma is said to be in Thermodynamic Equilibrium (TE).

3.6 Codes and databases for collisional-radiative modelling

There are many published databases of atomic levels and transitions, of which one of the best maintained is the National Institute of Standards and Technology (NIST) database.[71] This database requires that the energies of levels be verified experimentally to a very high degree of accuracy and ranks the results by the inherent experimental uncertainty. A web interface also allows a synthetic emission spectrum to be displayed for a given electron density and temperature. A web portal to opacity codes of the Los Alamos National Laboratory (LANL)[21] contains many cross sections for atomic processes for low-Z elements. The web portal also allows approximate opacities of plasmas to be calculated.

To calculate atomic levels and some transition strengths from first principles, there is a code called `grasp2K`.[93] This atomic structure code uses the variational principle to calculate wavefunctions and corresponding energies, including relativistic effects which are important for high-Z atoms. The code has remarkable agreement with experiment, for a wide range of ions.

The code `PROPACEOUS`, part of the `PrismSPECT` suite,[94,95] is a commercially available code which calculates plasma parameters in LTE or CRSS. `PrismSPECT` is focused on 1-dimensional hydrodynamic simulation of laser- or ion-beam produced plasmas and generation of synthetic spectra, which are compared with experimental diagnostics. A similar online collisional-radiative code called `FLYCHK`,[96] which outputs plasma quantities and can be used to model emission spectra, is maintained by NIST.

4 Microscopic plasma models

Steady state situations, such the distribution of ions in LTE, are convenient for computing equation of state quantities and emission spectra. They are often used to efficiently perform inline calculations as part of radiation-hydrodynamic codes. However, steady state may only be reasonably assumed if there is sufficient time for energy to be redistributed between electrons and ions by collisions. In this chapter, we present a collisional-radiative code written to evaluate the timescales taken by plasmas to reach steady state, to confirm that these timescales are insignificant compared to hydrodynamic motion and to explore the transient behaviour of EUV laser-produced plasmas.

4.1 Code description

The self-consistent set of rate equations (as outlined in §3.2) are solved by a code called `CRABS`: routine for Collisional-Radiative ABSorption, written as part of this work. The focus of the code is to model the interaction of a strong photoionizing laser pulse with ion populations, and therefore radiation is modelled by a monochromatic distribution $f_\gamma(\epsilon_\gamma) = \delta(\epsilon_\gamma - E_{\text{Laser}})$. The photon energy E_{Laser} is in this case only slightly higher than the first ionization energy of atoms, maximising its photoionization cross section through Equation (142). `CRABS` can calculate rates from the Maxwell-Boltzmann distribution via the direct integral formulae or at a significantly higher computational cost from the Fermi-Dirac distribution via numerical integration. The resulting rate matrix can be used to calculate populations in steady state or to evolve them in time using a 4^{th}-order Runge-Kutta method, as discussed in Appendix B.6. `CRABS` can include continuum lowering (which may be switched "on" or "off") through the Stewart-Pyatt model, given in Equation (156). This model was chosen to be consistent with `POLLUX` and because it has been demonstrated to agree well with experiments performed on dense plasmas. `CRABS` does not model the motion of ions.

`CRABS` can solve a 0-dimensional model, which corresponds to either a small element of volume or a system which is very homogeneous. It has the option to extend to a 1-dimensional model, with the spatial axis corresponding to the propagation of a laser and discretised as shown in Figure 25. An individual collisional-radiative model is solved in a number of cells of thickness Δx. A laser profile propagates at a speed c, so that its intensity profile advances forward by one cell after a time $t = \Delta x/c$. At each timestep, the laser intensity is coupled to matter via the usual

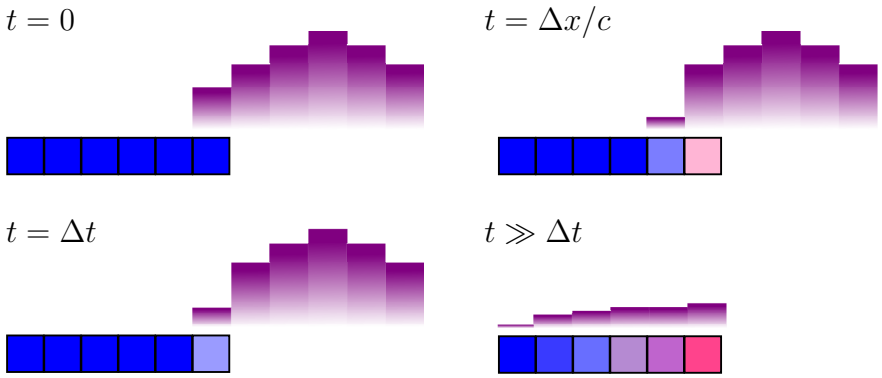

Figure 25: Schematic diagram of discretization of time and space in the CRABS code. The ion populations and electron temperature are solved for in each space cell and the opacity is calculated. A laser pulse is incident from the right and advances through the cells at times spaced by $\Delta x/c$. The laser is absorbed as it travels through the plasma, increasing the temperature.

radiative processes and is attenuated by

$$\frac{dI}{dt} = -c\kappa I, \tag{164}$$

where the total absorption coefficient is the sum of the photoionization and inverse bremsstrahlung coefficients $\kappa = \kappa_\Phi(E_{\text{Laser}}) + \kappa_{IB}(E_{\text{Laser}})$.

CRABS uses a simplified "superconfiguration"[97,98] atomic model with a ground state and a single effective excited level for each ionization stage, as discussed in Appendix D. The model's physical complexity is targeted at simulating the absorption of photoionizing radiation by dense matter. Although such an atomic model does not resolve individual quantum levels, as may be required to calculate the gain of a laser for example, it allows long-term simulation of plasma out of steady state. Atomic processes with insignificant rates (at the conditions considered in this work), such as dielectronic and radiative recombination, are ignored for the sake of performance. Autoionization is important only for x-ray photons with energies > 100 eV, sufficient to excite tightly bound electrons to the autoionizing states. The rate of three body recombination dominates over dielectronic recombination at higher densities[99,100] and towards solid, as we can see from the electron density dependence (n_e^2 and n_e) of the respective rates.

The radiation transport model considers only the propagation of a laser pulse along a single axis. This appears a gross simplification, compared to the radiation spectrum of plasmas containing many features from bremsstrahlung and line radiation across all solid angles. However, this uniaxial propagation and monochromatic

opacity model is accurate when the laser pulse is short and intense and therefore dominates over other radiative processes. The total ion density in each cell is kept constant, meaning that the model ignores hydrodynamic motion. This simplification is acceptable because the timescales of atomic processes are significantly shorter than those of any plasma fluid motion, as discussed below.

4.2 Plasma formation models

In order to verify `CRABS`, we compare results from a 0-dimensional run to an analytical solution of the rate equations which we derive below. We also consider the case of a 0-dimensional plasma being rapidly created from solid material by a large flux of short-wavelength radiation.

4.2.1 Analytical treatment of hydrogen

The atomic system of hydrogen has only two ionization stages; we consider in this example a fixed electron temperature without the effects of continuum lowering or any excited atomic levels above the ground state. This is the simplest possible system and perhaps the only one for which an analytic solution exists. For a fixed T_e, the collisional ionization and three body recombination rates, $K^{\uparrow}$ and $K^{\downarrow}$ respectively, are constant; all other rate coefficients are taken to be zero. In the usual notation, the population densities of the neutral and singly ionized hydrogen are denoted by N_0 and N_1 respectively. Now, the two coupled differential equations for population densities to be solved become

$$\frac{dN_0}{dt} = n_e^2 N_1 K^{\downarrow} - n_e N_0 K^{\uparrow}, \tag{165}$$

$$\frac{dN_1}{dt} = -n_e^2 N_1 K^{\downarrow} + n_e N_0 K^{\uparrow}. \tag{166}$$

As usual, there is a constant total ion density $N_T = N_0 + N_1$. Finally, since there is only a single electron per ionized atom, the electron density $n_e = N_1$. These two relations may be substituted into Equation (166) to give

$$\frac{dN_1}{dt} = N_1 N_T K^{\uparrow} - N_1^2 K^{\uparrow} - N_1^3 K^{\downarrow}. \tag{167}$$

Equation (167) is a nonlinear, first order ODE, whose exact solution is given by the following transcendental equation:[101]

$$t - t_0 = \frac{1}{N_T X} \operatorname{arctanh}\left(\frac{K^{\uparrow} + 2K^{\downarrow} N_1}{X}\right) + \frac{1}{2N_T K^{\uparrow}} \ln\left(\frac{N_1^2}{N_T K^{\uparrow} - N_1\left(K^{\uparrow} + K^{\downarrow} N_1\right)}\right), \tag{168}$$

where $X = \sqrt{4N_T K^{\uparrow} K^{\downarrow} + (K^{\uparrow})^2}$ and t_0 is some constant of integration. This solution may be simplified by assuming that three body recombination rate in Equation (167) is insignificant compared to collisional ionization (namely $K^{\downarrow} = 0$), which holds for high electron temperature. This yields a simpler solution,

$$t - t_0 = \frac{2}{N_T K^{\uparrow}} \operatorname{arctanh}\left(\frac{2N_1}{N_T} - 1\right). \tag{169}$$

Rearranging this relation yields the time dependence of the populations,

$$N_0 = \frac{N_T}{2}\left[1 - \tanh\left(\frac{N_T K^{\uparrow}}{2}(t - t_0)\right)\right], \tag{170}$$

$$N_1 = \frac{N_T}{2}\left[1 + \tanh\left(\frac{N_T K^{\uparrow}}{2}(t - t_0)\right)\right]. \tag{171}$$

If a rate coefficient $\Phi = IL^{\uparrow}$ corresponding to photoionization is included in this treatment, the equivalent of Equation (166) becomes

$$\frac{dN_1}{dt} = -n_e^2 N_1 K^{\downarrow} + n_e N_0 K^{\uparrow} + \Phi N_0. \tag{172}$$

Following the same treatment as above and with identical boundary conditions yields a slightly modified version of the analytical hydrogen equation,

$$N_1 = \frac{N_T}{2} - \frac{\Phi}{2K^{\uparrow}} + \left(\frac{N_T}{2} + \frac{\Phi}{2K^{\uparrow}}\right)\tanh\left(\frac{\left(N_T K^{\uparrow} + \Phi\right)}{2}(t - t_0)\right). \tag{173}$$

This result naturally reduces to the previous solution, given by Equation (171), in the absence of photoionization ($\Phi = 0$). The effect of photoionization is to increase the rate at which the system reaches equilibrium and creates an asymmetric tendency to ionize the atomic populations.

These two simple results, with and without incident photons, have been compared to corresponding numerical simulations in Figure 26. In this case, the total ion density $N_T = 10^{21}$ cm^{-3} and fixed electron temperature is $T_e = 25$ eV. The initial density of 1+ ions is zero in the photon case and small, but not zero in the non-photonic case to avoid the trivial solution. The computational results show remarkable similarity to the analytical case, although deviate slightly at later times because of the over-simplifying assumption that three body recombination $K^{\downarrow} = 0$ in the analytic case.

4.2.2 Plasma creation by EUV photons

It is useful to explore the creation of a plasma from cold solid matter by a constant flux of EUV photons. `CRABS` was run with a single spatial cell with the superconfigu-

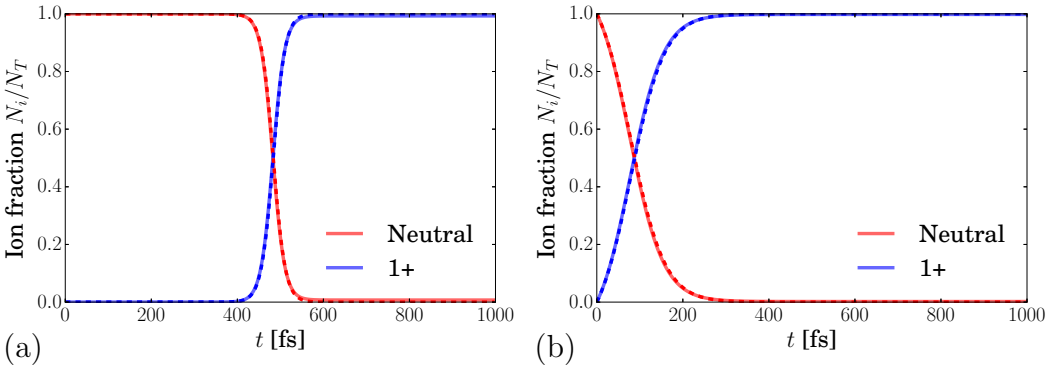

Figure 26: Populations of neutral and ionized hydrogen in a simplified model at a temperature $T_e = 25$ eV and a total density of $N_T = 10^{21}$ cm^{-3} (a) without incident photons with $N_1(0) = 10^5$ cm^{-3}; (b) with incident photons at a normalised flux of $\Phi = 10^{12}$ s^{-1} and with $N_1(0) = 0$ cm^{-3}. The computational results (solid) are compared to the analytical model (dashed).

ration atomic model of iron, constant irradiation with continuum lowering switched off. The plasma is initially at a temperature of $T_e = 0$; in the absence of continuum lowering, this corresponds to every atom being neutral. With the start of irradiation, the first free electrons are created solely by photoionization. Each electron gains an energy of $E_{\text{Laser}} - E_0 = 42.1$ eV, and it is assumed that it thermalises to a temperature of $T_e = \frac{2}{3}\varepsilon = 28.1$ eV. However, this high temperature is far out of equilibrium with the ionization distribution and unsustainable, leading to a fast drop in temperature as additional electrons are collisionally ionized.

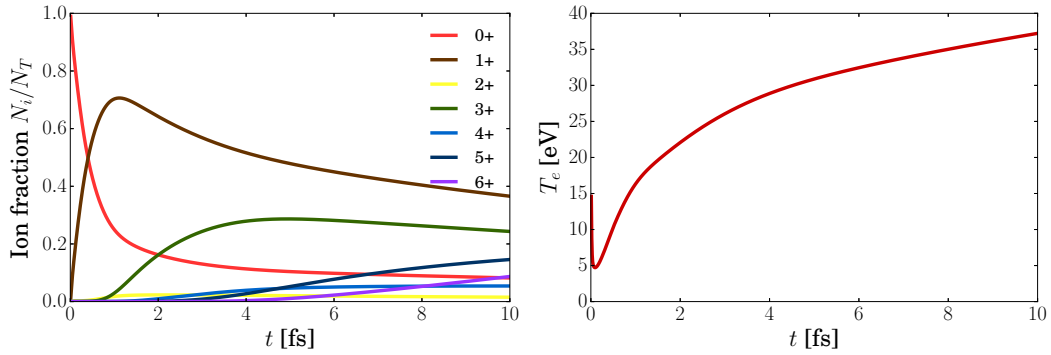

Figure 27: Evolution of populations of ions (as indicated) and electron temperature of solid density iron with an incident flux of 10^{15} W cm^{-2} of 50 eV photons. The populations of higher ionization stages (8+ and higher) are negligible in this case.

As the electron density of a forming plasma rises, inverse bremsstrahlung becomes more prominent at transferring energy from photons to electrons. Another process which begins to occur is a cycle of photoionization and three body recombination,

which in effect transfers the energy of a single photon to two electrons, without a net change in ionization. These two processes eventually cause the temperature fall to reverse at a minimum, followed by a steady ramp up. During this time, the ionization distribution approaches the instantaneous steady state conditions.

This simplified model demonstrates the nature of short wavelength laser-plasma interactions. A large density of free electrons is rapidly developed by photoionization; the original phase of the matter very quickly transitions to a dense plasma. We observe a fast drop in the initially high temperature, with a long-term linear rise comparable to optical lasers. The plasma is created on timescales much faster than those of hydrodynamic expansion (of the order of picoseconds), suggesting that solid density plasma may be created by short-wavelength lasers.

We can use a 0-dimensional simulation (with continuum lowering) to explore the effect of degeneracy on the creation of plasma by a laser pulse. We choose carbon as it is a common target material, is low-Z (therefore simple computationally), and accurate atomic data is readily available. Degeneracy is strongest when electron density is high and temperature low. Therefore, a pulse which ionizes strongly and heats weakly creates maximally degenerate plasma; a short, but intense pulse with photons just above the first ionization energy fits these criteria.

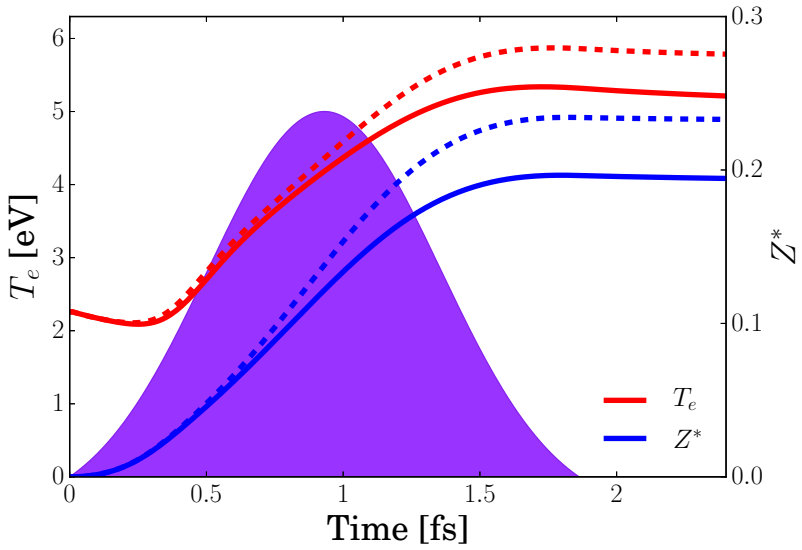

Figure 28: Evolution of the electron temperature and ionization fraction of carbon (density of 3.53 g cm^{-3}, corresponding to diamond) irradiated by a laser beam with photon energies of 14 eV and Gaussian intensity as shown shaded with a full-width half maximum of 1 fs and a peak intensity of 10^{14} W cm^{-2} with the Maxwell-Boltzmann (dashed line) and the Fermi-Dirac (solid line) statistics as indicated.

The results of simulations with the Fermi-Dirac and the Maxwell-Boltzmann distributions are compared in Figure 28. We have chosen an ion density corresponding to diamond, the most dense known condensed state of carbon. The laser photons have an energy of 14 eV, only slightly above $E_0 = 11.25$ eV in a realistic temporally Gaussian pulse of 1 fs duration.

The simulations begin identically, as there are insufficient electrons for degeneracy to take effect for the first ~ 0.2 fs. Thereafter, the Fermi-Dirac model has a lower ionization fraction due to reduced ionization rates, as a result of blocking factors appearing preferrentially in the ionization rates (see formulae for $K^{\uparrow}$, $L^{\uparrow}$). This results in a higher kinetic energy per electron, but this is compensated by the larger heat capacity and therefore the temperature is lower in the Fermi-Dirac model. These quantities equilibrate to steady-state values during the tail end of the laser pulse.

We have considered a "worst case scenario" regarding the degeneracy of electrons. A typical laser pulse is likely to be significantly longer and reach much hotter final temperatures, where the two energy distributions become identical. Hydrodynamic expansion at longer timescales would also act to lower the electron density and therefore the degree of degeneracy. It is therefore justifiable to use the Maxwell-Boltzmann distribution to model most short-wavelength laser interactions.

4.3 Time to steady state

We have previously discussed the deviation of a solid-density plasma in steady state from LTE. We are also interested in quantifying how quickly a plasma reaches similar steady state conditions. Plasmas may be rapidly heated by thermal conduction or streaming fast electrons, if not directly by laser radiation.

We consider the plasma to be in CRSS at a starting temperature of $T_s = 25$ eV. This plasma is relatively cold, but not degenerate, so that excessive computation is not required. The amount of energy required to raise the temperature to some final value T_f is calculated by considering the plasma's total heat capacity. This energy is transferred to the kinetic energy of the electrons ε at a linear rate during a deposition time t_d, but without a flux of photons. If the energy were deposited instantaneously ($t_d = 0$), the temperature would exceed T_f - kinetic energy would require time to be transferred to the potential energy of ions. Likewise, although for $t_d \neq 0$ the energy rise is linear, the temperature rise is not. At each timestep after t_d, the five most populated ionization stages are compared to their values in CRSS

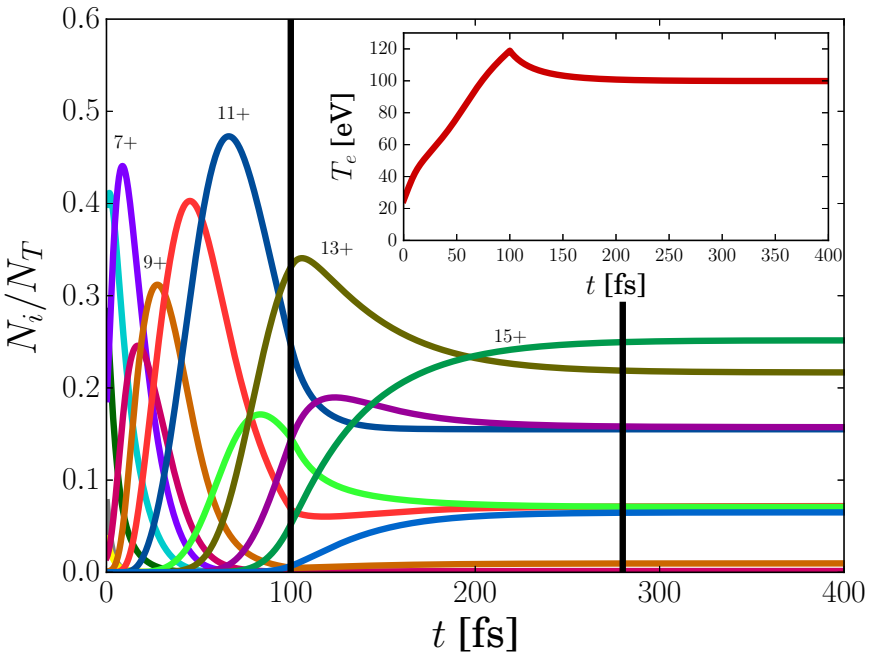

Figure 29: Ionization populations (as labelled) and temperature (inset) as a function of time during a linear energy deposition causing the initial electron temperature $T_s = 25$ eV to increase to $T_f = 100$ eV for iron plasma at $10^{-1/2}\times$ solid density. The end of the deposition time at 100 fs and the subsequent equilibration time 180 fs later are indicated by vertical lines.

at T_f. When the deviation of each one is less than 1%, the plasma is considered to have equilibrated, with an equilibration time t_{eq} as measured from t_d.

The results of a 0-dimensional `CRABS` simulation following the scheme above, with $t_d = 100$ fs and $T_f = 100$ eV, are plotted in Figure 29. We see a rapid evolution of ion populations during the time of energy deposition. When energy deposition stops, the temperature begins to relax to T_f asymptotically, though its time dependence cannot be described by elementary functions. The ion populations tend to steady state in a similar manner. This asymptotic behaviour explains why the equilibration threshold is set to a finite value (in this case 1%). Due to the nature of the rate equations, the asymptotic approach takes infinitely long to precisely reach steady state.

It is important to consider the equilibration time of electrons, because `CRABS` assumes that the electrons instantaneously arrive at an appropriate Maxwell-Boltzmann distribution regardless of the rate of deposition of energy. We therefore require that $t_{eq} \gg t_{e-e}$, where the Spitzer electron-electron equilibration time is given by Equation (64). It is also important to consider the timescales for energy transfer to

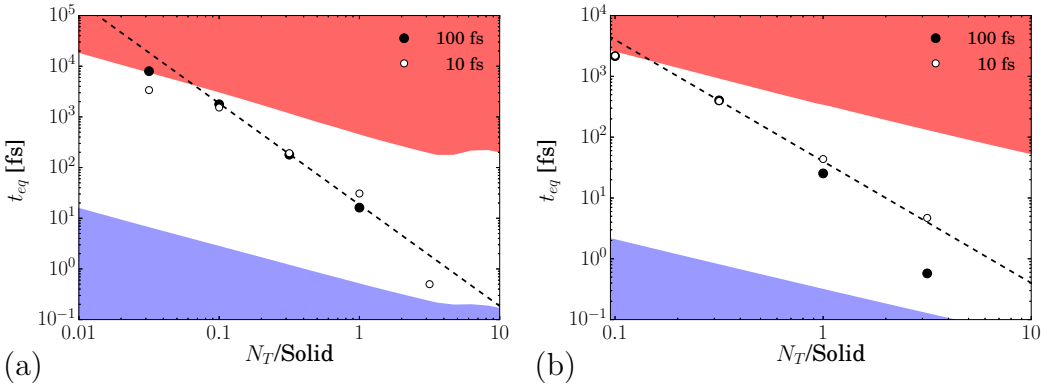

Figure 30: Equilibration times as a function of total density as a fraction of solid for (a) iron and (b) carbon. Simulations were run with $T_s = 25$ eV and $T_f = 100$ eV with a deposition time t_d as indicated. A trend-line of the equilibration times proportional to N_T^{-2} is plotted. The region where electrons have insufficient time to thermalise is coloured blue; it is bounded by the electron-electron equilibration time t_{e-e}. The region where electron-ion energy transfer begins to occur is coloured red; it is bounded by t_{e-i}.

ions. It may be expected that some energy be lost to ions as the plasma tends towards TE, where $T_e = T_i$. We therefore require that $t_{e-i} \gg t_{eq}$, where the Spitzer electron-ion time is given by Equation (65), in order that the assumption that the ion temperature is unchanged holds.

The results of a parameter scan of total ion density for carbon and iron are shown in Figure 30. The density range covers values relevant for short wavelength and intense optical laser experiments. We see a general decrease in equilibration time with density, closely following a trendline with an inverse quadratic dependence on density. At very high densities, the equilibration time vanishes and hence does not appear on the logarithmic plot in Figure 30.

The electron density at a given temperature tends to increase with total ion density, particularly due to continuum lowering, leading to an overall increase in the atomic rates ($\propto n_e, n_e^2$). In steady state, when rates are balanced, their absolute magnitude is not important. However, high rates hasten the response of a system to transient events, such as the energy deposition considered here, and hence t_{eq} decreases with total ion density. As the atomic rates become higher, the ion populations follow their instantaneous steady state values more closely during energy deposition. At some point, this deviation from CRSS falls below the 1% equilibration threshold and the equilibration time vanishes.

The appropriate energy distribution equilibration times are also plotted in Figure

30, evaluated at the final electron temperature. We confirm that below $\sim 5\times$ solid density the electrons reach a Maxwell-Boltzmann distribution much faster than the atomic processes modelled in `CRABS`. Above this density continuum lowering models have not been experimentally verified, hence there is large uncertainty in theoretical models. We see also that above $\sim 0.1\times$ solid ion density, the electron-ion equilibration time becomes comparable with t_{eq}, and hence the assumption that the ion temperature remains constant no longer holds.

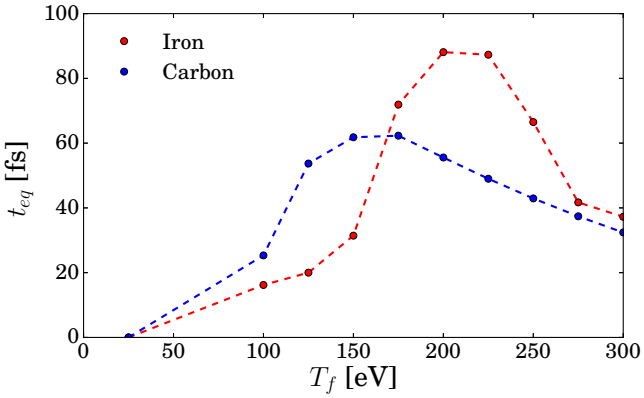

Figure 31: Variation in equilibration time t_{eq} as a function of final temperature T_f for iron and carbon at solid density with deposition time $t_d = 100$ fs and starting temperature $T_s = 25$ eV.

The effect of the final temperature T_f on the equilibration time is plotted in Figure 31, at solid ion density. In both cases, we see the equilibration time rise to a peak and then begin to fall off with increasing T_f. It is intuitive that as the system is driven to a higher final temperature, the populations are further from the final steady state and, hence the equilibration time increases. However, above a certain point, steady state populations cease to vary significantly with temperature. Given this lack of variation, it is easier to reach steady state in this case and hence the equilibration time drops at high temperatures.

4.4 Bleaching wave propagation

Having explored the interaction of lasers with an infinitessimal region of plasma, we are interested in exploring the axial propagation of laser radiation. We have seen that photoionization can dominate the absorption of radiation and can deplete ionization stages with ionization energies exceeded by the photon energy. Conversely, we can expect absorption to stop once these ionization stages are depleted. The

corresponding drop in opacity is termed "bleaching", with a spatial and temporal behaviour akin to a propagating wave as discussed below.

Prior to simulating bleaching using the 1-dimensional mode of `CRABS`, we can derive an analytic model. Consider the spatial equivalent of Equation (164), with radiation propagating from negative to positive x,

$$\frac{dI}{dx} = -\kappa I. \tag{174}$$

We expect the radiation to be strongly attenuated in regions of high absorption and conversely the intensity to be high in regions where bleaching has taken place. Therefore, we can expect the absorption coefficient to behave as $\kappa(x) \propto I_0 - I(x)$, where I_0 is the peak intensity. The mathematical treatment in this case is reminiscent of the analytical model of hydrogen, with

$$I(x) = \frac{I_0}{2}\left[1 - \tanh\left(\frac{\kappa_0}{2}(x - x_0)\right)\right], \tag{175}$$

$$\kappa(x) = \frac{\kappa_0}{2}\left[1 + \tanh\left(\frac{\kappa_0}{2}(x - x_0)\right)\right], \tag{176}$$

where κ_0 is the unperturbed absorption coefficient and x_0 is a constant of integration. We see that at a given point in time, the point x_0 is a measure of how far the radiation has propagated. We expect this point to propagate with time as the bleaching process occurs. The speed of propagation may be derived by considering the energetics of the interaction; it is given by the ratio of the flux of radiation to the energy density required in order to fully bleach the opacity, namely

$$\frac{dx_0}{dt} = \frac{I_0}{\varepsilon_{\text{bleach}}}, \tag{177}$$

where

$$\varepsilon_{\text{bleach}} = \sum_{i=0}^{Z} N_{i,j} E_i \Theta(E_i - \epsilon_\gamma). \tag{178}$$

It should be noted that the bleaching wave is a collective excitation, rather than a particle and is therefore not restricted by relativity. In the lab frame, therefore, it is possible for the bleaching wave to propagate faster than c.

The discussion so far has focused on the case where the opacity is dominated by photoionization, which decreases as radiation is absorbed. However, inverse bremsstrahlung tends instead to increase with continued ionization, as it has a strong dependence on the electron density and the charge states of ions. Therefore, this treatment applies to low-density material, where inverse bremsstrahlung is weak.

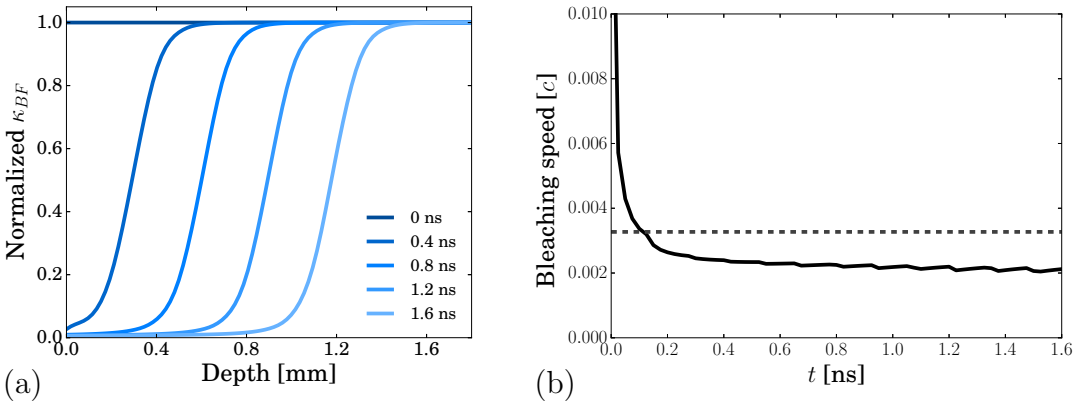

Figure 32: (a) The normalised photoionization absorption coefficient of helium at atmospheric pressure ($N_T = 2.5 \times 10^{19}$ cm^{-3}) during irradiation by a laser pulse with a flat profile, $E_{\text{Laser}} = 26.5$ eV and $I_0 = 10^{10}$ W cm^{-2}. (b) Simulated speed of propagation of the bleaching wave dx_0/dt (solid), defined as the point where the normalised absorption coefficient takes a value of 0.5, and analytic value (dashed).

Results of a 1-dimensional `CRABS` simulation of atmospheric density helium, for a laser with $E_{\text{Laser}} = 26.5$ eV and a constant intensity profile, are shown in Figure 32. Helium was chosen as its ionization energy of $E_0 = 24.6$ eV is narrowly above this chosen laser photon energy, which is relevant to capillary discharge lasers, as discussed in §5. We see that this fully collisional-radiative model confirms that the absorption coefficient is bleached and verifies our very simple analytical model of bleaching propagation. Plotted also is the speed of the bleaching wave, which tends to a constant value. Although inverse bremsstrahlung was simulated, its effect was small, because the density of gas at atmospheric pressures is low and helium is a low-Z element.

The simulated bleaching velocity tends to a value of $2.2 \times 10^{-3}c$, which is remarkably close to the theoretical value computed from Equation (177), which is $3.27 \times 10^{-3}c$. This similarity can be improved further, if the heat capacity of the free electrons is included in Equation (178), assuming the end with a temperature $T_e \simeq 10$ eV.

We consider a similar interaction, but with two temporally Gaussian laser pulses of differing peak intensity in Figure 33. The laser is incident on a region of finite thickness of helium (properties identical to those above) and measured after emerging from the region of helium. We see that for the more intense pulse, the first third of the pulse is strongly attenuated as the opacity is bleached and thereafter the pulse is not affected. However, the less intense pulse does not contain enough energy to bleach the helium completely and is therefore completely absorbed.

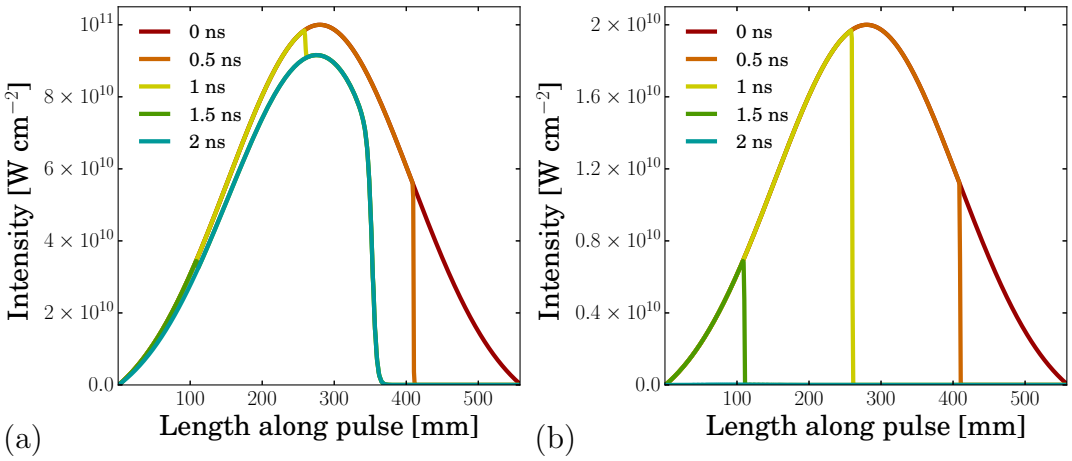

Figure 33: Temporal variation of a Gaussian laser pulse with peak intensities of (a) 10^{11} W cm^{-2} and (b) 10^{10} W cm^{-2} incident on 2 mm thick region of helium. $E_{\text{Laser}} = 26.5$ eV and $N_T = 2.5 \times 10^{19}$ cm^{-3} as in Figure 32.

The paradigm discussed above offers an interesting effect, which may be explored experimentally. Any focused laser pulse will form a Bessel profile in space, as discussed in §2.1. The attenuation of the pulse, when interacting with a region of helium, will therefore be spatially dependent and produce a modified profile. The diffraction-limited focused profile of a capillary discharge laser and the effect of attenuation of a region of helium are shown in Figure 34a.

At a distance of one focal length beyond the interaction region, the laser pulse expands to its original size. In the absence of any interaction, an identical image of the beam would be formed here. In the case of a beam from a capillary discharge laser, this profile is annular as discussed in §5.2.2, with a local minimum at its centre. After an interaction, the image would be modified by diffraction. In this case, the central minimum of the profile is less pronounced.

An experiment may therefore be conducted, whereby a laser pulse propagating through vacuum is focused onto a helium gas jet. Local gas pressures of the order of several atmospheres can be readily achieved inside a high vacuum (required for EUV laser propagation) by such jets.[102] Precise measurements may be taken by imaging the beam with a CCD before and after the interaction. This is shown in Figure 34c with simulated idealised CCD images of the beam before and after the interaction with the helium jet. The peak absorption coefficient scales linearly with the total ion density and therefore the 2 mm region mentioned above may be shrunk or expanded as necessary by control of the gas pressure. This may be necessary depending on the focal length of the optic used - it is required that the region of interaction be much shorter than the length scale for the spatial profile to change significantly.

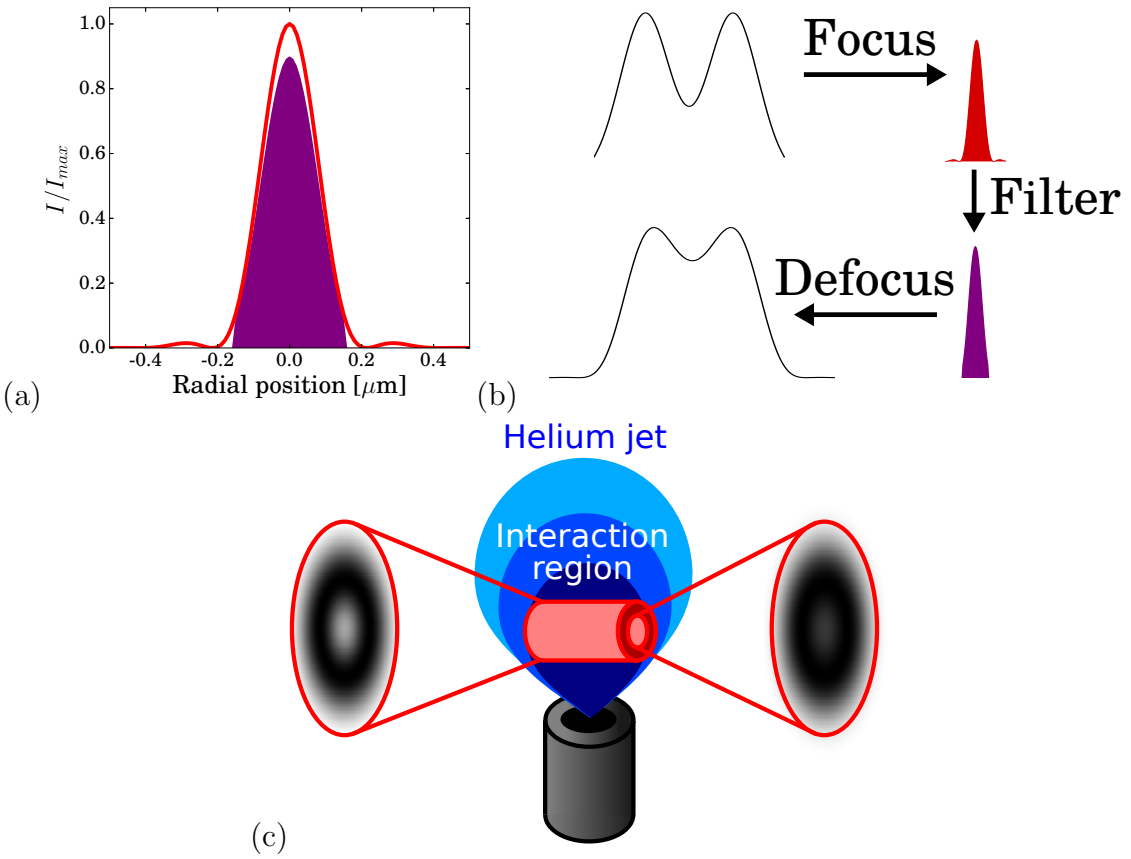

Figure 34: (a) The focused spatial intensity profile of a capillary discharge laser (solid) and the profile resulting from the interaction with a region of helium (shaded). (b) Schematic diagram for a proposed experiment: an initially annular profile is focused onto helium, has attenuation based on the peak intensity and has a modified profile when defocused. (c) Sketch to illustrate the proposed experimental setup. The annular beam from a capillary discharge laser (as shown on the left) is focused onto a helium jet. Comparison of the beam profiles before and after the interaction allows the plasma to be diagnosed.

It is more difficult to observe similar bleaching waves in solid density materials, because of the effect of inverse bremsstrahlung. It is clear from Equation (154) that the inverse bremsstrahlung absorption coefficient strongly depends on density and the charge of the ions in a plasma. This coefficient would therefore be much higher in plasmas created from typical solid laser targets, made of plastics or metals, compared to the helium gas jet considered above.

The results of a `CRABS` simulation of carbon at solid density, with constant irradiation by EUV photons, are shown in Figure 35. We see that the opacity due to photoionization is bleached at early times, as predicted by Equations (175) and (176). However, the absorption due to inverse bremsstrahlung quickly grows as the

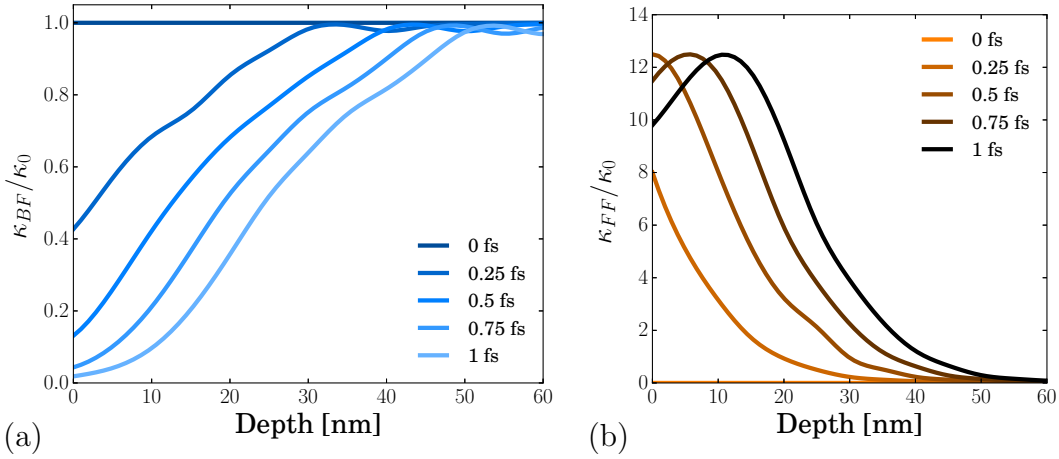

Figure 35: The contribution to the absorption coefficient due to (a) photoionization and (b) inverse bremsstrahlung for solid density carbon irradiated by photons with intensity $I = 10^{14}$ W cm^{-2} and photon energy $\epsilon_\gamma = 26.5$ eV at times indicated. The coefficients are normalised to the photoionization coefficient for neutral carbon.

electron density and average charge state of the ions increases, exceeding the initial photoionization coefficient κ_0 by an order of magnitude. Absorption by inverse bremsstrahlung begins to fall only when the plasma has been heated to moderately high temperatures ($\gtrsim 50$ eV in this example). The laser radiation is being absorbed by this method to directly heat the electrons, preventing its propagation further into the target. For such high density targets, it is difficult to observe a bleaching of opacity before strong hydrodynamic expansion begins to occur.

5 EUV transmission experiments

In this chapter, we discuss laser experiments performed at the Department of Electrical and Computer Engineering of Colorado State University (CSU). Many short-wavelength radiation sources have been developed at the EUV Engineering Research Center.[37] In particular, a number of compact EUV capillary discharge lasers are in operation at CSU, two of which have been used for this work. These capillary lasers operate on the $1s^2\ 2s^2\ 2p^5\ 3p\ {}^1S_0 \rightarrow 1s^2\ 2s^2\ 2p^5\ 3s\ {}^1P_1$ transition of Ar^{8+} (neon isoelectronic sequence), with a corresponding photon energy $\epsilon_\gamma = 26.5$ eV. The argon is initially confined in a long alumina capillary and a population inversion is achieved by a rapid electrical discharge, as detailed in §1.2.2.

The experiments aimed to create and probe a solid density plasma by the capillary discharge laser, while also setting out experimental techniques to be used for future, larger-scale experiments. The experiments allowed the benchmarking of the hydrodynamic code `POLLUX`, as well as the diffraction codes written as part of this work. We have exploited two different versions of the capillary discharge laser, with similar properties. Each version employed a separate focusing geometry: a Fresnel zone plate (FZP) and a spherical multilayer mirror (MLM). The FZP is part of an ablation mass spectrometry system, with an older laser. The MLM experiment was attached to a newer laser system, development of which has recently been completed.

The focused laser caused ablation of thick solid targets in initial experiments, leaving an ablation crater. The craters could then be analyzed by microscopes, which allows direct comparisons with `POLLUX` simulations. The depth of these craters (which is a parameter that may be easily quantified) was much less than the target thickness, so that simulations treated their extent as semi-infinite. Targets sufficiently thin to be ablated by a single shot were also used, allowing a portion of the beam to be transmitted through the target and imaged. The thickness was chosen so that a single shot had sufficient energy for a significant fraction to be transmitted.

Targets

Parylene-N was chosen as the main target material for the experiments. It is a resilient plastic composed of equal proportions of carbon and hydrogen. This composition simplifies the hydrodynamic modelling by `POLLUX`, as well as other codes used for spectroscopy studies. As a plastic, it can be manufactured into a range of self-supporting structures, or cut in the laboratory. Aluminium was used as a secondary target material.

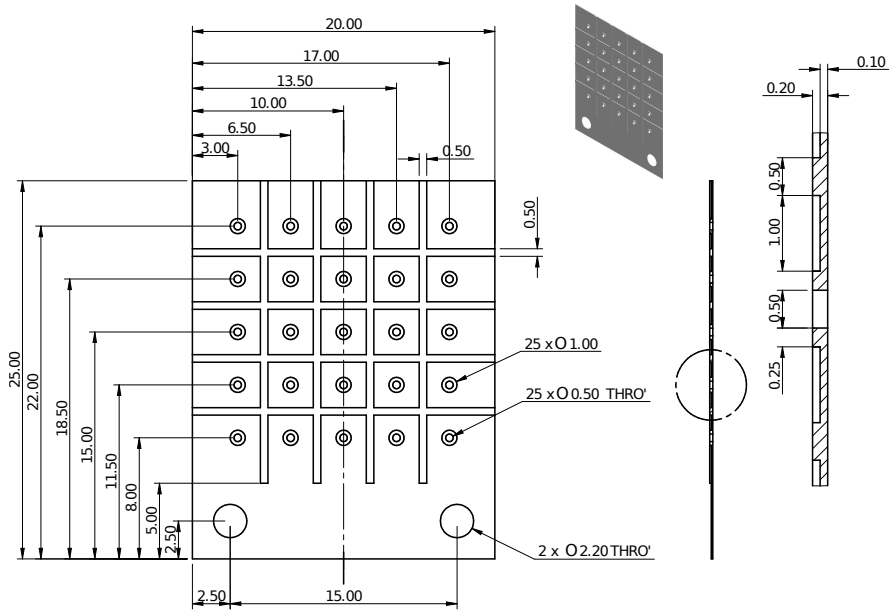

Figure 36: Engineering drawing[103] (dimensioned in mm) of the target holders for the parylene-N targets produced by the target fabrication group at the Central Laser Facility (CLF).

For the transmission experiment, films of two thicknesses, 429 nm and 1028 nm, were produced and characterised by the target fabrication group of the Central Laser Facility (CLF). The films were attached to rigid aluminium holders, as shown in the engineering drawing in Figure 36. The films were stretched over a regular grid of 0.5 mm diameter holes to form the targets. As a secondary target material, aluminium foils of 1.2, 2.5 and 25 μm were mounted onto several target holders at CSU after removal of the parylene-N films.

5.1 Zone plate focus experiments

A Fresnel zone plate (FZP) is used to achieve a tight focus, with intensities up to 10^{10} W cm^{-2}, as part of a previously established ablation mass spectrometry experiment. In a mass spectrometer, ions are accelerated by a DC voltage, allowing the mass to charge ratios of the constituent ions to be determined; in this case, a laser-produced plasma is the source of ions.[11] The narrow focal spots allow a 3-dimensional map of isotope compositions to be built up from a given sample. The experimental setup used for mass spectrometry (with thick targets) is shown in Figure 37, with the transmission experiment inset.

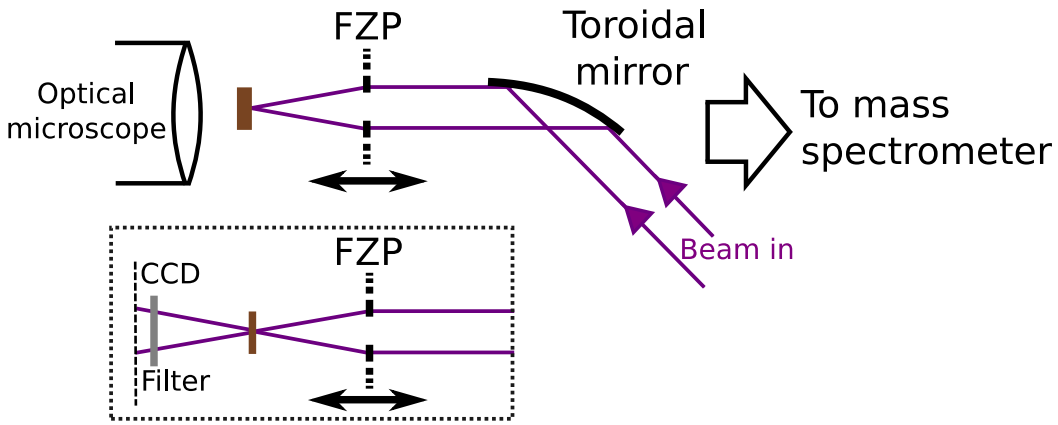

Figure 37: The focusing geometry using a zone plate to ablate thick targets (top), as part of the ablation mass spectrometry experiment at CSU.[11] The setup used to image a beam transmitted through thin targets (inset).

5.1.1 Focal geometry

The FZP parameters are given in Table 4. To allow the plasma to be extracted, a central opening is created by removing the first few zones. The laser beam is guided to the experiment by toroidal gold grazing-incidence mirrors with high reflectivity. These mirrors were used to transfer the beam through the experimental setup; focusing was achieved solely by the FZP. Capillary discharge lasers typically have an annular profile, as characterised in §5.2.2, which expands to a diameter of several millimetres when it reaches the experiment. The size of the FZP is limited to a much smaller diameter by the size of the outer zone, meaning that only 3.1% of the total laser energy is delivered to the target.

Focal length	2.1 mm
Outer diameter	0.5 mm
Outer zone width	200 nm
Number of zones	$\sim$ 625
Central opening	50 μm

Table 4: Physical parameters of the Fresnel zone plate used in experiments at CSU.

The FZP has a very short focal length, making it challenging to achieve a good focal spot. The zone plate's mount is motorised, so that it may be positioned to within 1 μm of the focal distance away from the target's surface. An optical microscope is used to confirm ablation of the target by visual observation.

To image the beam as it is transmitted through a thin target, the optical micro-

scope was replaced by an Andor DO436 CCD. This model was chosen as it has a very large range of photon energy response (10^{-2} to 10^{3} eV). It can capture photons for times > 100 ms, which is sufficient to capture a whole laser shot sequence, but must subsequently digitise for approximately 3 seconds, which is very slow compared to the maximum repetition rate of this type of argon-based capillary discharge laser. The pixel size is 13.5 μm, which provides sufficient resolution to image the details in the transmitted beam; 2048 pixels in each dimension give a length of 27.6 mm on each side, which is sufficient to image the entire beam up to several metres from the capillary. Each pixel on the CCD has a maximum possible response, after which it saturates, continuing to saturate neighbouring pixels and possibly to damage the detector. To adjust the intensity response of the CCD and protect it from saturation, a filter must be used.

We have used specially constructed aluminium filters with thicknesses of between 0.5 and 1.2 μm, attached to a 1" circular steel holder. The holders were mounted in slots on a protective metal screen, which was designed to shield the CCD from stray light entering the vacuum chamber and debris created by ablation. This setup allowed multiple filters of different thicknesses to be used to attenuate the beam by the required amount.

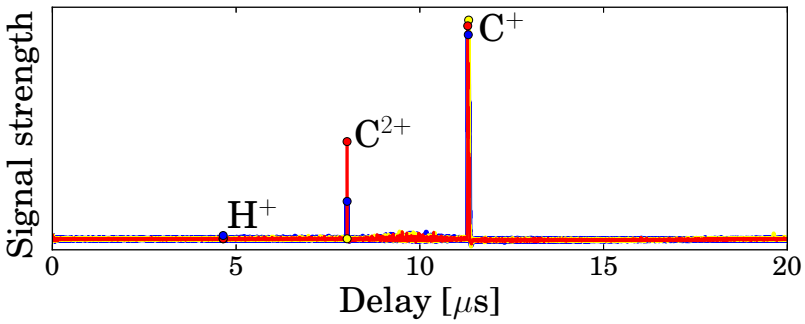

Figure 38: Signals from the mass spectrometer for three shots (as coloured). The peaks are labelled with the corresponding elemental ionization stage. The differences in the three cases are caused by slight variations in the focal intensity.

Removing the optical microscope to mount the CCD made it difficult to find the position of the focal spot. We found that the mass spectrometer's signal could be used to determine when significant ablation was occuring and hence when the target was at the focal point. The spectrometer measures a time-resolved voltage signal proportional to the density of passing ions. The time of flight of the ions is a function of their mass to charge ratio. With the optical microscope attached, we have identified peaks corresponding to the first two charge states of carbon when

ablation was occuring. The mass spectrometer signals for three shots at focus are shown in Figure 38 after the optical microscope was replaced with the CCD, so that the transmitted beam could be imaged.

5.1.2 Ablation results

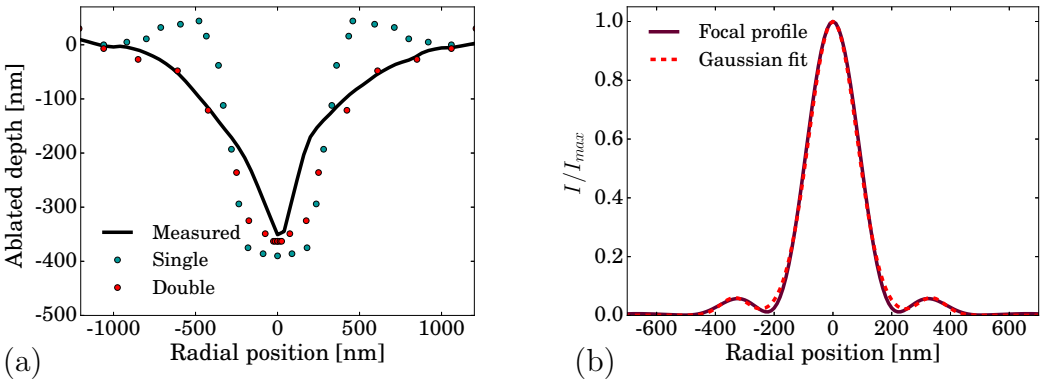

Figure 39: (a) Measured ablation profile, compared to POLLUX simulations with a single central Gaussian peak and the predicted double peak, as indicated. Experimental data supplied by Ilya Kuznetsov; POLLUX simulations were performed by Andrew Rossall.[3] (b) Normalised intensity profile for zone plate parameters in Table 4, 8 μm away from the nominal focal distance. An analytic fit of a central Gaussian peak, along with a side lobe, is also shown.

The ablation craters created on the surface of the thick targets were scanned by an atomic force microscope (AFM). This method yields high-resolution measurements of the surface depth, building up a 3-dimensional nanoscale image. A line out through the centre of a crater is shown in Figure 39a. We compare this profile to the depth of solid density material remaining after laser interactions in POLLUX simulations.

As a purely hydrodynamic code, POLLUX requires a relatively simple spatial intensity profile. By default, such a profile is Gaussian to match the diffraction-limited beams of optical lasers. However, 1-dimensional diffraction calculations show the presence of side lobes, as shown in Figure 39b, for a distance along the beam axis z at or close to the focal point. These lobes have been parameterized via a second offset Gaussian, with an intensity of 6% of the central peak. This profile has been incorporated into POLLUX by Andrew Rossall, allowing good agreement to be found with the measured crater.[3]

Using the mass spectrometer to achieve a focus, we were able to successfully

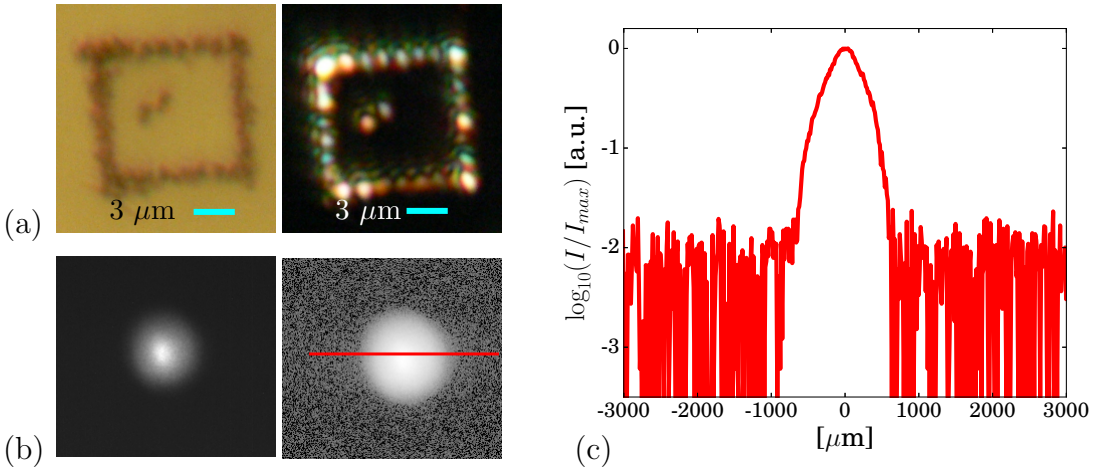

Figure 40: (a) Reflection and transmission micrographs of the target surface at 100× magnification. (b) Raw and background subtracted CCD images of the transmitted beam. (c) Line out of the logarithmic intensity profile recorded by the CCD at a distance of 416 mm beyond the target.

ablate the 429 nm parylene-N targets and record the transmitted intensity. Micrographs of the target region, after the surface was coated in gold by vapour deposition, are shown in Figure 40a. The opaque coating was added to improve the contrast of the micrographs. The transmitted laser beam forms an intensity peak, which has been captured by the CCD as shown in Figure 40b. The raw CCD images contain a background with a vertical gradient, which can readily be subtracted. A logarithmic line out of this intensity peak is shown in Figure 40c. An absolute spatial scale is obtained from the pixel size (13.5 μm), with the CCD positioned 416 mm from the target.

Ablation of the 429 nm parylene-N was simulated in `POLLUX`; the resulting density at two simulation times is shown in Figure 41. The intensity profile used is that of Figure 39b; the focused laser had a full-width half maximum (FWHM) of approximately 200 nm and peak intensity of approximately 10^{10} W cm^{-2}. The final result of such simulations is a hole with a diameter of 630 nm. The thin targets lacked the tensile strength to be measured by the AFM, so a direct comparison to `POLLUX` simulations could not be made. An extreme upper bound on the hole size can be obtained from their pattern on the target surface. Shots were made at intervals of 1 μm in a closed loop. If the diameter of the holes exceeded this spacing, the enclosed region would fall away. Although the holes are close to the microscope's resolution limit, we are able to estimate their diameter at 700 nm from the optical micrographs.

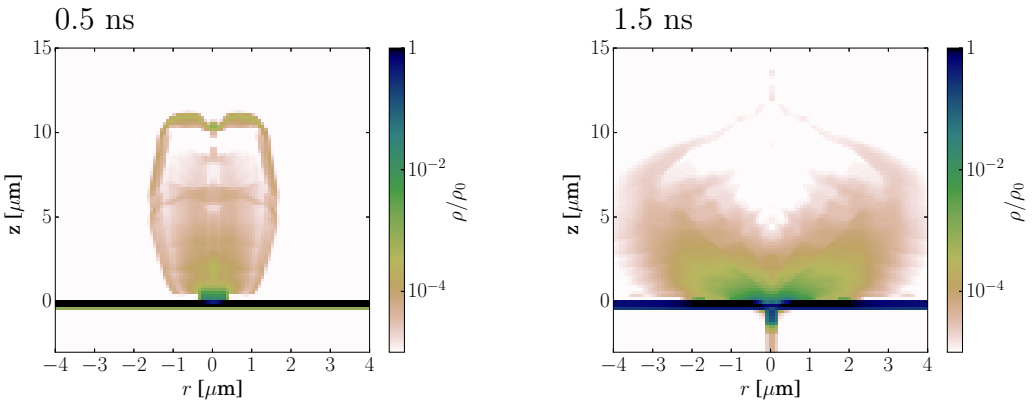

Figure 41: Density profiles computed by POLLUX normalised to solid density ρ_0 at times indicated. The EUV laser is incident from the top of page, centered on $r = 0$. The intensity profile used is identical to that in Figure 39b, with a peak intensity of 10^{10} W cm^{-2}.

5.2 Multilayer mirror focus experiments

A newly developed capillary discharge laser was used for the ablation experiments with a multilayer mirror focusing geometry. This laser is a prototype of a system which has been developed to enter serial manufacturing and to be sold to academic and industrial users as a single unit, produced by XUV Lasers, Inc. The operational parameters are shown in Table 5. As the first scientific experiments conducted with the laser system, the undertaking described in this section was used to improve the design specifications for future laser units. The multilayer mirror was able to achieve peak intensities of $\sim 3 \times 10^{10}$ W cm^{-2}, exceeding those of the FZP. Previous experiments using argon capillary discharge lasers with MLMs have shown successful ablation of solid density targets,[104] motivating the present work.

Wavelength	46.9 nm
Repetition rate	< 10 Hz
Pulse duration (FWHM)	~ 1 ns
Pulse energy	< 50 μJ
Beam divergence	~ 5 mrad

Table 5: Operational parameters of the capillary discharge laser developed by XUV Lasers, Inc. The peak repetition rate, pulse energy and beam divergence were verified during experiments described here and are discussed further below.

The capillary discharge laser is extremely compact compared even with laboratory optical lasers, as shown in Figure 42. The main cylindrical tank contains the

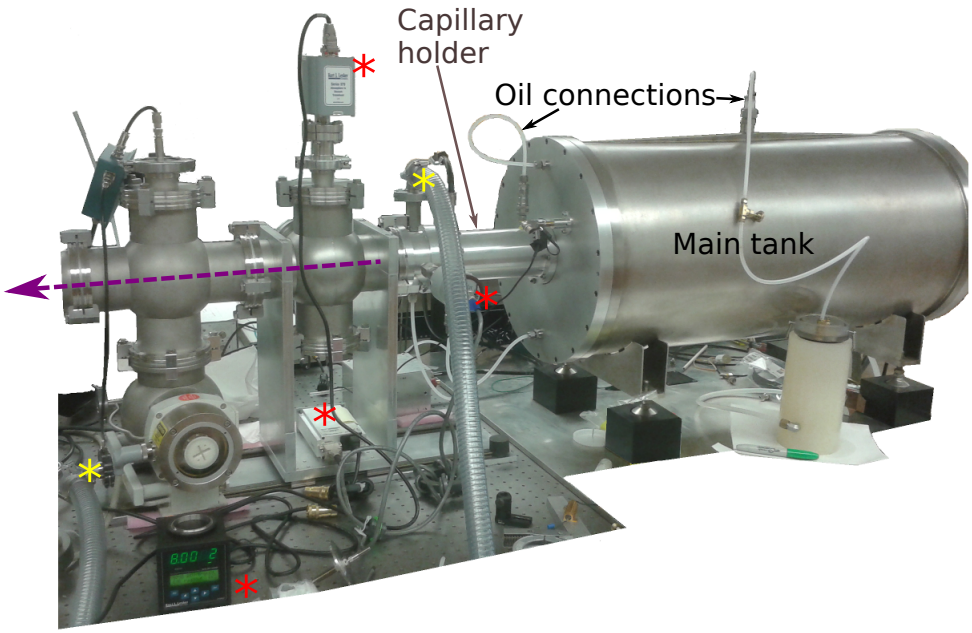

Figure 42: Image of the prototype capillary discharge laser of XUV Lasers, Inc. used in experiments. The main features and approximate beam line of the laser are labelled; in addition asterisks label the vacuum pumps (yellow), vacuum gauges and their displays (red). The total setup pictured is approximately 1.5 m in length.

capacitors and electronics required to produce the 18 kA discharge with $\sim$ 30 ns rise time leading to lasing. Biodegradable dielectric oil is used both as an insulator and as a coolant, with connections between parts of the laser and to a spillover tank as shown in Figure 42. The alumina capillary is located in a holder which extends from the main tank. An argon tank and roughing pump connected to the capillary ensure an appropriate background pressure of 40 Pa for lasing. The laser beam passes out of the capillary holder through a pinhole, into two vacuum chambers containing diagnostics and then to the main experimental chamber. This pumping geometry maintains the lasing pressure required in the capillary and a reasonable vacuum of 10^{-3} Pa in the experimental chamber.

5.2.1 Experimental setup and preliminary measurements

We have used a Sc/Si multilayer coating on a concave spherical glass substrate to focus the 46.9 nm beam onto the target; its properties are given in Table 6. As the CCD must be mounted on an NW-50 flange, the beam had to be guided to a wall parallel or perpendicular to the original beam propagation and therefore a "Z" configuration with a second, identical mirror to recollimate the beam was used as shown in Figure 43. The collimating mirror (M2) had a higher surface

roughness than the focusing mirror (M1) and had experienced damage, leading to lower performance. In practice, the entire target holder shown in Figure 36 proved too wide to be inserted into the "Z" experimental configuration without clipping the laser beams. Vertical cuts were made to isolate a strip with a single column of targets. The mirrors were tilted by an angle $\alpha = 4.7°$ to the incoming beam.

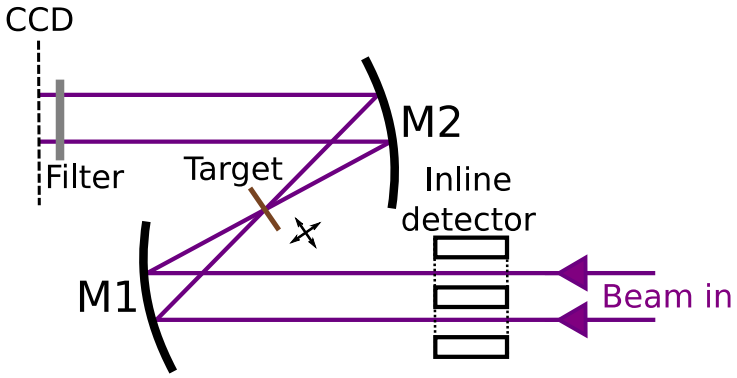

Figure 43: Experimental setup for the multilayer mirror (MLM) ablation experiment.

Reflectivity (46.9 nm)	$\sim 40\%$
Radius of curvature R_c	10 cm
Transverse radius R_m	0.5"
Scandium layer	11.0 nm
Silicon layer	13.7 nm
Interface layer	3 nm

Table 6: Physical properties of the multilayer mirrors used. The reflectivity and interface layer thickness are an estimate observed to agree with previous experiments.[105]

The experiment was contained in an experimental chamber, connected by a bellow directly to the laser setup shown in Figure 42. The experimental chamber had dimensions (in mm) of 560×475×382 and did not require independent pumping. The optical components shown in Figure 43 were supported by holders attached to an optical breadboard on the bottom of the experimental chamber. The targets were supported on a motorised mount with three linear degrees of freedom, with a minimum step size of 0.1 mm in each direction, which allowed the focal spot to be located in the z dimension and shots to be made on target at intervals in the (x,y) plane. When replacing one type of target with another (for example, of different

thickness), it was not possible to maintain the z position to an accuracy better than ~ 0.3 mm. Ablation results were obtained for a range of focal positions defined by this uncertainty. However, as the focal profile is spatially extended by the large tilt angle of the MLM, this accuracy is sufficiently high compared to $f = 5$ cm (the focal length of the MLM) so that approximately the same peak intensity is achieved for the range of z. Nonetheless, accurate positioning remains a significant challenge in experiments with EUV radiation, as described in Chapter 2.

5.2.2 Beam profile

It is important to measure the intensity profile of the beam emerging from the laser as the unperturbed profile can then be used to calculate the intensity at the focal spot via diffraction integrals. We have measured the laser profile by placing a CCD just before the experimental chamber, at a distance of 745 mm from the end of the capillary. An image of the beam produced in this way is shown in Figure 44a. There is a large background signal due to long-timescale spontaneous emission from the argon plasma shining through an inline ionization detector (discussed in §5.2.3).

The laser beam forms an annular profile in the lower right of the image, narrowly clipping the detector. Background emission is removed by taking the difference of two pulses with different energies. Spontaneous emission mostly occurs during the compression phase of the capillary discharge laser, so it is not practically possible to produce a totally "dark" background signal. However, when comparing two pulses with different energies, the background remains almost constant, yielding a multiple of the laser signal. The background-corrected profile is shown in Figure 44b, where the structured background has disappeared to leave random noise and an intense signal.

To express the intensity as an analytical function, we fit to the difference of two lasing signals a pseudo-Gaussian function given by

$$I(r) = (A - c)\exp\left(-\frac{(r - r_0)^2}{w^2}\right) + c \qquad r \leq r_0, \tag{179}$$

$$I(r) = A\exp\left(-\frac{(r - r_0)^2}{w^2}\right) \qquad r > r_0, \tag{180}$$

where r is the radial distance from the centre of the profile and A, c, r_0 and w are fit parameters. Due to the CCD response, which can saturate at high intensities, this difference is not well defined in the region close to r_0. Therefore, this region was excluded from the fitting routine. The resulting fit is shown in Figure 44c. It

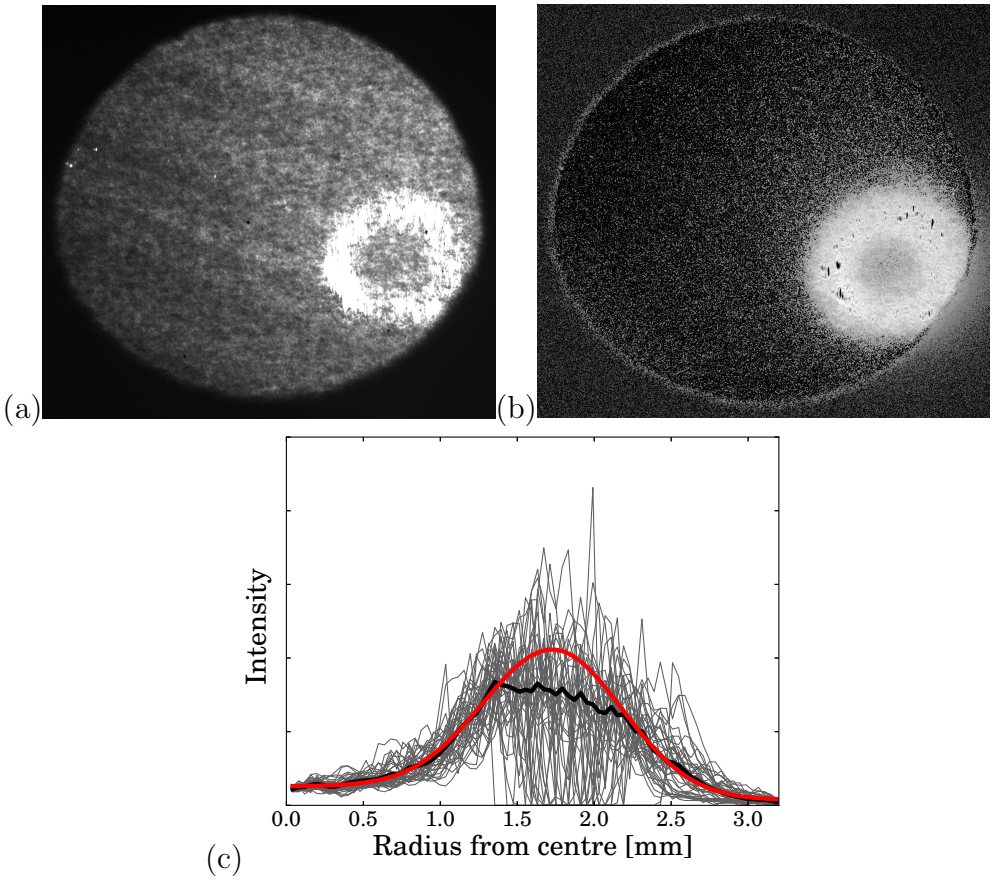

Figure 44: (a) The annular profile of the laser beam measured directly using the CCD, behind a 2.5 μm aluminium filter. The outer circular structure is due to the inline detector. (b) Difference of two laser pulses (each of differing energy) to remove background. (c) An average (black) over a number of line outs from the centre of the beam (grey) with background subtracted. An analytic function (red) fit to the profile is shown.

should be noted that this measurement does not provide an accurate value for the fluence of the laser and hence only the relative values of A and c are meaningful.

The 2.5 μm aluminium filter used to shield the CCD had striations, corresponding to imperfections in the rolled aluminium sheet as visible in Figure 44a. Visual inspection shows a small azimuthal asymmetry in the beam, as there are three distinct and separate groupings of black regions (one partially clipped by the inline detector) corresponding to regions of maximal intensity where the CCD has been saturated. It is difficult to confirm whether this effect is due to filter imperfections. This motivates a more careful determination of the intensity profile in future experiments.

5.2.3 Pulse energy measurement

Determination of the laser pulse energy enables the intensities at the laser focus to be deduced. As with most lasers, pulse energies of capillary discharge lasers vary from shot to shot, but they are perhaps more difficult to measure than usual due to the general lack of flexibility in EUV and soft x-ray optics. Due to the pulse energy variation, non-destructive measurements are desirable for every experimental shot.

We have used an inline ionization detector to measure pulse energies. The laser beam passes into a chamber, which is turbo-pumped, but nonetheless contains gas particles at pressures of 10^{-3} Pa. The beam is sent through a short cylindrical tube, with two electrodes biased to -2 kV at each end. The residual gas is ionized by the beam and creates an electrical signal, measured by the electrodes. The integrated signal is proportional to the pulse energy, though the precise relation depends on parameters such as the gas pressure and the proximity of the beam relative to the cylinder. The inline detector can provide accurate pulse energy measurements after calibration, provided that the experimental conditions are kept largely constant.

In order to calibrate the inline detector with an absolute measurement of the pulse energy, we have used a photodiode, which can be attached to the laser in place of the connection to the experimental chamber. The diode is biased to -2 kV and produces a voltage signal by electron photoemission when struck by the laser beam. The laser's pulse energy (typically reported in μJ) is related to the time-integrated voltage V through the relation

$$E_{\text{pulse}}[\text{J}] = \frac{\epsilon_\gamma[\text{eV}]}{qHZ[\Omega]} \int_{-\infty}^{\infty} V[\text{V}]dt[\text{s}], \tag{181}$$

where Z is the detector's impedance, H is the attenuation factor of the filter and q is the quantum efficiency of the absorbing material. For the diode used, the impedance $Z = 50\ \Omega$, and the gold had a quantum efficiency $q_{\text{Au}} = 0.054$.

Hole diameter	10 μm
Hole density	10^5 cm^{-2}
Transmission fraction	7.85%

Table 7: Parameters of the gold-coated mesh used in front of the photodiode to attenuate the EUV laser beam.

We have used the Talbot effect in the design of a filter for the photodiode. Unfiltered, the laser energy is too high to be measured accurately, as a space charge is created in front of the detector by a large flux of photo-electrons. The detector

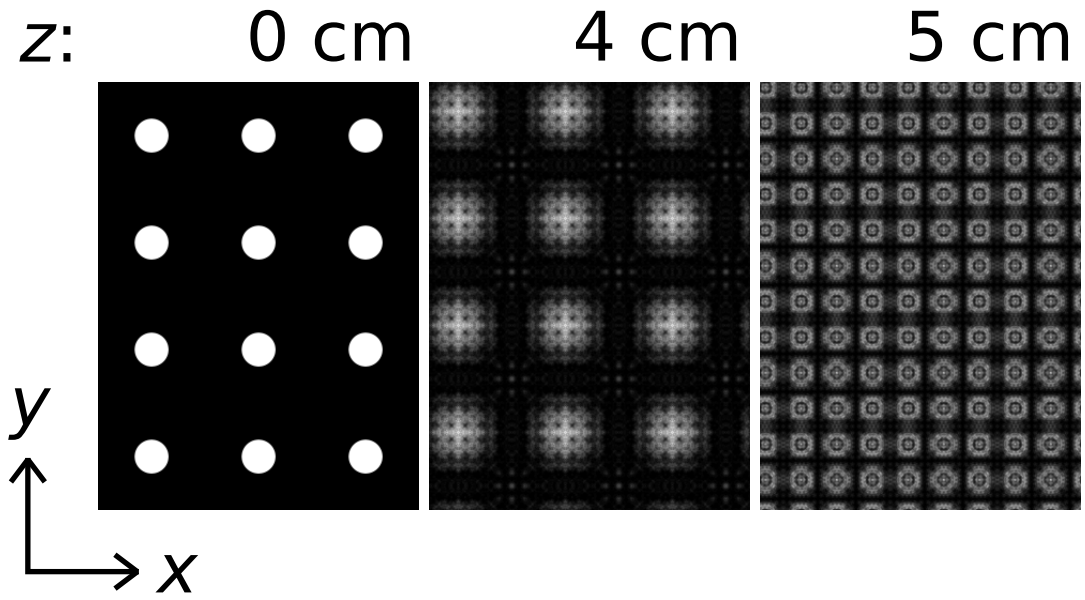

Figure 45: Talbot pattern for laser light with a wavelength of 46.9 nm, with a filter of regularly spaced circular holes of 10 μm diameter at distances z as indicated.

is required to yield a standalone measurement of the absolute pulse energy, so an unperforated aluminium filter (with a uniform, but finite attenuation) cannot be used to attenuate the beam. The uncertainty in the aluminium and oxidation layer thickness would introduce a high uncertainty into the filter transmission. An array of circular holes in a mesh, coated with gold (which almost infinitely attenuates the laser light) with properties listed in Table 7 was used instead.

We require that the resultant diffraction pattern from the mesh is sufficiently diffuse that a space charge does not form around the detector. Placing the mesh directly next to the photodiode could create undesirable alternating regions of high and low intensity. In this case, therefore, forming a Talbot pattern would also be undesirable. As discussed in §2.3, small perturbations to an initial Talbot mask tend to decay away, so large departures from an idealised regular grid are required to avoid a Talbot pattern repetition. We can therefore take a Talbot pattern to be the worst-case scenario in terms of having alternating regions of high and low intensity beam.

When the circular holes are arrayed regularly, we can calculate the resultant Talbot pattern in order to optimise the distance at which to place the mesh, so that the local intensity at the diode is not too great. The initial mesh and Talbot patterns at two distances, 4 and 5 cm, are shown in Figure 45. The grounded gold mesh needs to be positioned away from the diode in order to prevent a short circuit between the two, while also fitting within the constrained dimensions of the apparatus. A

position at a distance of 4 cm was chosen for the diode. We see from Figure 45 that the resulting pattern is significantly more uniform than the original mesh, therefore minimising the unwanted space charge build-up at the diode.

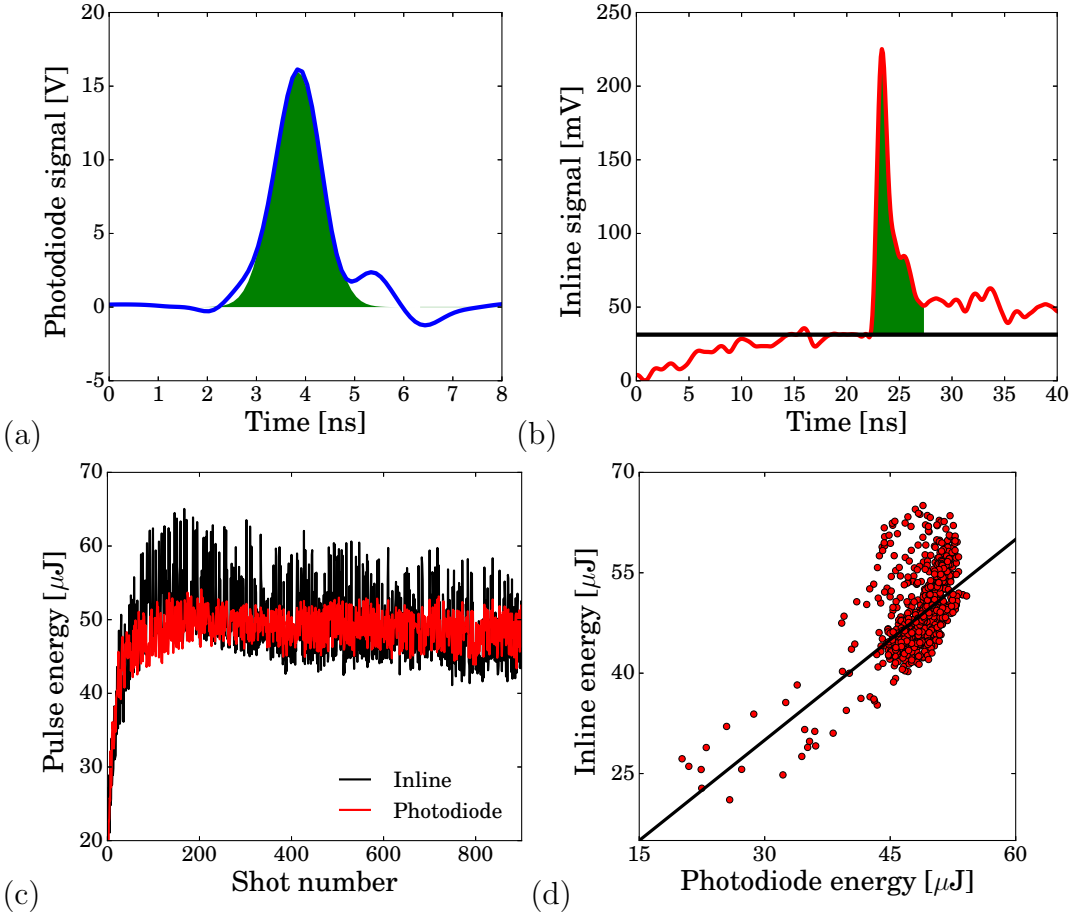

Figure 46: (a) Typical voltage signal from the photodiode (solid line), with a Gaussian fit used to integrate it (shaded region). (b) Magnitude of the voltage signal from the inline ionization detector for the same shot (solid line) with a noise floor as indicated and trapezoidal integration of the shaded region. (c) Pulse energies measured by both detectors as indicated for a number of shots at 1 Hz. (d) Each detector's energies plotted against each other (points) and the fit line (solid).

The voltage signals for both detectors were measured and digitised by Pico Technology oscilloscope. The photodiode signal is easy to isolate from any background and a Gaussian function can be readily fit to the digitised datapoints; an example is shown in Figure 46a, with fit parameters $A = 16.8$ V and $t_{1/2} = 1.12$ ns. The voltage signal can then be integrated analytically through Equation (186). We see from this example that the main signal is followed by an oscillation, which has been confirmed to originate from an imperfect electrical termination causing reflections and is ignored by the fit routine.

The inline detector produces a more complicated signal with a noise background for the duration of the capillary laser's cycle, most likely due to spontaneous emission. After subtracting this noise floor, it is difficult to describe the result with an analytic function; instead, it may be integrated trapezoidally. An example of the voltage signal, together with the noise floor and region of integration, is shown in Figure 46b.

In order to calibrate the integrated voltage signal from the inline detector with the photodiode energy calculated using Equation (181), a statistically significant number of laser shots must be compared to accurately determine the constant of proportionality. We have analysed three sets of 1000 shots (the digitization limit for a single run of the oscilloscope) to determine this conversion factor. Results from both detectors for one such set, where the energy ramped up as the laser began operation, are shown in Figure 46c. The shot-to-shot variation is typical of the capillary discharge laser. The statistical fit is evaluated by comparing both detectors' energy values as in Figure 46d. We see that the points lie within 5 μJ of the fit line (which is taken as the error margin of the measurements), with the exception of a number of high energy pulses, where the energy is overestimated by the inline detector.

As a result of the studies of these methods of pulse energy measurement, we discovered that the laser's pulse energy is maximised for continuous operation with repetition rates of 1 Hz - the lowest possible repetition rate at the time of the experiments. However, this maximum was reached only after a ramp-up of 20 or more continuous shots, as can be seen in Figure 46c. In order to conduct the planned experiment with a single intense pulse delivered to a target, these initial shots must be diverted away. To achieve this, we installed a rudimentary shutter which was a movable optical mirror (opaque to EUV radiation) with the appropriate vacuum feed-through controls. Although it was only manually operable, it was possible to time it to open for the last shot in a given sequence. It is preferrable to integrate a similar movable beam blocker into the control electronics of future experiments.

5.2.4 Alignment and focal spot characterisation

In order to align the optical components and targets with the invisible EUV beam, we have retraced their path using a low-power helium-neon (HeNe) alignment laser. Initially counter-propagating in the plane of the capillary, the HeNe is inserted into the beamline using two adjustable mirrors. We ensure co-alignment of the beams by manipulating the mirrors to fix the visible beam to two photoresist samples (one

for each mirror) previously exposed to the EUV beam. The sample closer to the laser is removed to allow access to the other and replaced into its position with an accuracy of 1 mm, leading to an angular accuracy of ~ 1 mrad.

To form the photoresists, microscope glass slides were cut to size to fit into holders and coated with a layer of the plastic PMMA (polymethyl methacrylate). After removal from the vacuum chamber, EUV exposed slides can be developed for post-shot analysis by applying a 1:3 solution of MIBK (methyl isobutyl ketone) and IPA (isopropyl alcohol) respectively with pressurized nitrogen gas used to remove excess fluid.

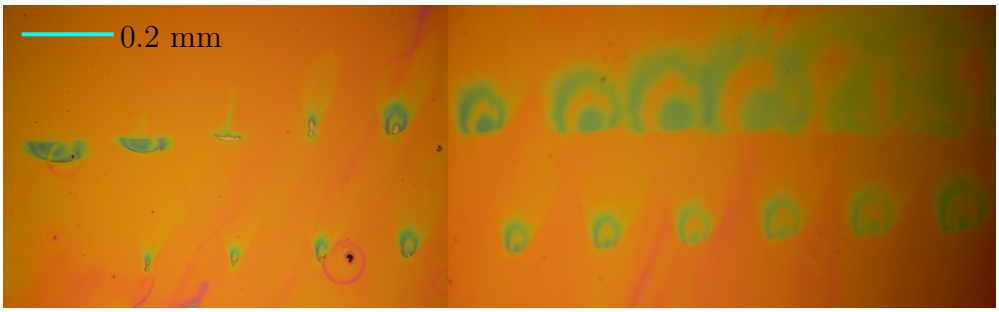

Figure 47: Developed PMMA slide showing beam profiles spaced in the z-direction (perpendicular to the plane of the slide) by 0.5 mm (top) and 0.2 mm (bottom).

When focusing the laser beam, the PMMA slides may be used to image the size and shape of the beam at the desired focal plane with the aid of an optical microscope. The regions of highest intensity, where material has been ablated, are visible without development. We have found that 20× microscope magnification is sufficient for this purpose. Imaging the focal spot is necessary to confirm its position, as although the HeNe beam can propagate coaxially with the EUV beam, it has a different beam shape (as discussed below) and different interaction with the optics, for example a different phase change due to the MLMs.

An approximate scan (in steps of 0.5 and 0.2 mm respectively) along the beam axis, around the planned target position, used to locate the optimal focal spot is shown in Figure 47. The beam was clipped on one side, which allowed straightforward identification of the focal spot using the observation that the beam shape inverts about the focal position. We see that the beam shapes are generally self-similar outside the focal region, but become difficult to predict near focus without detailed modelling.

Fine scans of beam shapes close to the focus provide an opportunity to benchmark the code `SAFE2DIP`, by comparisons with its output. We performed a scan

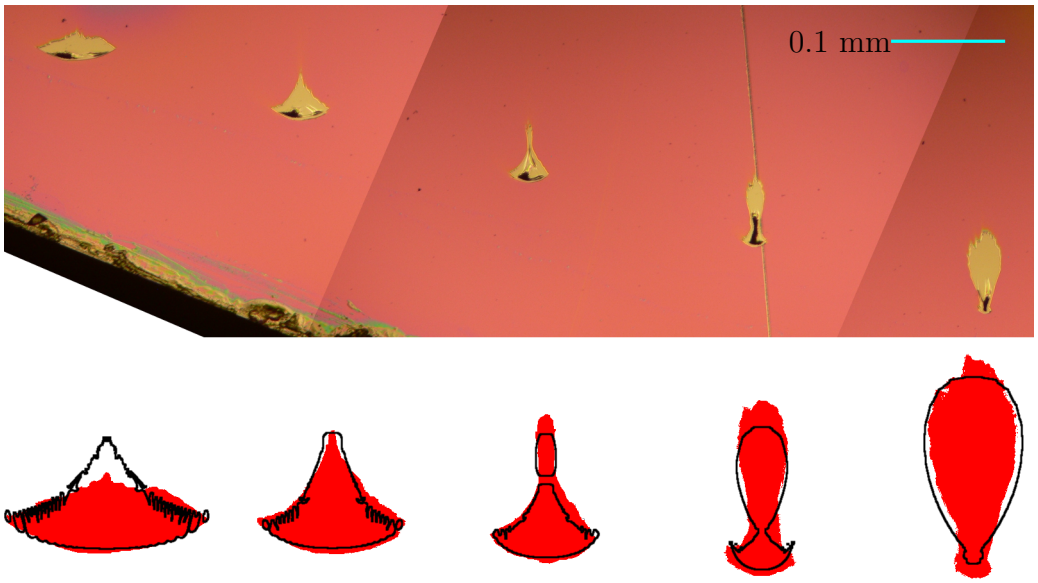

Figure 48: (Top) Microscope image of ablation profiles of parylene-N coated onto glass slides spaced in the z-dimension by 0.1 mm. The blackened regions correspond to ablation of the glass substrate. (Bottom) The ablation profiles (red) with an intensity contour (black) calculated by `SAFE2DIP`.

over z in the focal region in steps of 0.1 mm, ablating the surface of microscope glass slides coated with parylene-N. Images of the slides taken at 20× magnification are shown in Figure 48; three images are "stitched together" to reproduce the entire region. The pink colour of the parylene-N film allows it to be easily distinguished from the glass substrate, in areas where the intensity was sufficient to cause ablation. In areas of very high fluence the glass substrate for the photoresist has been ablated, leaving regions which appear black under microscope illumination. The regions of glass have been digitally extracted from the micrographs and are shown enlarged in red in Figure 48. Contours of a constant intensity taken from `SAFE2DIP` simulations spaced by 0.1 mm are also pictured. There is a generally good agreement between the simulations and the micrographs. The details of `SAFE2DIP` calculations are discussed in more detail in the next section.

5.3 Multilayer mirror focus results and analysis

We have performed experiments to ablate thin targets and captured the transmitted beam using the CCD. These images were collated together with the corresponding pulse energy and high magnification micrographs of the ablation regions. These are shown in Figure 49.

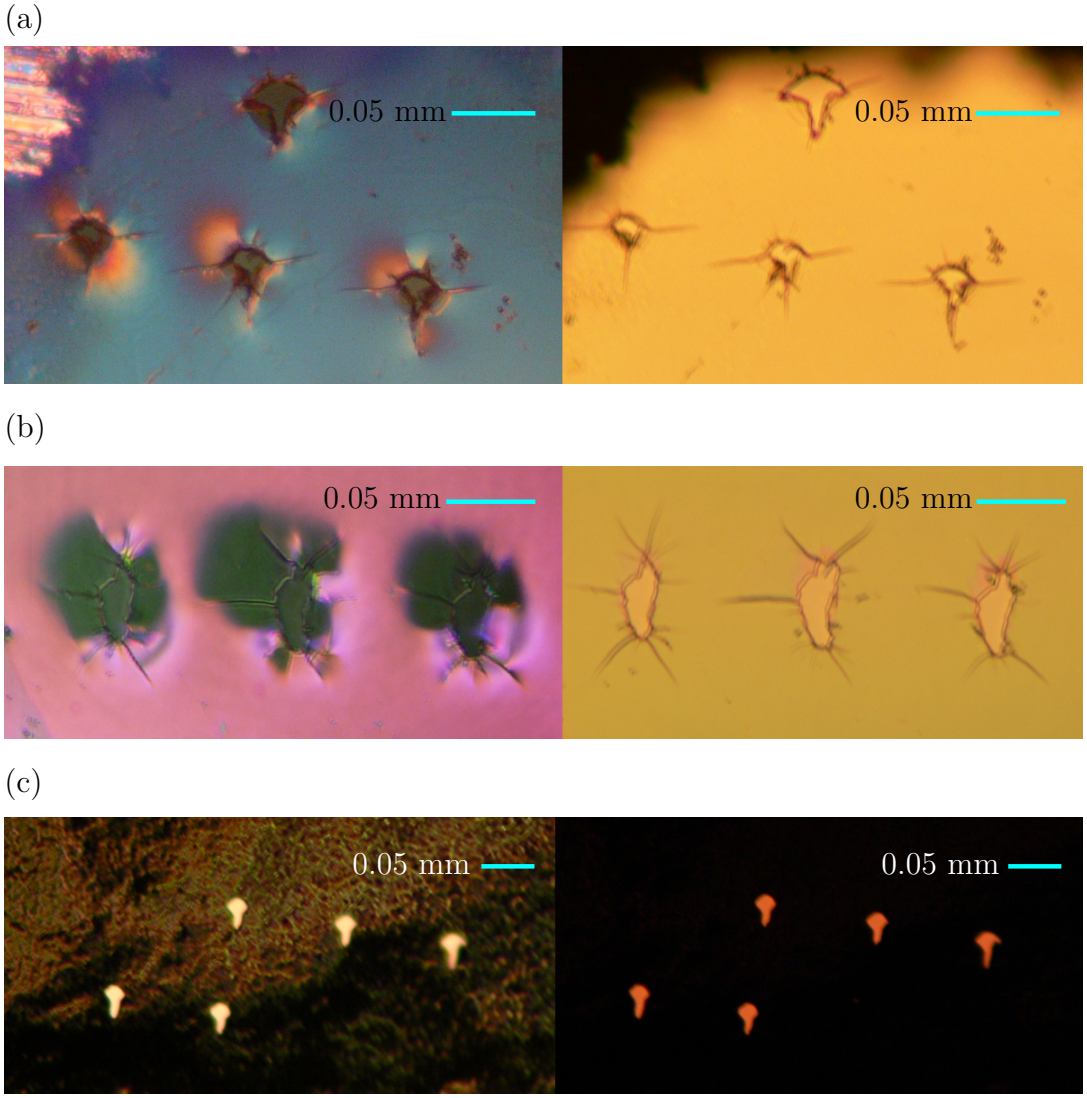

Figure 49: Reflection (left) and transmission (right) micrographs of parylene-N targets of thickness (a) 1028 nm, (b) 429 nm and (c) aluminium of thickness 1200 nm.

5.3.1 Simulations of the focal spots

To match the ablation profiles seen in the micrographs, simulations were performed with `SAFE2DIP`. The EUV laser beam was modelled by an offset Gaussian profile, as outlined in §5.2.2. It was treated as a spherical wave expanding from a point at the end of the capillary. The phase profile is spherical with a radius of curvature equal to the distance from the capillary and the widths w and r_0 scaled appropriately.

The beam's amplitude and phase are modified by a multilayer mirror, as given by Equation (43). The angular dependence of the reflection amplitude $\mathtt{r}$ (whose modulus squared gives the total reflectance) and extra phase has been computed by the `IMD` code[56] for the Sc/Si mirror parameters in Table 6. In order to accelerate

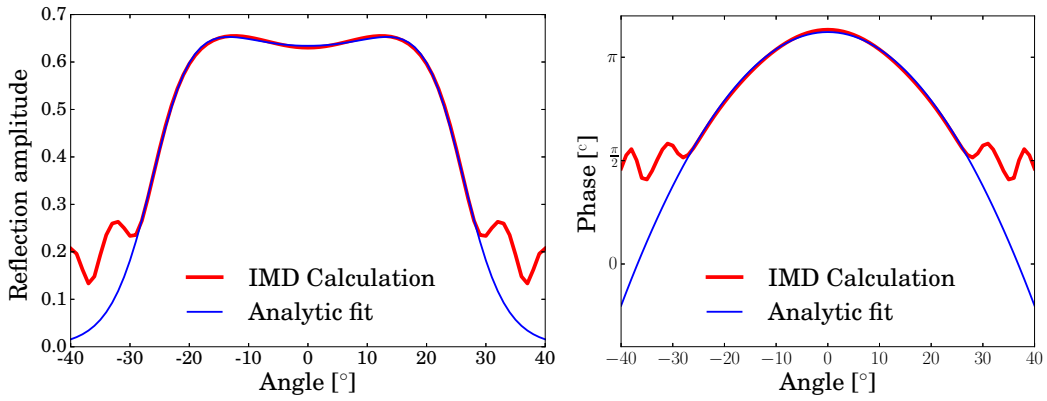

Figure 50: Reflection amplitude and phase as a function of the incidence angle onto the Sc/Si mirrors, as calculated by the `IMD` code and analytic fits.

calculations, it is useful to fit these quantities by analytic functions. This leads to a parameterisation of the form

$$\phi_{MLM} = A_\phi \eta^2, \tag{182}$$

$$\mathtt{r} = A_\mathtt{r}(1 + D\eta^2)\{1 - \tanh[C(|\eta| - B)]\}, \tag{183}$$

where η is the angle of incidence onto the mirror and A_ϕ, $A_\mathtt{r}$, B, C, D are the fit parameters. These functions and the `IMD` simulations are shown in Figure 50. We see a good agreement between the simulation and fit up to approximately 25°, which is a sufficient range for the mirrors in this experiment. It is noteworthy that the additional phase is largely quadratic, similar to the phase added by the mirror curvature itself. This effect shifts the position of the focal spot.

The measured beam profile of Equations (179) and (180), together with the MLM properties, allows a parameter scan of the focal profile along the beam axis. Measured values of the mirror tilt angle $\alpha = 4.7°$ (the beam is then reflected at an angle 2α) and target tilt angle $\beta = 9.4°$ were used in the `SAFE2DIP` geometry, which is shown in Figure 7. The Fresnel diffraction integral is normalised via Equation (22), using the beam energy values obtained from the inline detector. Two examples of focal profiles are shown in Figure 51.

We are able to match the results of `SAFE2DIP` simulations to ablated profiles by considering contours of constant intensity. We have made such comparisons with ablation of parylene-N from glass slides in §5.2.4, but thin targets provide an unambiguous point of comparison through the contrast of the holes made in the target material. Contours are overlaid onto micrographs of 1028 nm thick parylene-N after 30 shots on target and 1200 nm thick aluminium after two shots on target in

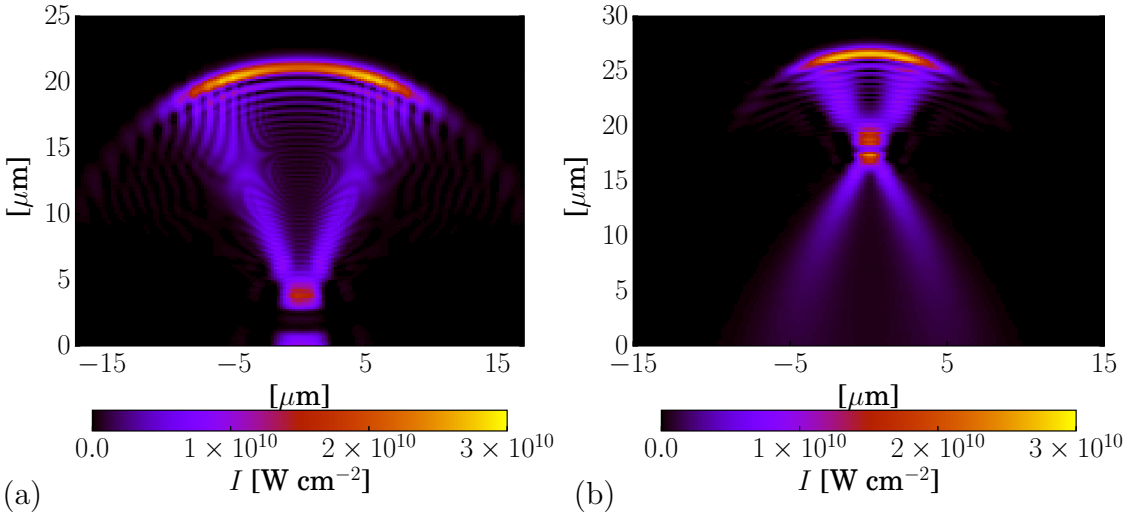

Figure 51: The results of `SAFE2DIP` simulations of the focal spot profile of the off-axis MLM, with $\alpha = 4.7°$ at (a) $z = 49.75$ mm and (b) $z = 49.85$ mm. The profiles have been normalised to an intensity corresponding to an average pulse energy of 32 μJ, as measured by the inline detector.

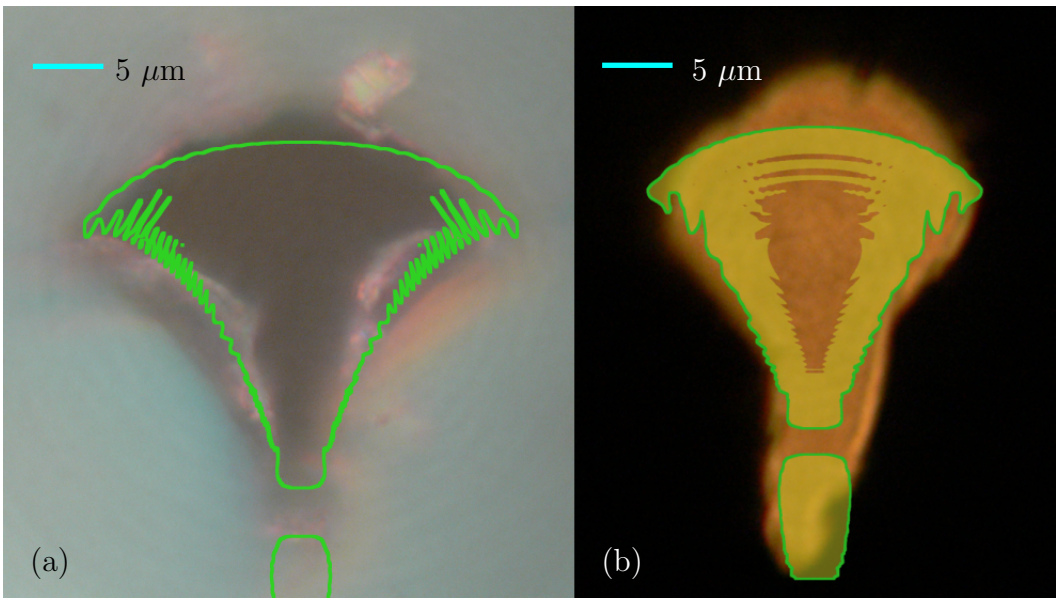

Figure 52: Intensity contours taken from `SAFE2DIP` simulations overlaid on micrographs with 100× magnification of (a) 1028 nm parylene-N and (b) 1200 nm aluminium.

Figure 52; the region with intensity above the contour threshold is filled in the latter case, showing that the profile is hollow. We see good overall agreement between the simulations and experimental results, particularly since the large number of shots

in the given examples smooth out any unexpected asymmetries in the laser profile.

5.3.2 Hydrodynamic simulations

We are unable to use an azimuthally symmetric code like POLLUX to directly model the fundamentally 2-dimensional focal intensity profiles and therefore 3-dimensional plasmas produced by the tilted MLMs. A fully 3-dimensional radiation-hydrodynamic code is currently under development at the University of York.[106] However, POLLUX simulations can be used to attain a reasonable approximation to the ablated profiles, because 3-dimensional effects like lateral heat conduction are not significant at the target surface. This implies that target ablation is strongly dependent only on the local intensity.

We therefore use the simplifying assumption that if we simulate a plasma in 2 dimensions (for example in x and z), the result is independent of the variation in the other lateral dimension (in this case, y). Schematically, we assume that plasma properties along a line (red) through a circular intensity profile ϕ are similar to those along a line through a linear intensity profile ⊣⊢.

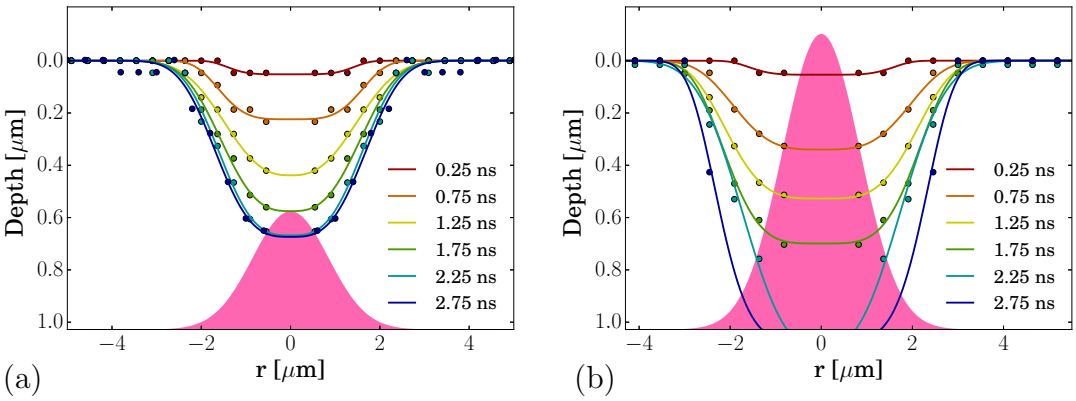

Figure 53: Time-resolved target depth on the POLLUX grid (points) parameterised by super-Gaussian curves (lines). A depth of 1028 nm corresponds to ablation through the entire target. The targets are 1028 nm thick parylene-N with incident laser radiation with a peak intensity of (a) 10^{10} W cm^{-2} and (b) 2.5×10^{10} W cm^{-2} and FWHM of 2 μm, as shown schematically by the shaded region.

We obtain a time-resolved target depth from POLLUX simulations by tracking the outermost (in the cylindrical dimension z) grid points with solid density. At the final simulation time, this depth corresponds to the measurable ablation profile after the experiment. The depth at these discrete points can be parameterised by a super-Gaussian function $\mathcal{G}_n$ (discussed in Appendix B), allowing interpolation to a

finer grid. This may be necessary, because many grid points are required to simulate the plasma plume created by laser interactions (which can be seen, for example, in Figure 41), leading to a relatively low resolution at the focus of the laser. Examples of such time-resolved depth profiles, starting with uniformly thick 1028 nm parylene-N, are shown for two intensities in Figure 53. We see that the more intense pulse is able to directly penetrate the parylene-N target, while two shots would be required for the less intense pulse.

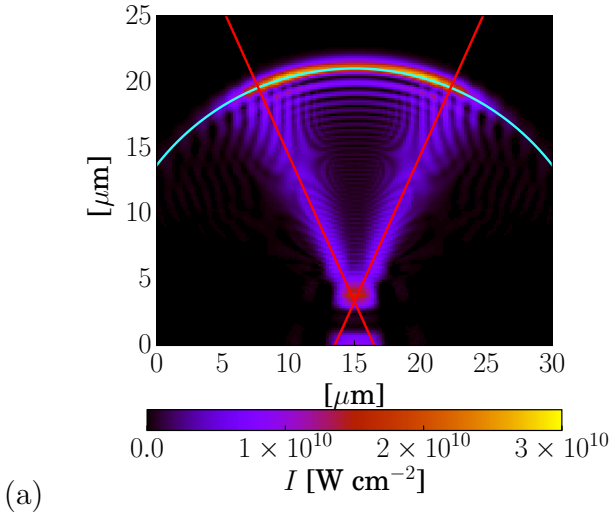

(a)

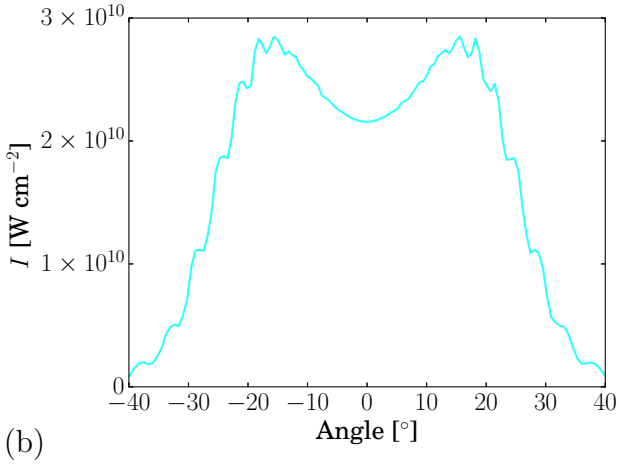

(b)

Figure 54: (a) `SAFE2DIP` simulation with $\alpha = 4.7°$ at $z = 49.75$ mm with a circle over the "arc" (light blue) and symmetric straight lines over the V-shape (red). (b) Intensity as a function of angle over the circle.

The `SAFE2DIP` intensity profiles can be decomposed into several geometric components, as shown in Figure 54. The profile is composed of a prominent circular "arc" feature, which contains the highest intensity of the entire profile at 2.8×10^{10} W cm^{-2} and has a FWHM of 2 μm. We take a line out from the arc along a circle

with a radius of 19 μm. The rest of the profile forms a V-shape, with a varying FWHM and an approximately constant intensity of 5×10^9 W cm^{-2}. We take a line out along a straight line (the profile is symmetric about its centre) to form the V-shape. The present approach is described for an arbitrary curve in Appendix E.

With the decompositions of the simulated intensity profile, we use the assumption that the lateral intensity variation has no effect on the laser-produced plasma to obtain a fully 3-dimensional target profile from the parameterised `POLLUX` simulations. We impose simulated depths along a line perpendicular to the points on the arc and the V-shape. The intensities at points on these lines allow the appropriate parameterised depth profile to be imposed perpendicularly outwards. The codes `SAFE2DIP` and `POLLUX` give results at discrete points in their parameter space - intensity on specific grid points or depth profiles with a certain peak intensity; interpolation yields values between these discrete points. A depth profile calculated by this method for a single shot incident on 1028 nm parylene-N is shown in Figure 55a.

Such a target depth profile is calculated for all the relevant focal intensity profiles, target thicknesses and materials. To allow a direct comparison to the micrographs, we take a contour corresponding to a depth of 1028 nm - the region predicted to have been penetrated by the laser. These contours are overlaid over micrographs with five different sets of conditions in Figure 55.

We see a generally good agreement between the micrographs and computed contours, but several experimental considerations must be taken into account. Due to the annular capillary discharge laser profile, above a certain MLM tilt angle, the focused intensity profiles form a closed loop of high intensity around a central minimum; this can be seen in `SAFE2DIP` calculations presented above. As a result, solid pieces of material ~ 5 μm across are cut from the targets, but remain intact. Such a piece, which has remained attached to the target after a single shot, is labelled by a green asterisk in Figure 55b. The targets have also been affected by venting the experimental chamber back to atmospheric pressure, which creates cracks in regions embrittled by the laser. The targets have been prepared under tension; its release by laser interactions, in addition to embrittlement, has caused cracks as seen in Figure 55e.

5.3.3 Transmission analysis

The second multilayer mirror M2 recollimated the transmitted laser radiation, allowing it to be imaged by the CCD after attenuation by a filter. This optical

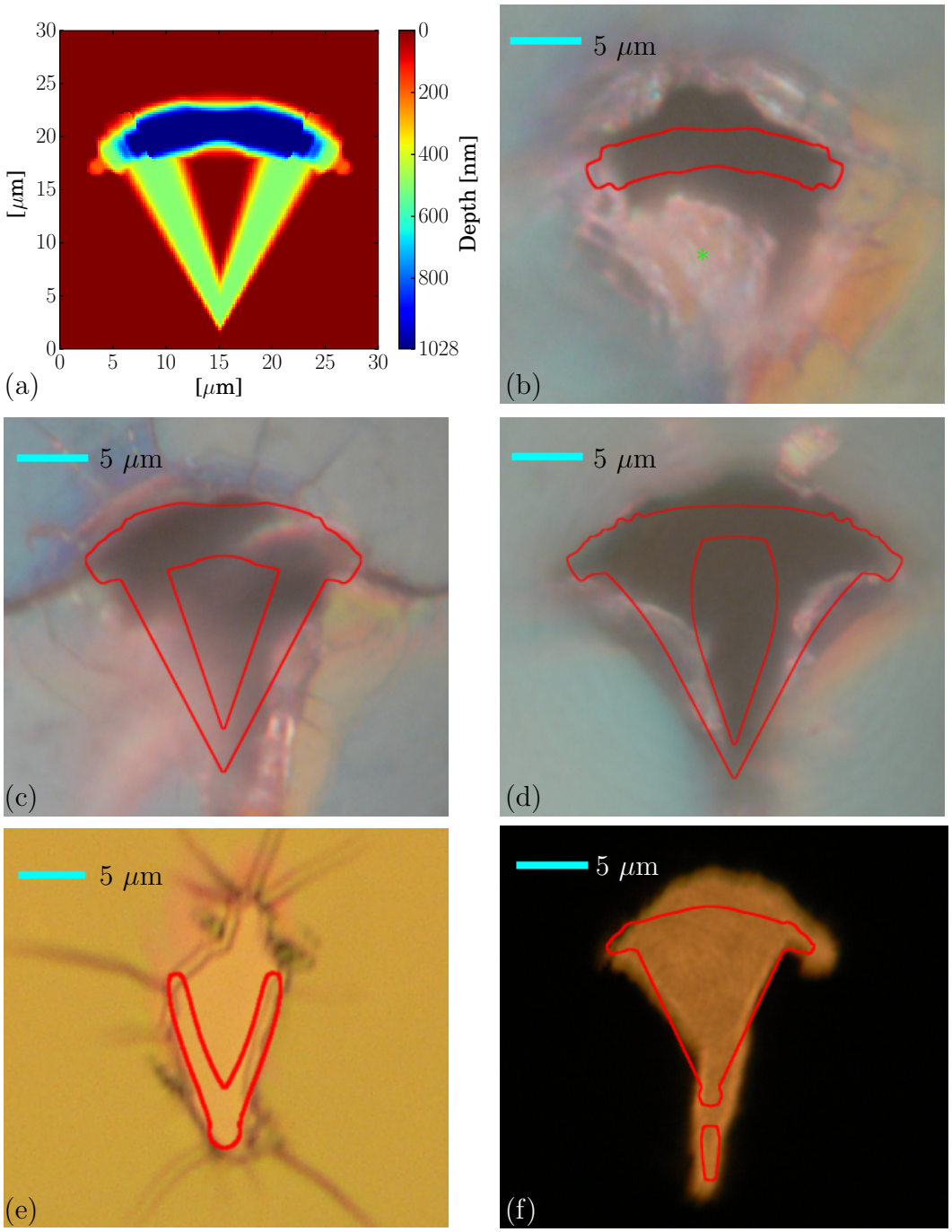

Figure 55: (a) Simulated depth profile of a single laser shot on a 1028 nm parylene-N target. Micrographs of targets of this thickness overlaid with contours corresponding to where the target has been penetrated (corresponding to a depth of 0 nm) by (b) single shot, (c) two shots and (d) 30 shots. Contours over (e) 429 nm parylene-N target after a single shot and (f) 1.2 μm aluminium target after two shots. A region of unablated target material in (b), which has folded inwards, is denoted by the green asterisk. The distance z from the MLM to the targets differed by up to 30 μm in these cases, leading to different incident intensity profiles.

arrangement led to strong distortion of the annular laser profile, even in the absence of any targets, but nonetheless provided an additional diagnostic for EUV laser ablation experiments. The two mirrors produced a small de-magnification, because they were not separated by precisely $2f$ and because of a small mismatch in the focal lengths, despite having identical radii of curvature to within manufacturing tolerances. An image of the laser beam after passing through the optical system in the absence of a target is shown in Figure 56a. Despite the strong distortion, a line out of the intensity profile, as given in Figure 56b, closely matches the annular profile measured previously after scaling the linear dimension to account for the de-magnification.

The laser intensities captured during single-shot ablation of the targets are largely consistent with diffraction calculations and allow some insight into the plasma interactions. CCD images of the transmitted laser beam through the 429 and 1028 nm parylene-N targets are shown in Figures 56c and 56e respectively. Contrast in the latter has been greatly increased, to compensate for the small transmitted energy fraction. Transmitted intensity profiles have been obtained by calculating diffraction through the areas where the targets have been penetrated in §5.3.2. In effect, the aperture is treated as a spatial filter to the incident intensity profile. The resultant diffracted intensities are given in Figures 56d and 56f respectively. The de-magnification factor obtained from scaling in Figure 55b was used to ultimately scale the linear dimensions in these simulations.

The CCD images may be used to obtain a value for the total fraction of the energy of a single pulse transmitted after interactions with a target. We have taken a sum of the detector counts over the beam shape in CCD images taken with and without interaction with a target. The ratio of these two cases gives the transmitted energy fraction, when weighted by the individual pulse energies taken from the inline detector. These ratios are given for three experimental conditions in Table 8.

Target conditions	**Transmission fraction**
429 nm parylene-N, 0 shots	1.5±0.35%
429 nm parylene-N, 1 shot	∼ 100%
1028 nm parylene-N, 0 shots	0.31±0.065%
1028 nm parylene-N, 1 shot	33.4±6.6%

Table 8: The fraction of laser light transmitted through a range of targets as measured by the CCD.

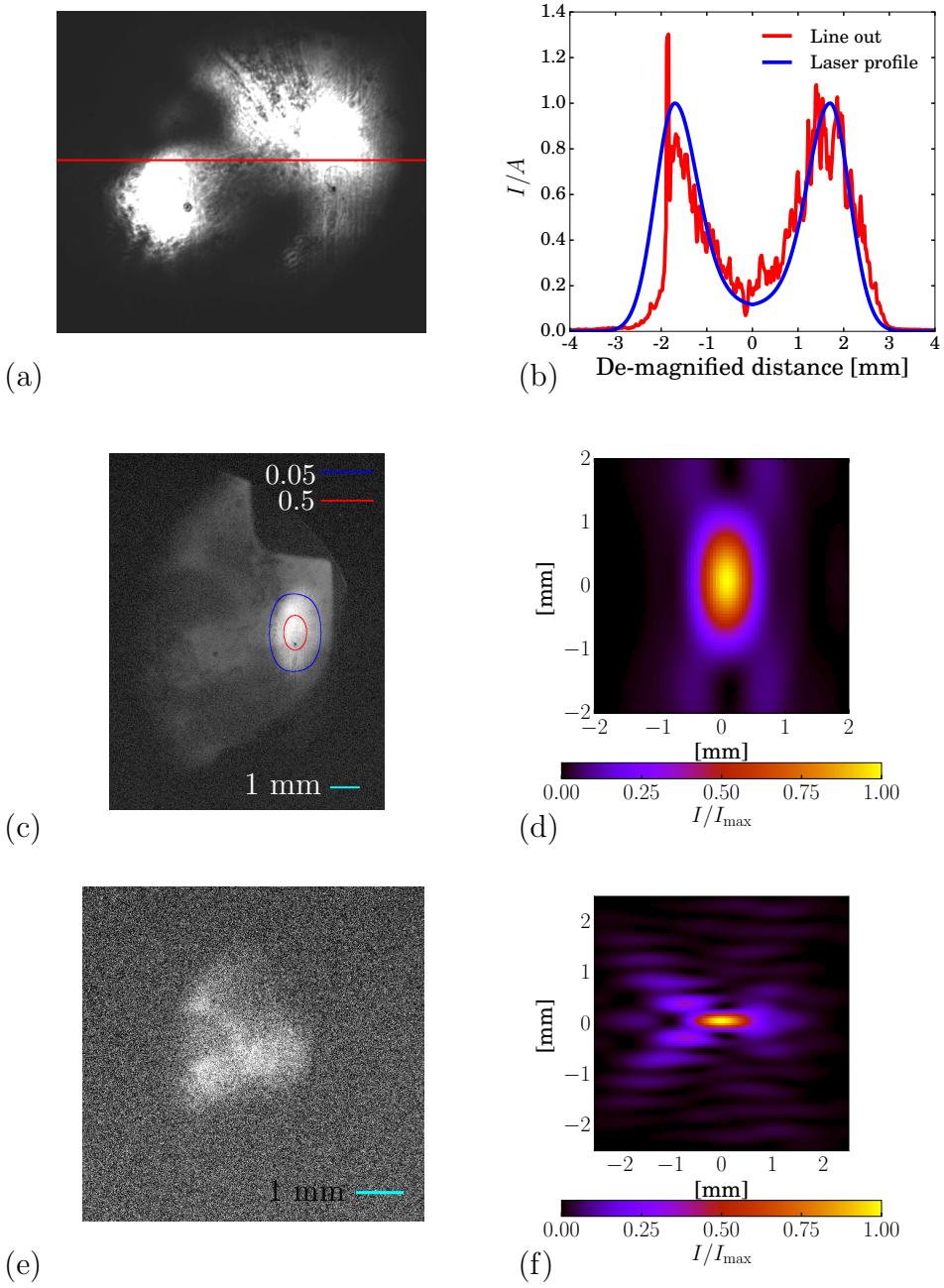

Figure 56: (a) Background subtracted image of the EUV laser beam after passing through the MLM optical setup, as shown in Figure 43. (b) Intensity profile along the red line, compared to the fit of Equations (179) and (180), with appropriate scaling due to de-magnification in the optical setup and normalised to the A parameter in the fit equations. (c) Single-shot transmission through a 429 nm parylene-N target (ablation profile shown in Figure 55e) with contours from (d) the simulated transmitted intensity. (e) High-contrast image of transmission through a 1028 nm parylene-N target (ablation profile shown in Figure 55b) and (f) the simulated intensity.

At present, the hydrodynamic simulations have insufficient spatial resolution to provide the optical depths and phase modulation required to achieve full agreement between measurments and simulations of transmission in the experiments discussed. The results in this section show modest qualitative agreement and motivate further experiments. Previous studies have used coherent EUV radiation to diagnose plasmas created by intense, short-pulse optical lasers.[119] The present work opens the possibility to create and diagnose a plasma using a single EUV pulse. The plasma generated in this way may be significantly more dense because of the higher critical density of EUV photons. A long optical laser pulse may instead be used as a backlighter to image the low-density expanding plasma plume after the main EUV pulse.

6 Conclusions

This work has explored the methods of focusing lasers with wavelengths in the extreme ultraviolet (EUV) range, and the plasmas produced at such a focal spot. The effects of wave optics - diffraction and inteference - have been used to achieve focused intensities of $\leq 3 \times 10^{10}$ W cm^{-2} and simulated by the code `SAFE2DIP`, written as part of this work. Plasmas produced by these and higher intensities have been simulated on the microscopic scale using the collisional-radiative code `CRABS`, written as part of this work, and on the macroscopic scale by the radiation-hydrodynamic code `POLLUX`, written previously at the University of York. Experiments have been undertaken with a novel capillary discharge laser to validate these codes and to develop techniques for future experiments.

We have shown that solid-density plasmas produced by EUV lasers remain close to local thermodynamic equilibrium (LTE). LTE holds exactly if the collisions between electrons and ions are solely responsible for the change in the excitation and ionization state of the ions. Due to the high densities, the collisional rates do indeed dominate over radiative rates for low to moderate incident intensities of radiation ($0 < I < 10^{12}$ W cm^{-2}). A criterion has been derived to determine if photoionization has an effect on LTE in similar fashion to that of McWhirter, which determines if the density is sufficient for LTE to hold.

We have studied the effect of rapid heating on a plasma, by considering a rapid increase in the electrons' kinetic energy over 10 or 100 fs. This is taken as an extreme case, with heating typically occurring on much longer timescales. The collisional rates are sufficiently high that LTE is reached in a time < 1 ps after such transient heating for plasma densities as low as 10% of solid. Such timescales are well below the timescales of interest for hydrodynamic expansion occuring when EUV lasers interact with solid-density targets.

The statistics of electrons at high density must be modelled by the Fermi-Dirac distribution, because many of the available quantum states have been occupied. The rates of electron collisions with ions are reduced, as such collisions can occur only if free quantum states exist for the outgoing electrons. Accounting for the outgoing electrons requires detailed data for the collisional ionization differential cross section, which is relatively poorly studied. We have found that even for solid-density plasmas, these quantum degeneracy effects are insignificant if the incident flux of ionizing radiation is relatively small. In that case, the electron density and temperature are simultaneously low and *vice versa*, while LTE holds. However, the

Fermi-Dirac distribution deviates from the Maxwell-Boltzmann distribution only when the electrons are both cold and dense. This is the case when the plasma is driven out of LTE by a high intensity ($> 10^{13}$ W cm^{-2}) of photoionizing radiation. In practice, such a flux of radiation would rapidly heat the plasma to high temperatures where the electrons behave classically. The difference in the atomic rates and heat capacity between the two cases may nonetheless lead to differences in the final properties of the plasma.

The results of the collisional-radiative modelling are fortuitous, because the state of a plasma in LTE is determined by the relatively straightforward Saha-Boltzmann equation. LTE eliminates the need to calculate computationally expensive atomic processes, whose rates depend on experimentally determined cross sections. It allows the equation of state of plasmas to be calculated inline by hydrodynamic codes like `POLLUX`.

If a plasma is generated at low density, for example from a gas, it may exhibit interesting non-LTE properties. This is the principle behind the capillary discharge laser operating in an argon plasma created by a strong electrical discharge, which has been used for experiments described here. Laser gain can only be achieved if the medium is fundamentally out of thermodynamic equilibrium, which is achieved by the electrical discharge in this case. We have explored how a laser focused onto a gas target may lead to a drop in opacity, allowing the laser to propagate further. This cycle of opacity "bleaching" propagates at a well-defined rate, which can be estimated by simple energy considerations. The phenomenon of opacity bleaching may be observed by the change in the intensity profile of the transmitted laser beam, due to diffraction. At higher densities, strong inverse bremsstrahlung absorption prevents a bleaching wave from propagating.

The wave description of light is very important to the design of optics for laser wavelengths below the visible. Low reflectivities and high absorption by many solid state materials in the EUV spectral region makes it challenging to conduct experiments. Significant net reflectivity is possible only from a stack of wavelength-sized dielectric layers, with net reflectivities of $\leq 60\%$.

Experiments have been undertaken on a new version of capillary discharge laser with a wavelength of 46.9 nm. This laser's pulse shapes and energies were measured as part of this work. Two types of focusing geometry have been exploited in these experiments: a Fresnel zone plate (FZP) and multilayer mirror (MLM). The FZP has the advantages of a very tight focal spot and its inherent angular symmetry. However, it is greatly limited in size, as the zone widths become ever smaller. Only

a small fraction of the laser beam is then available to be focused, and the FZP requires half of the incident flux (negative zones) to be filtered. Furthermore, the tight focus comes at the cost of an extremely short focal length - for example, the FZP used for experiments had $f = 2.1$ mm. Practically, targets must be located within several micrometres of the focal position, but without specialist positioning and fiducial equipment, it is difficult to position a target to an accuracy better than 0.1 mm.

MLMs can be manufactured to capture an entire laser beam with ease and have advantageously long focal lengths. However, the setup with a single MLM tilted with respect to the beam axis, has led to asymmetric and spatially extended focal profiles. Nonetheless, peak intensities were achieved exceeding those of the FZP setup. We have seen good agreement between `SAFE2DIP` simulations and ablation profiles created in experiments. To avoid such asymmetries, MLMs must be used in a pair-wise arrangement such as the Schwarzschild or Kirkpatrick-Baez, leading to a tight focus with angular symmetry, but at the expense of an extra reflective loss and a great increase in the complexity of the setup.

The radiation-hydrodynamic code `POLLUX` has been used to simulate the ablation of material and motion of plasmas created by the capillary discharge laser. `POLLUX` simulations are able to successfully predict the depth of ablation in solid density material, if the incident laser radiation has full angular symmetry. This work presents approaches to model asymmetric intensity profiles using `POLLUX` by deomposing them into simple geometric components. This approach is valid because lateral heat transport is not significant in this regime of laser interactions. Good agreement is found between ablation profiles calculated by this approach and a wide range of experimental parameters.

We have demonstrated the feasibility of both creating and imaging a dense plasma with a single EUV laser beam transmitted through a thin target. Complete analysis of the transmission requires accurate hydrodynamic models, but may serve as an important diagnostic in future experiments. The high spatial and temporal coherence of EUV lasers opens the possibility to perform interferometry. Their high photon energies allow the poorly understood regime of high density plasmas to be studied.

Future work

- Further experiments are planned to be undertaken using capillary discharge lasers operating at 46.9 nm. A Schwarzschild objective may be constructed in order to make use of the large total energy throughput of reflective optics, while minimizing the focal spot size. The theoretical framework developed in this work may be extended to simulate the intensity at the focus by solving appropriate Fresnel integrals. Multilayer effects may be calculated by the `IMD` code, which has been further verified for 46.9 nm photons as part of this work; the effect of radial asymmetries, such as from the mirror supports, can be simulated by a code like `SAFE2DIP`.

- An increase in peak intensity would allow a wider range of target thickness and material to be investigated, in order to further verify `POLLUX` across differing plasma conditions. In addition to solid targets, chosen for this work in part because of their simplicity, an EUV laser may be focused onto a gas jet. The density profile of such a jet would need to be characterised and used in simulations in order to explain the results of such experiments. Further diagnostics for the plasma parameters, such as visible or soft x-ray spectrometers, may be added to the setup.

- The effects of electron degeneracy in collisional-radiative models may be explored further. The increased computational cost of the related numerical integrals may be offset by further parallelism. Newly emerging computing architectures, such as Graphics Processing Units (GPUs), are based on a large number of multi-threaded processors, each of which can evaluate an individual rate coefficient simultaneously. Simulations requiring many rate evaluations may then be performed with an efficient code on a high performance cluster in a reasonable time.

Appendices

A Conventions

This section discusses the units and notation used throughout this text, which are frequently used in plasma physics.

A.1 Units

It is convenient when describing plasmas to use electronvolts (eV), centimetres (cm) and seconds (s), instead of the usual seven SI base units. Electronvolts are particularly useful when considering plasmas, as the kinetic energies and ionization potentials of particles in plasmas are typically tens or hundreds of eV. The symbols used throughout this work and their units are shown in Table 9.

Quantity	**Symbol**	**Unit**
Length	l, x, δx...	cm
Time	t	s
Mass	m, m_e	eV/c^2
Energy	E, ϵ, ϵ_γ	eV
Temperature	T, T_e, T_r	eV
Density	N, n	cm^{-3}
Energy density	ε	eV cm^{-3}
Intensity	I	W cm^{-2}
Spectral Intensity	$I(\epsilon_\gamma)$	s^{-1} cm^{-2}
Partition function	$\mathcal{Z}$	–
Degeneracy	g	–
Coulomb logarithm	Ξ	–

Table 9: Unless stated otherwise, these symbols and units are used throughout the text.

Temperatures are implicitly multiplied by the Boltzmann constant k_B in order to express them in units of eV. Masses are given in units of eV/c^2, as they are frequently multiplied by the speed of light squared; this leads to convenient quantities for the masses of subatomic particles. One exception to this are intensities, which are given in the units of W cm^{-2} as are commonly used for laser physics. Intensities may be converted to units of eV s^{-1} cm^{-2} through division by the elementary charge

$e = 1.602176 \times 10^{-19}$ A s. Several pertinent combinations of elementary constants, which are frequently used in plasma physics, are given in Table 10.

Constant	**Value**	**Units**
$\hbar c = hc/2\pi$	1.97327×10^{-5}	eV cm
e^2/ε_0	1.80705×10^{-6}	eV cm
$m_e c^2$	5.10999×10^{5}	eV
$\mathrm{Ry} = m_e c^2 e^4/8(hc)^2\varepsilon_0^2$	1.36057×10^{1}	eV
$G = 4\pi(2m_e c^2/h^2c^2)^{3/2}$	6.81220×10^{21}	$\mathrm{eV}^{-3/2}$ cm^{-3}

Table 10: Numerical values of combinations of physical constants which occur frequently throughout this text.

As ions, electrons and radiation may frequently be out of thermodynamic equilibrium with one another, temperatures are frequently subscripted T_i, T_e and T_r respectively. We subscript quantities involving photons with the symbol γ. We distinguish between the absolute intensity of radiation I - a power per unit area - and the spectral intensity $I(\epsilon)$ - the power per unit area per photon energy. The two are related via the integral $I = \int_0^\infty I(\epsilon_\gamma) d\epsilon_\gamma$.

A.2 Atomic physics conventions

As a result of the high energy densities in plasmas, electrons in atoms may be excited to highly energetic quantum states and ionized many times. We use the words "atom" and "ion" interchangeably in this work; a neutral atom is considered to be an "ion" with zero charge. Each electron bound to an atom has an integer-valued principal quantum number n and an azimuthal quantum number l. To denote such an atom's configuration, each electron is labelled with the numerical value of n and a letter corresponding to l; for historical reasons, the first four values of l take the letters s, p, d, f and thereafter increase alphabetically. The principal quantum numbers may also be referred to in the literature as shells, labelled K, L, M *etc.*, while an azimuthal quantum number within a shell is termed a subshell. Electrons have a further spin quantum number $m = \pm 1$, usually not labelled. Each quantum state may only be occupied by a single electron due to the Pauli exclusion principle. An example of a typical electron configuration of neon is $1s^2\ 2s^2\ 2p^5\ 3p$, where there are two 1s electrons *etc.*; we see that the outermost electron has been excited from the ground state and we may refer to this configuration as 3p in shorthand. States may also be labelled using the spectroscopic notation ${}^{2S+1}L_J$, where L, S and J

are the orbital, spin and total angular momentum; L is denoted by the S, P, D, F convention.

We are interested in the densities of ions in specific ionization stages and configurations. The generic symbol N for the density of ions in units of cm^{-3} is referred to with a subscript i, which corresponds to its charge; for example, in the case of carbon, N_5 refers to the number density of C^{5+} ions; $i = 0$ corresponds to a neutral atom. Densities may be further subscripted by j to denote the excited level, so that $N_{5,0}$ is the density of 5+ ions in the ground state. A given excited state may not correspond to a superconfiguration, as detailed in Appendix D. The density of ions in a given ionization stage is given by the sum over the excited states $N_i = \sum_j N_{i,j}$, and the total ion density by the sum over ionization stages $N_T = \sum_i N_i$. As discussed in §3.2, these ion densities are often assembled into a vector $\vec{N}$; the comma in the notation of $N_{i,j}$ distinguishes it from a rank-2 tensor.

The charge of an ion (and hence the maximum value of i) is denoted by Z. Ionization potentials, denoted by E_i, correspond to the energy of the transition $i - 1 \to i$; for example, for carbon E_5 is the ionization potential of the $C^{4+} \to C^{5+}$ transition. While E is reserved for well-defined energies, such as those of atomic transitions, ϵ is used for dynamically varying energies, such as the kinetic energy of electrons in a plasma; often these are dummy variables in a definite integral. Electron density is invariably denoted by n_e. The configuration energies are denoted by $E_{i,j}$, or sometimes simply by E_j.

B Mathematical methods

We present the mathematical functions, numerical methods for solutions of transcendental and differential equations, along with associated notation as used in this text.

B.1 Important functions

The Dirac δ-function is zero everywhere except the origin and satisfies the relations

$$\int_a^b \delta(x)dx = 1, \quad b > 0, a < 0,$$
$$\int_a^b \delta(x)f(x)dx = f(0), \quad b > 0, a < 0,$$
$$\int_a^b \delta(x)dx = \int_a^b \delta(x)f(x)dx = 0, \quad ab > 0.$$

The Kronecker delta δ_{ij} is the discrete equivalent of the continuous Dirac δ-function, non-vanishing for its indices taking equal values. Closely related is the Heaviside step function, which satisifies

$$\Theta(x) = \int_{-\infty}^{x} \delta(t)dt. \tag{184}$$

The Heaviside function $\Theta(x)$ is therefore zero and unity for negative and positive x respectively. It should be noted that $\Theta(0) = \frac{1}{2}$.

The Gaussian function is frequently used throughout the text for its useful properties. It is defined as

$$\mathcal{G}(x) = A \exp\left[-4 \ln 2 \left(\frac{x - x_0}{x_{1/2}}\right)^2\right], \tag{185}$$

where x_0 is the centre and $x_{1/2}$ is the full-width half maximum (FWHM), the distance between the two points at which the Gaussian is $A/2$. The integral of the Gaussian function over its entire domain is given by

$$\int_{-\infty}^{\infty} \mathcal{G}(x)dx = \frac{2A}{x_{1/2}}\sqrt{\frac{\ln 2}{\pi}}. \tag{186}$$

The integral over a subset of its domain is equivalent to the error function. For curve fitting, we also make use of the super-Gaussian function

$$\mathcal{G}_n(x) = A \exp\left[\left(\frac{x - x_0}{w}\right)^n\right], \tag{187}$$

where w is a measure of the width of the super-Gaussian peak and $n \in \mathbb{R}$ (not restricted to integers) adjusts the steepness of this peak.

Exponential integrals

The family of exponential integral functions is defined through the relation

$$\mathbf{E}_n(x) = \int_x^\infty \frac{\exp(-t)}{t^n} dt. \tag{188}$$

They are denoted in bold to distinguish them from ionization energies *etc.* Of particular importance is the function $\mathbf{E}_1$, which may be useful when integrating over the Maxwell-Boltzmann distribution. We are interested in definite integrals of the type

$$\int_Y^\infty \ln\left(\frac{\epsilon}{Y}\right) \exp\left(-\frac{\epsilon}{Z}\right) d\epsilon = Z \int_{Y/Z}^\infty \ln\left(\frac{Zt}{Y}\right) \exp(-t)\, dt, \tag{189}$$

simplified in this case by the substitution $t = \epsilon/Z$. We proceed integrating by parts,

$$\int_{Y/Z}^\infty \ln\left(\frac{Zt}{Y}\right) \exp(-t)\, dt = \left[-\ln\left(\frac{Zt}{Y}\right) \exp(-t)\right]_{t=Y/Z}^{t=\infty} + \int_{Y/Z}^\infty \frac{\exp(-t)}{t} dt. \tag{190}$$

The square brackets vanish: we have $\ln(1) = 0$ in the lower limit and since $\exp(t)$ grows faster than $\ln(t)$, the ratio in the upper limit also tends to zero. We therefore have

$$\int_Y^\infty \ln\left(\frac{\epsilon}{Y}\right) \exp\left(-\frac{\epsilon}{Z}\right) d\epsilon = Z\mathbf{E}_1\left(\frac{Y}{Z}\right). \tag{191}$$

The function $\mathbf{E}_1$ can be efficiently calculated by numerical methods.[107]

B.2 Tensors

Vectors and matrices are used in collisional-radiative modelling and in mathematical methods throughout this work. Vectors are denoted by an arrow, such as $\vec{v}$. Subscripts are used to denote the elements of tensors. For a matrix element A_{mn}, the rows are denoted by m and columns by n so that matrix multiplication can be implemented as usual: $u_m = \sum_n A_{mn} v_n$. The symbol $\mathbb{I}$ is used to denote the identity matrix, whose elements are δ_{ij}. The superscript symbol † is used to denote the transpose. Finally, we demonstrate that rate matrices, as presented in §3.2, cannot be directly inverted.

Theorem 1. A matrix M whose diagonals are the negative sum of their corresponding columns ($M_{nn} = -\sum_{m \neq n} M_{nm}$) is singular ($\det(M) = 0$).

Proof. The determinant of a matrix is unchanged by adding the elements of a row to the corresponding elements of another row.[108] It is therefore unchanged by adding to a given row all the others, leading its elements to be $\sum_m M_{nm} = \sum_{m \neq n} M_{nm} + M_{nn} = 0$. A matrix with one or more zero rows has a zero determinant.[109] This implies that M has no inverse.

B.3 Curve fitting

In this work, much use is made of curve fitting routines to parameterise a set of points obtained from experiments or simulations through an analytic function. Given a set of pairs of points (x_i, y_i), the aim is to minimise the χ^2 error

$$\chi^2 = \sum_i y_i - f(x_i, \vec{p}) \tag{192}$$

for some set of input parameters $\vec{p}$ to an appropriate function f. Minimisation algorithms attempt to approach the minimum point by perturbing the current best estimate of $\vec{p}$ by a step $\vec{h}$. The Jacobian matrix $J_{ij} = \partial f(x_i, \vec{p})/\partial p_j$ is often used to calculate $\vec{h}$.

Perhaps the most often used χ^2-minimisation algorithm is the Levenberg − Marquardt.[110] The step $\vec{h}$ is a solution to the equation

$$(J^\dagger J + \lambda \mathrm{diag}(J^\dagger J))\vec{h} = J^\dagger[\vec{y} - \vec{f}(\vec{p})], \tag{193}$$

where $\lambda > 0$ is some scalar damping term. The routine `curve_fit` in the `scipy.optimize` library of `Python` efficiently implements this algorithm and has been used throughout this work.

B.4 Root-finding algorithms

In this work, we encounter many equations without analytical solutions. In this case, we rearrange the equation in question so that the RHS, for example, is equal to zero, and then attempt to find its roots, *i.e.* the point where it vanishes. The roots are typically found iteratively. One of the best-known algorithms to find the root of an analytic function is the Newton-Raphson method, which approximates the function by its tangent. If x_i is an estimate for the root of a function f, then a

better estimate is given by

$$x_{i+1} = x_i - \frac{f(x_i)}{f'(x_i)}, \tag{194}$$

where f' is the function's derivative. If the exact derivative is replaced by a finite difference $\Delta f/\Delta x$, this is referred to as the secant method.

If only a single root of a function is known to lie in some interval $a \leq x \leq b$, then it may be found by repeated bisection of the interval. Each time, the root is localized to one half of the remaining interval. Similarly, if the function is known at several points on both sides of the root, then a spline may be fit to the points and used to interpolate to find the root. Depending on the number of known points, this leads to linear, quadratic, cubic *etc.* interpolation. Brent's algorithm[12] combines the above methods, choosing the optimal one at every iteration. The disadvantage is that, like the bisection method, it requires the presence of precisely one root in some interval. By contrast, the Newton-Raphson or secant methods will typically converge on a root for a well behaved function, though they are slower than Brent's algorithm and may fall into a basin of attraction, leading to an infinite cycle. Brent's algorithm is particularly important in this work as part of the `CRABS` code for finding the steady state electron density for a plasma at fixed temperature and total ion density, as described in §3.4.

B.5 Fast Fourier Transform

Fourier methods are extremely valuable in mathematics and are applied numerically via the Discrete Fourier Transform (DFT) to signal processing and to solve differential equations. They are particularly useful in diffraction, as outlined in Chapter 2. The DFT of an N-dimensional tensor g with M elements, such that $\{j \in \mathbb{Z} | 0 \leq j < M\}$, is given by

$$G_{k_0 \ldots k_{N-1}} = \sum_{j_0=0}^{M-1} \exp(\mp 2\pi i j_0 k_0/M) \cdots \sum_{j_{N-1}=0}^{M-1} \exp(\mp 2\pi i j_{N-1} k_{N-1}/M) g_{j_0 \ldots j_{N-1}}. \tag{195}$$

The $-$ and $+$ signs correspond to the DFT, labelled $\mathcal{F}$, and its inverse, labelled $\mathcal{F}^{-1}$, respectively.

A particularly efficient method for computing the DFT due to Cooley and Tukey[111] is the Fast Fourier Transform (FFT). The method factorises the exponentials to simplify calculations; for example, the exponential factor $\exp(-2\pi i/6)$ may be computed from $\exp(-2\pi i/12)$ through the identity $\exp(-2\pi i/6) \equiv \exp(-2\pi i/12)^2$ by a single multiplication, greatly speeding up the calculation. The FFT algorithm

is implemented by the freely available `C` library `FFTW`[112] ("Fastest Fourier Transform in the West"), which has been very highly optimised for modern computers.

B.6 Numerical integration

Calculating a definite integral of a function which cannot be integrated analytically is often referred to as quadrature. All the methods of quadrature transform a continuous integral into a discrete sum of the integrand evaluated at many points x_i (called nodes or abscissae),

$$\int_a^b f(x)dx \approx \sum_{j=0}^{N} w_j f(x_j), \tag{196}$$

where $N+1$ is the total number of function evaluations and w_j are weights, specific to the numerical method.

Most familiar are the Newton-Cotes type of formula, where x_j are spaced regularly by $\Delta x = (b-a)/N$. The simplest practical method is trapezoidal, where $w_j = \Delta x/2$ for $j = 0, N$ and Δx otherwise. There are higher-order Newton-Cotes methods,[113,114] with more complicated weights which allowing higher-order polynomials to be integrated exactly.

More complicated quadrature methods require the limits of the integral to be exactly -1 and $+1$. We recast a general integral using the transformation

$$t = \frac{2x-b-a}{b-a}, \tag{197}$$

so that the integral becomes

$$\int_a^b f(x)dx = \frac{b-a}{2}\int_{-1}^{1} f(t)dt. \tag{198}$$

The Curtis-Clenshaw integral formula is derived by attempting to expand $f(t)$ as a series of Chebyshev polynomials,[113] which gives

$$\int_{-1}^{1} f(t)dt = -\frac{4}{N}\sum_{j=0}^{N} f\left(\cos(\pi j/N)\right)\sum_{k=0}^{N/2}\frac{\cos(2\pi jk/N)}{k^2-1}. \tag{199}$$

The weights w_i are comprised of a sum over cosines at each node. Given that $\mathrm{Re}\{\exp(2\pi jk/N)\} = \cos(2\pi jk/N)$, it is possible to calculate the weights efficiently by performing an FFT.

The method of Gaussian quadrature recasts the weights and nodes in terms of coupled linear equations, which may be efficiently solved by matrix methods. An

algorithm by Golub and Welsch[115,116] allows the calculation of Gaussian nodes and weights from a symmetric tridiagonal matrix J, whose non-zero elements are given by

$$J_{j+1,j} = J_{j,j+1} = \frac{1}{2\sqrt{1-(2j)^2}}. \tag{200}$$

Let the eigenvectors and eigenvalues of J be denoted by $\vec{v}_j$ and λ_j respectively. Then the Gaussian integral becomes

$$\int_{-1}^{1} f(t)dt = 2\sum_{j=0}^{N}(v_{j,0})^2 f\left(\lambda_j\right), \tag{201}$$

where $v_{j,0}$ is the 0^{th} element of the j^{th} eigenvector. As the matrix J is real, symmetric and tridiagonal, specialised algorithms may be used for its matrix decomposition; the commonly used LAPACK algorithms contain the function `stev` for this purpose.[87]

The above three methods have been listed in order of their accuracy (for a given N). It is clear by inspection that the increase in efficiency of the latter two methods comes at a cost of having to compute the non-trivial weights and nodes. This cost is offset when many repeated integrals are performed with the same N, as nodes and weights may be reused each time, even if the limits a and b are different.

Solution of differential equations

We frequently require finding a solution to a set of coupled differential equations for a set of variables, starting with some initial conditions. It is useful to write the variables in a vector $\vec{y}$, so that they satisfy

$$\frac{d\vec{y}}{dt} = f\left(t, \vec{y}\right). \tag{202}$$

They can then be solved by discretising t and iterating from an initial boundary condition $\vec{y}(t_0)$ to obtain the value $\vec{y}(t_n)$ at each discrete point in time. It is possible to solve Equation (202) naively using the formula $\vec{y}(t_{n+1}) = \vec{y}(t_n) + f(t_n, \vec{y}(t_n))\Delta t$, but a much more accurate approach is to use the 4^{th}-order Runge-Kutta formula[117] (often referred to as RK4),

$$\vec{y}_{n+1} = \vec{y}_n + \frac{1}{6}\Delta t\left(\vec{k}_1 + 2\vec{k}_2 + 2\vec{k}_3 + \vec{k}_4\right), \tag{203}$$

where the coefficients are given by

$$\begin{aligned}
\vec{k}_1 &= f\left(t_n, \vec{y}_n\right), \\
\vec{k}_2 &= f\left(t_n + \Delta t/2, \vec{y}_n + \vec{k}_1 \Delta t/2\right), \\
\vec{k}_3 &= f\left(t_n + \Delta t/2, \vec{y}_n + \vec{k}_2 \Delta t/2\right), \\
\vec{k}_4 &= f\left(t_n + \Delta t, \vec{y}_n + \vec{k}_3 \Delta t\right).
\end{aligned}$$

This algorithm has an error of order Δt^5, compared to Δt^2 for the simple method. Runge-Kutta methods with more $\vec{k}$ coefficients exist, with errors of correspondingly higher orders.

C Properties of the Fermi-Dirac distribution

The statistics of electrons, two of which may not occupy the same quantum state, are determined by the Fermi-Dirac energy distribution. This distribution is mathematically and computationally challenging because it requires the chemical potential to be known. The chemical potential is defined transcendentally, through the integral in Equation (73). The application of the Fermi-Dirac distribution is relevant to warm dense matter and to the shell and fuel during inertial fusion compression. It is therefore worthwhile to examine some of the mathematical features of the chemical potential.

At $T = 0$, the chemical potential takes a value of the Fermi energy, $\mu(0) = E_F$, as in Equation (75). At high temperatures, we require that the chemical potential approach the asymptotic form $\bar{\mu}(T) = T \ln\left[(4/3\sqrt{\pi})\,(E_F/T)^{3/2}\right]$. We show in this section that the chemical potential decreases as the temperature decreases and approaches $\bar{\mu}$ asymptotically.

Theorem 2. For a given fixed electron density n_e, the chemical potential is a monotonically decreasing function of temperature.

Proof. For a function to decrease monotonically, its derivative must be everywhere negative. Differentiating Equation (73), we have

$$\frac{d\mu}{dT} = -T\frac{\int_0^\infty (\epsilon-\mu)\sqrt{\epsilon}A d\epsilon}{\int_0^\infty \sqrt{\epsilon}A d\epsilon}, \tag{204}$$

$$A = \exp\left(\frac{\epsilon-\mu}{T}\right)\left[1+\exp\left(\frac{\epsilon-\mu}{T}\right)\right]^{-2}. \tag{205}$$

T, ϵ and A are positive and therefore μ decreases monotonically if the numerator is positive: $\int_0^\infty (\epsilon-\mu)\sqrt{\epsilon}A d\epsilon > 0$. For $\mu < 0$, the factor $(\epsilon-\mu)$ becomes positive, as are all other factors in the integrand, so the condition is satisfied.

For $\mu > 0$, we split the integral into three parts: $\int_0^\infty (\epsilon-\mu)\sqrt{\epsilon}A d\epsilon = \int_{2\mu}^\infty (\epsilon-\mu)\sqrt{\epsilon}A d\epsilon + \int_\mu^{2\mu} (\bar{\epsilon}-\mu)\sqrt{\bar{\epsilon}}A d\bar{\epsilon} + \int_0^\mu (\epsilon-\mu)\sqrt{\epsilon}A d\epsilon$, where we have chosen a different variable of integration in the second integral. The first part is positive, since $\epsilon > \mu$. For the second integral, we make the substitution $\epsilon = 2\mu - \bar{\epsilon}$, leading to

$$\int_\mu^{2\mu} \frac{(\bar{\epsilon}-\mu)\sqrt{\bar{\epsilon}}\exp\left(\frac{\bar{\epsilon}-\mu}{T}\right)}{\left[1+\exp\left(\frac{\bar{\epsilon}-\mu}{T}\right)\right]^2} d\bar{\epsilon} = \int_0^\mu (\mu-\epsilon)\sqrt{2\mu-\epsilon}A d\epsilon. \tag{206}$$

The new limits allow two integrals to be combined together, meaning that we require $\int_0^\mu (\mu-\epsilon)(\sqrt{2\mu-\epsilon}-\sqrt{\epsilon})A d\epsilon > 0$. Given the limits, $0 \le \epsilon \le \mu$, we see that both brackets are positive and therefore $\frac{d\mu}{dT}$ is negative as required.

Theorem 3. The chemical potential $\mu(T)$ is always greater than its asymptotic form $\bar{\mu}(T)$.

Proof. From Equation (73), we have that

$$\frac{3}{2E_F^{3/2}} \int_0^\infty \frac{\sqrt{\epsilon}}{1 + \exp[(\epsilon - \mu)/T]} d\epsilon = 1.$$

Given that all the quantities are real, the relation $1 + \exp[(\epsilon - \mu)/T] > \exp[(\epsilon - \mu)/T]$ leads to

$$\frac{3}{2E_F^{3/2}} \int_0^\infty \frac{\sqrt{\epsilon}}{\exp[(\epsilon - \mu)/T]} d\epsilon > 1,$$

which simplifies to

$$\frac{3}{2} \left(\frac{T}{E_F}\right)^{3/2} \exp(\mu/T) \int_0^\infty \frac{\sqrt{\epsilon/T}}{\exp[\epsilon/T]} d(\epsilon/T) > 1.$$

Using the familiar definite integral $\int_0^\infty \sqrt{x} \exp(-x) dx = \sqrt{\pi}/2$, this simplifies to

$$\frac{3\sqrt{\pi}}{4} \left(\frac{T}{E_F}\right)^{3/2} \exp(\mu/T) > 1.$$

Rearranging and substituting the definition of $\bar{\mu}(T)$ from Equation (77), we see indeed that $\mu(T) > \bar{\mu}(T)$.

D Superconfiguration atomic models

In Chapter 3, we have discussed atomic rates which are repsonsible for exciting ions in a plasma to highly energetic quantum states. Determining the proportion of ions in a given state is central to determining the emissivities and opacities of plasmas used for spectroscopy and radiation-hydrodynamics. The quantum state of an atom is one of infinitely many solutions to the Schrödinger equation. In a realistic plasma, continuum lowering reduces the number of possible states to a finite number.[78] The problem becomes solvable, but nonetheless computationally very expensive.

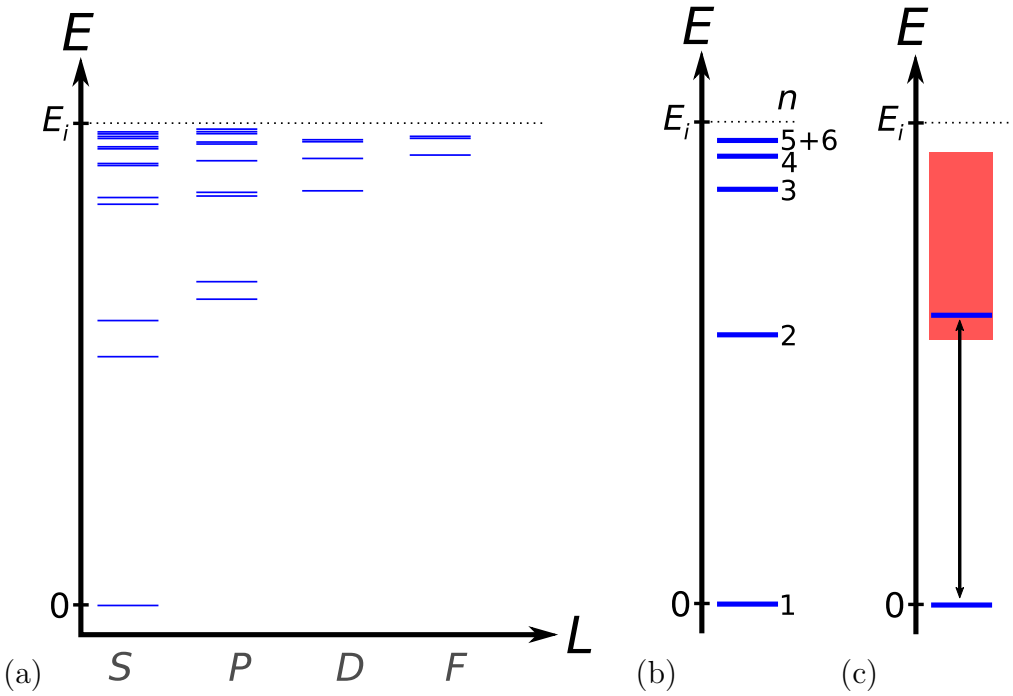

Figure 57: Grotrian diagrams for neutral helium (drawn approximately to scale); autoionizing states are not shown here. (a) A selection of individual quantum states plotted by energy and orbital angular momentum; data from NIST.[71] (b) A superconfiguration approach, where the individual levels have been grouped by principal quantum number n. (c) The approach in the current work, grouping the significant levels into a single excited state.

One approach commonly used to reduce this computational load is to take a weighted average over many similar quantum states to gather them together into a single "superconfiguration".[97,98] The occupation of states in such a superconfiguration is then always assumed to be in LTE and therefore given by the Boltzmann ratio

$$\frac{N_{i,j'}}{N_{i,j}} = \frac{g_{j'}}{g_j} \exp(E_j/T_e). \tag{207}$$

This approach is justified for levels closely spaced in energy, because then the collisional rates between these levels are extremely high. A small threshold energy increases the integral in Equation (90); furthermore, the cross sections for such processes are typically large. For example, transitions involving a single spin "flip" or change in orbital angular momentum (but no change in principal quantum number) have these properties. For this reason, states may be grouped into superconfigurations by n, the principal quantum number.[96] As n increases, the states are ever more closely spaced and therefore can be grouped further. This is shown for neutral helium in Figure 57b. States with very high n are generally extremely close to LTE as a result of their energy spacing[118] or are not present because of continuum lowering.

After grouping atomic levels into superconfigurations, appropriate cross sections must be obtained for the atomic rate coefficients. The Lotz and Van Regemorter formulas require only an effective ionization/excitation energy and oscillator strength in the latter case. A more level-specific cross section, such as that of Equation (97), can be obtained by curve fitting;[98] atomic databases frequently offer such superconfiguration-averaged cross sections.[21]

The atomic model used in this work is a further simplification of the superconfiguration approach. We group all the levels for principal quantum number $n \geq 2$ into a single excited level; the $n = 1$ grouping corresponds to the ground level. The simple Boltzmann ratio of Equation (207) ensures that the ground state is almost invariably the most highly populated in equilibrium. Transitions to excited states are "bottlenecked" through the fastest transition from the ground state, because the redistribution between $n \geq 2$ is comparatively much faster. We therefore take the highest cross section to calculate the excitation rate between the two atomic levels of each ionization stage, or the sum of several cross sections in the case where atomic data is available and their magnitude is comparable. This approach makes possible the time-dependent collisional-radiative calculations presented in Chapter 4, but is not suitable for detailed spectroscopic analysis, for example, where transitions from fine structure levels must be resolved.

E Focal point coordinates

Consider a curve C in 2-dimensional Cartesian space passing through the set of points with coordinates (x_0, y_0). Each point on this curve is parameterised by a single unique variable α, namely $x_0 = x_0(\alpha)$, $y_0 = y_0(\alpha)$. A line L is perpendicular to the tangent to the curve at the point with coordinate α. $|\beta|$ is the distance along L; the sign of beta determines the direction along L. Therefore, a pair of coordinates α, β can be used to specify a point in the 2-dimensional space with Cartesian coordinates (x, y) as shown in Figure 58a.

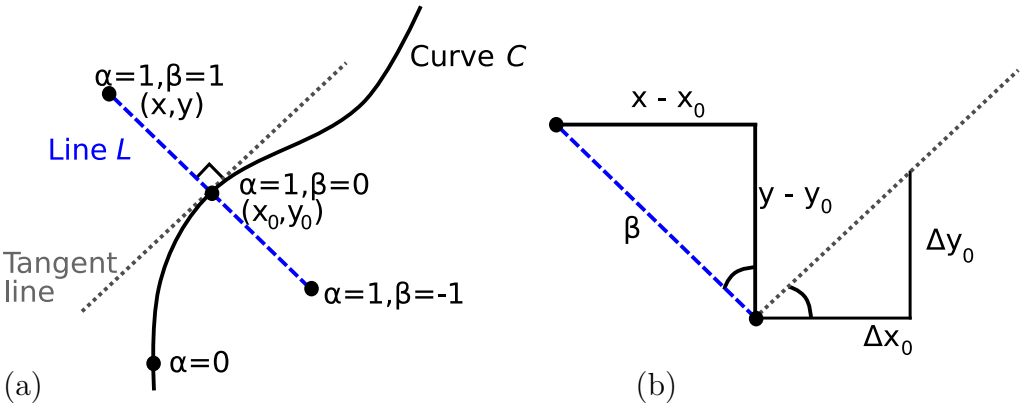

Figure 58: (a) A system of coordinates relative to a curve C, where α is equivalent to the position along the curve and β to the perpendicular distance from it. (b) The region around the tangent line, showing the relationship between the local gradient and displacement.

We are interested in converting between Cartesian coordinates and this new coordinate system. Figure 58b makes clear that by using the properties of similar triangles and Pythagoras's theorem respectively, we have that

$$\frac{x - x_0}{y - y_0} = \frac{dy_0}{dx_0} = \frac{dy_0}{d\alpha}\left(\frac{dx_0}{d\alpha}\right)^{-1}, \tag{208}$$

$$\beta = \sqrt{(x - x_0)^2 + (y - y_0)^2}. \tag{209}$$

After rearranging, this leads to

$$x - x_0 + (y - y_0)\frac{dy_0}{dx_0} = 0, \tag{210}$$

$$\beta = (y - y_0)\sqrt{1 + \left(\frac{dy_0}{dx_0}\right)^2}. \tag{211}$$

A root-finding routine can be used to calculate α from Equation (210) and use it to calculate β from Equation (211). There are two considerations when transforming

between the two aformentioned coordinate systems. Firstly, the set of acceptable values of α and β for a given curve may not span the entire Cartesian space; on the other hand, it is guaranteed that there is a Cartesian coordinate for every possible α and β. Secondly, a given curve may have a one-to-many relationship between a given Cartesian coordinate (which is unique) and pairs of α, β.

This coordinate system may be readily applied to the parameterisation of the asymmetric intensity profiles close to focus, as encountered in Chapter 5. The curve C (such as those in Figure 54) is chosen to run along the local peak intensity, so that the intensity variation is strongest perpendicular to C (along β). The intensity at every point on the curve $I(\alpha)$ is then used to impose the appropriate depth profile along β; examples of the profiles which would be imposed for $I(\alpha) = 10^{10}$ and $I(\alpha) = 2.5 \times 10^{10}$ W cm^{-2} are given in Figure 53. This approach treats the hydrodynamics along β as essentially 2-dimensional, because the intensity variation is small parallel to C (along α) and therefore so too are the flux of heat and momentum in this direction.

References

[1] A. K. Rossall, V. Aslanyan, and G. J. Tallents, "High energy density plasmas produced by x-ray and extreme ultraviolet lasers", Proceedings of SPIE **8849**, 884912 (2013).

[2] V. Aslanyan and G. J. Tallents, "Local thermodynamic equilibrium in rapidly heated high energy density plasmas", Phys. Plasmas **21**, 062702 (2014).

[3] A. K. Rossall, V. Aslanyan, G. J. Tallents, I. Kuznetsov, J. J. Rocca, and C. S. Menoni, "Ablation of Submicrometer Holes Using an Extreme-Ultraviolet Laser", Phys. Rev. Applied **3**, 064013 (2015).

[4] V. Aslanyan and G. J. Tallents, "Ionization rate coefficients in warm dense plasmas", Phys. Rev. E **91**, 063106 (2015).

[5] V. Aslanyan and G. J. Tallents, "Opacity Bleaching by Extreme Ultraviolet Radiation Incident on Solid Density Targets", Springer Proceedings in Physics **169**, 391 (2016).

[6] W. Li, L. Urbanski, and M. C. Marconi, "Progress in coherent lithography using table-top extreme ultraviolet lasers", Rev. Sci. Instrum. **86**, 121301 (2015).

[7] J. P. Cox and R. T. Giuli, *Principles of Stellar Structure Volume II: Applications to Stars* (Gordon and Breach Science Publishers, 1968).

[8] R. L. Sandberg, C. Song, P. W. Wachulak, D. A. Raymondson, A. Paul, B. Amirbekian, E. Lee, A. E. Sakdinawat, C. La-O-Vorakiat, M. C. Marconi, C. S. Menoni, M. M. Murnane, J. J. Rocca, H. C. Kapteyn, and J. Miao, "High numerical aperture tabletop soft x-ray diffraction microscopy with 70-nm resolution", PNAS **105**, 24 (2008).

[9] M. A. Purvis, J. Grava, J. Filevich, D. P. Ryan, S. J. Moon, J. Dunn, V. N. Shlyaptsev, and J. J. Rocca, "Collimation of dense plasma jets created by low-energy laser pulses and studied with soft x-ray laser interferometry", Phys Rev E **81**, 036408 (2010).

[10] J. Filevich, K. Kanizay, M. C. Marconi, J. L. A. Chilla, and J. J. Rocca, "Dense plasma diagnostics with an amplitude-division soft-x-ray laser interferometer based on diffraction gratings", Optics Letters **25**, 356 (2000).

[11] I. Kuznetsov, J. Filevich, F. Dong, M. Woolston, W. Chao, E. H. Anderson, E. R. Bernstein, D. C. Crick, J. J. Rocca, and C. S. Menoni, "Three-dimensional nanoscale molecular imaging by extreme ultraviolet laser ablation mass spectrometry", Nature Communications **6**, 6944 (2015).

[12] R. P. Brent, *Algorithms for Minimisation without Derivatives*, p. 47 (Prentice Hall, 1972).

[13] D. J. Hoarty, S. F. James, C. R. D. Brown, B. M. Williams, H. -K. Chung, J. W. O. Harris, L. Upcraft, B. J. B. Crowley, C. C. Smith, and R. W. Lee, "Measurements of emission spectra from hot, dense germanium plasma in short pulse laser experiments", High Energy Density Physics **6**, 105 (2010).

[14] K. Eidmann, U. Andiel, F. Pisani, P. Hakel, R. C. Mancini, G. C. Junkel-Vives, J. Abdallah, and K. Witte, "K-shell spectra from hot dense aluminum layers buried in carbon and heated by ultrashort laser pulses", Journal of Quantitative Spectroscopy and Radiative Transfer **81**, 133 (2003).

[15] S. C. Wilks, H. Chen, E. Liang, P. Patel, D. Price, B. Remington, R. Shepherd, M. Tabak, and W. L. Kruer, "Electron-Positron Plasmas Created By Ultra-Intense Laser Pulses Interacting With Solid Targets", *High Energy Density Laboratory Astrophysics* p. 347 (Springer, 2005).

[16] G. Sarri, K. Poder, J. M. Cole, W. Schumaker, A. Di Piazza, B. Reville, T. Dzelzainis, D. Doria, L. A. Gizzi, G. Grittani, S. Kar, C. H. Keitel, K. Krushelnick, S. Kuschel, S. P. D. Mangles, Z. Najmudin, N. Shukla, L. O. Silva, D. Symes, A. G. R. Thomas, M. Vargas, J. Vieira, and M. Zepf, "Generation of neutral and high-density electron-positron pair plasmas in the laboratory", Nature Communications **6**, 6747 (2015).

[17] H. M. Mott-Smith, "History of *Plasmas*", Nature, **233**, 219 (1971).

[18] R. O. Dendy, *Plasma Physics: An Introductory Course* (CUP, 1995).

[19] L. Spitzer, *Physics of Fully Ionized Gases* (New York: Interscience, 2nd edition, 1962).

[20] A. R. Bell, R. G. Evans, and D. J. Nicholas, "Elecron Energy Transport in Steep Temperature Gradients in Laser-Produced Plasmas", Phys. Rev. Lett. **46**, 243 (1981).

[21] Web interface to the Los Alamos atomic physics codes, *http://aphysics2.lanl.gov/tempweb/* (Accessed 20/03/15).

[22] G. J. Pert, *Introductory Fluid Mechanics for Physicists and Mathematicians* (Wiley, 2013).

[23] D. J. Acheson, *Elementary Fluid Dynamics*, p. 205 (OUP, 1990).

[24] G. J. Pert, "Two-dimensional hydrodynamic models of laser-produced plasmas", J. Plasma Phys. **41**, 263 (1989).

[25] S. L. Thompson, Sandia National Laboratories Report No. SC-RR-70-2 (1970).

[26] S. Hooker and C. Webb, *Laser Physics* (OUP, 2010).

[27] B. H. Bransden and C. J. Joachain, *Quantum Mechanics, Second Edition*, p. 446 (Pearson Education, 2000).

[28] G. J. Tallents, "The physics of soft x-ray lasers pumped by electron collisions in laser plasmas", J. Phys. D: Appl. Phys. **36**, R259 (2003).

[29] Y. Wang, M. A. Larotonda, B. M. Luther, D. Alessi, M. Berrill, V. N. Shlyaptsev, and J. J. Rocca, "Demonstration of high-repetition-rate tabletop soft-x-ray lasers with saturated output at wavelengths down to 13.9 nm and gain down to 10.9 nm", Phys. Rev. A **72**, 053807 (2005).

[30] S. Sebban, R. Haroutunian, Ph. Balcou, G. Grillon, A. Rousse, S. Kazamias, T. Marin, J. P. Rousseau, L. Notebaert, M. Pittman, J. P. Chambaret, A. Antonetti, D. Hulin, D. Ros, A. Klisnick, A. Carillon, P. Jaeglé, G. Jamelot, and J. F. Wyart, "Saturated Amplification of a Collisionally Pumped Optical-Field-Ionization Soft X-Ray Laser at 41.8 nm", Phys. Rev. Lett. **86**, 3004 (2001).

[31] D. V. Korobkin, C. H. Nam, S. Suckewer, and A. Goltsov, "Demonstration of Soft X-Ray Lasing to Ground State in Li III", Phys. Rev. Lett. **77**, 5206 (1996).

[32] S. Basu, P. L. Hagelstein, J. G. Goodberlet, M. H. Muendel, and S. Kaushik, "Amplification in Ni-Like Nb at 204.2 Å Pumped by a Table-Top Laser", Appl. Phys. B **57**, 303 (1993).

[33] A. Schütze, J. Y. Jeong, S. E. Babayan, J. Park, G. S. Selwyn, and R. F. Hicks, "The Atmospheric-Pressure Plasma Jet: A Review and Comparison to Other Plasma Sources", IEEE Transactions On Plasma Science, **26**, 1685 (1998).

[34] S. Heinbuch, M. Grisham, D. Martz, and J.J. Rocca, "Demonstration of a desk-top size high repetition rate soft x-ray laser", Optics Express, **13**, 4050 (2005).

[35] I. Gissis, A. Rikanati, I. Be'ery, A. Fisher, and E. Behar, "Time-resolved grating spectroscopy of a N capillary discharge plasma for a recombination pumped x-ray laser", J. Quant. Spectrosc. Radiat. Transfer **127**, 176 (2013).

[36] H. Bravo, B. T. Szapiro, P. W. Wachulak, M. C. Marconi, W. Chao, E. H. Anderson, C. S. Menoni, and J. J. Rocca, "Demonstration of Nanomachining With Focused Extreme Ultraviolet Laser Beams", IEEE Journal Of Selected Topics In Quantum Electronics **18**, 443 (2012).

[37] Website of the Engineering Research Center for EUV Science and Technology, *http://euverc.colostate.edu/* (Accessed 23/11/15).

[38] J. D. Jackson, *Classical Electrodynamics, Third Edition* (Wiley, 1998).

[39] S. V. Milton, E. Gluskin, N. D. Arnold, C. Benson, W. Berg, S. G. Biedron, M. Borland, Y. C. Chae, R. J. Dejus, P. K. Den Hartog, B. Deriy, M. Erdmann, Y. I. Eidelman, M. W. Hahne, Z. Huang, K. J. Kim, J. W. Lewellen, Y. Li, A. H. Lumpkin, O. Makarov, E. R. Moog, A. Nassiri, V. Sajaev, R. Soliday, B. J. Tieman, E. M. Trakhtenberg, G. Travish, I. B. Vasserman, N. A. Vinokurov, X. J. Wang, G. Wiemerslage, and B. X. Yang, "Exponential Gain and Saturation of a Self-Amplified Spontaneous Emission Free-Electron Laser", Science **292**, 2037 (2001).

[40] Website of CERN, *http://press.web.cern.ch/press-releases/1999/08/energy-record-gives-lep-new-discovery-possibilities* (Accessed 01/11/15).

[41] P. Emma, R. Akre, J. Arthur, R. Bionta, C. Bostedt, J. Bozek, A. Brachmann, P. Bucksbaum, R. Coffee, F. J. Decker, Y. Ding, D. Dowell, S. Edstrom, A. Fisher, J. Frisch, S. Gilevich, J. Hastings, G. Hays, Ph. Hering, Z. Huang, R. Iverson, H. Loos, M. Messerschmidt, A. Miahnahri, S. Moeller, H. D. Nuhn, G. Pile, D. Ratner, J. Rzepiela, D. Schultz, T. Smith, P. Stefan, H. Tompkins, J. Turner, J. Welch, W. White, J. Wu, G. Yocky, and J. Galayda, "First lasing and operation of an angstrom-wavelength free-electron laser", Nature Photonics **4**, 641 (2010).

[42] Website of the European XFEL project, *http://www.xfel.eu/overview/facts_and_figures/* (Accessed 04/11/15).

[43] J. Mompart and R. Corbalán, "Lasing without inversion", J. Opt. B: Quantum Semiclass. Opt. **2**, R7 (2000).

[44] L. Yuan, D. Wang, A. A. Svidzinsky, H. Xia, O. Kocharovskaya, A. Sokolov, G. R. Welch, S. Suckewer, and M. O. Scully, "Transient lasing without inversion via forbidden and virtual transitions", Phys. Rev. A **89**, 013814 (2014).

[45] E. Hecht, *Optics, Third Edition* (Addison Wesley, 1998).

[46] M. Maggiore, *A Modern Introduction to Quantum Field Theory* (OUP, 2005).

[47] J. W. Goodman, *Introduction to Fourier Optics, Second Edition* (McGraw-Hill, 1996).

[48] Wolfram MathWorld, Bessel function of the first kind, *http://mathworld.wolfram.com/BesselFunctionoftheFirstKind.html* (Accessed 30/01/16).

[49] I. N. Bronshtein, K. A. Semendyayev, G. Musiol, and H. Muehlig, *Handbook of Mathematics, Fourth Edition*, p. 705 (Springer-Verlag 2004).

[50] D. R. Hartree, "The evaluation of a diffraction integral", Mathematical Proceedings of the Cambridge Philosophical Society **50**, 567 (1954).

[51] U. T. Ehrenmark, "A three-point formula for numerical quadrature of oscillatory integrals with variable frequency", J. Comp. Appl. Math. **21**, 87 (1988).

[52] W. Kahan, "Further remarks on reducing truncation errors", Communications of the ACM **8**, 40 (1965).

[53] Website of J. C. Wyant, *http://wyant.optics.arizona.edu/fresnelZones/fresnelZones.htm* (Accessed 13/10/14).

[54] M. A. Dupertuis, M. Proctor and B. Acklin, "Generalization of complex Snell-Descartes and Fresnel laws", J. Opt. Soc. Am. A **11**, 1159 (1993).

[55] S. A. Kovalenko, "Descartes-Snell law of refraction with absorption", SQO **4**, 214 (2001).

[56] D. L. Windt, "IMD - Software for modeling the optical properties of multilayer films", Computers in Physics, **12**, 360 (1998).

[57] IMD section of the website of Reflective X-ray Optics LLC, *http://www.rxollc.com/idl/* (Accessed 23/07/2015).

[58] A. Yu. Okulov, "Two-dimensional periodic structures in a nonlinear resonator", J. Opt. Soc. Am. B **7**, 1045 (1990).

[59] H. F. Talbot, "Facts relating to Optical Science", The London and Edinburgh Philosophical Magazine and Journal of Science **9**, 401 (1836).

[60] L. Urbanski, A. Isoyan, A. Stein, J.J. Rocca, C. S. Menoni, and M. C. Marconi, "Defect-tolerant extreme ultraviolet nanoscale printing", Optics Letters **37**, 3633 (2012).

[61] Newport Corporation's optical materials reference webpage, *http://www.newport.com/Optical-Materials/144943/1033/content.aspx* (Accessed 22/06/2015).

[62] F. Seiboth, A. Schropp, R. Hoppe, V. Meier, J. Patommel, H. J. Lee, B. Nagler, E. C. Galtier, B. Arnold, U. Zastrau, J. B. Hastings, D. Nilsson, F. Uhlen, U. Vogt, H. M. Hertz, and C. G. Schroer, "Focusing XFEL SASE pulses by rotationally parabolic refractive x-ray lenses", J. Phys.: Conf. Ser. **499**, 012004 (2014).

[63] S. J. Blundell and K. M. Blundell, *Concepts in Thermal Physics* (OUP, 1975).

[64] S. A. Khrapak, A. V. Ivlev, G. E. Morfill, and H. M. Thomas, "Ion drag force in complex plasmas", Phys. Rev. E **66**, 046414 (2002).4

[65] F. Reif, *Fundamentals of Statistical and Thermal Physics* (Waveland Press, 2009).

[66] V. V. Karasiev, D. Chakraborty and S. B. Trickey, "Improved analytical representation of combinations of Fermi-Dirac integrals for finite-temperature density functional calculations", Computer Physics Communications **192**, 114 (2015).

[67] P. Wurfel, "The chemical potential of radiation", J. Phys. C: Solid State Phys. **15**, 3967 (1982).

[68] M. Poirier and F. de Gaufridy de Dortan, "A comparison between detailed and configuration-averaged collisional-radiative codes applied to nonlocal thermal equilibrium plasmas", J. App. Phys. **101**, 063308 (2007).

[69] H. Suno and T. Kato, "Cross section database for carbon atoms and ions", ADNDT **92**, 407 (2006).

[70] H. Van Regemorter, "Rate of Collisional Excitation in Stellar Atmospheres", ApJ **136**, 906 (1962).

[71] National Institute of Standards and Technology atomic spectra database, *http://www.nist.gov/pml/data* (Accessed 17/03/2015).

[72] J. Oxenius, *Kinetic Theory of Particles and Photons: Theoretical Foundations of Non-LTE Plasma Spectroscopy* (Springer-Verlag, 1986).

[73] Wolfram MathWorld, handshake problem, *http://mathworld.wolfram.com/HandshakeProblem.html* (Accessed 20/08/2014).

[74] K. L. Bell, H. B. Gilbody, J. G. Hughes, A. E. Kingston, and F. J. Smith, "Recommended Data on the Electron Impact Ionization of Light Atoms and Ions", J. Phys. Chem. Ref. Data **12**, 891 (1983).

[75] W. Lotz, "Electron-Impact Ionization Cross-Sections for Atoms up to Z=108*", Z. Physik **2**, 232 (1970).

[76] N. Oda, "Energy and Angular Distributions of Electrons from Atoms and Molecules by Electron Impact", Radiat. Res. **64**, 80 (1975).

[77] H. Ehrhardt, K. Jung, G. Knoth, and P. Schlemmer, "Differential Cross Sections of Direct Single Electron Impact Ionization", Z. Phys. D Atoms **1**, 3 (1986).

[78] D. Salzmann, *Atomic Physics in Hot Plasmas* (OUP, 1997).

[79] B. F. Rozsnyai and V. L. Jacobs, "Photorecombination rates of hydrogenic and nonhydrogenic states", ApJ **327**, 485 (1988).

[80] G. Bekefi, *Radiation Processes in Plasmas* (Wiley, 1966).

[81] I. H. Hutchinson, *Principles of Plasma Diagnostics* (CUP, 1987).

[82] J. Stewart and K. Pyatt, "Lowering of Ionization Potentials in Plasmas", ApJ **144**, 1203 (1966).

[83] G. Ecker and W. Kröll, "Lowering of the Ionization Energy for a Plasma in Thermodynamic Equilibrium", Phys. Fluids **6**, 62 (1963).

[84] D. J. Hoarty, P. Allan, S. F. James, C. R. D. Brown, L. M. R. Hobbs, M. P. Hill, J. W. O. Harris, J. Morton, M. G. Brookes, R. Shepherd, J. Dunn, H. Chen, E. Von Marley, P. Beiersdorfer, H. -K. Chung, R. W. Lee, G. Brown, and

J. Emig, "Observations of the Effect of Ionization-Potential Depression in Hot Dense Plasma", Phys. Rev. Lett. **110**, 265003 (2013).

[85] O. Ciricosta, S. M. Vinko, H. -K. Chung, B. -I. Cho, C. R. D. Brown, T. Burian, J. Chalupsky, K. Engelhorn, R. W. Falcone, C. Graves, V. Hajkova, A. Higginbotham, L. Juha, J. Krzywinski, H. J. Lee, M. Messerschmidt, C. D. Murphy, Y. Ping, D. S. Rackstraw, A. Scherz, W. Schlotter, S. Toleikis, J. J. Turner, L. Vysin, T. Wang, B. Wu, U. Zastrau, D. Zhu, R. W. Lee, P. Heimann, B. Nagler, and J. S. Wark, "Direct Measurements of the Ionization Potential Depression in a Dense Plasma", Phys. Rev. Lett. **109**, 065002 (2012).

[86] B. J. B. Crowley, "Continuum Lowering - A New Perspective", High Energy Density Physics **13**, 84 (2014).

[87] LAPACK website, *http://www.netlib.org/lapack/* (Accessed 25/09/15).

[88] G. Cristoforetti, E. Tognoni, and L. A. Gizzi, "Thermodynamic equilibrium states in laser-induced plasmas: From the general case to laser-induced breakdown spectroscopy plasmas", Spectrochimica Acta Part B **90**, 1 (2013).

[89] M. R. Zaghloul, M. A. Bourham, and J. M. Doster, "A simple formulation and solution strategy of the Saha equation for ideal and nonideal plasmas", J. Phys. D: Appl. Phys. **33**, 977 (2000).

[90] R. W. P. McWhirter *Plasma Diagnostic Techniques,* R. H. Huddlestone and S. L. Leonard, Eds. (Academic Press, New York, 1965).

[91] T. Fujimoto and R. W. P. McWhirter, "Validity criteria for local thermodynamic equilibrium in plasma spectroscopy", Phys. Rev. A **42**, 6588 (1990).

[92] G. Cristoforetti, A. De Giacomo, M. Dell'Aglio, S. Legnaioli, E. Tognoni, V. Palleschi and N. Omenetto, "Local Thermodynamic Equilibrium in Laser-Induced Breakdown Spectroscopy: Beyond the McWhirter criterion", Spectrochimica Acta Part B **65**, 86 (2010).

[93] P. Jönsson, X. He, C. Froese Fischer and I. P. Grant, "The grasp2K relativistic atomic structure package", Computer Physics Communications **177**, 597 (2007).

[94] Website of the PrismSPECT code, *http://www.prism-cs.com/Software/PrismSpect/PrismSPECT.htm* (Accessed 27/11/13).

[95] J. J. MacFarlane, I. E. Golovkin, P. R. Woodruff, D. R. Welch, B. V. Oliver, T. A. Mehlhorn and R. B. Campbell, "Simulation of the Ionization Dynamics of Aluminum Irradiated by Intense Short-Pulse Lasers", Inertial Fusion Sciences and Application, 457 (2003).

[96] H. -K. Chung, M. H. Chen, W. L. Morgan, Y. Ralchenko and R. W. Lee, "FLY-CHK: Generalized population kinetics and spectral model for rapid spectroscopic analysis for all elements", High Energy Density Physics **1**, 3 (2005).

[97] A. Bar-Shalom, J. Oreg, W. H. Goldstein, D. Shvarts, and A. Zigler, "Super-transition-arrays: A model for the spectral analysis of hot, dense plasma", Phys. Rev. A **40**, 3183 (1989).

[98] O. Peyrusse, "A superconfiguration model for broadband spectroscopy of non-LTE plasmas", J. Phys. B: At. Mol. Opt. Phys. **33**, 4303 (2000).

[99] I. I. Sobelman, L. A. Vainshtein, and E. A. Yukov, *Excitation of Atoms and Broadening of Spectral Lines, Second Edition* (Springer, 1995).

[100] V. L. Jacobs, J. Davis, P. C. Kepple, and M. Blaha, "The influence of autoionization accompanied by excitation on dielectronic recombination and ionization equilibrium", ApJ **211**, 605 (1977).

[101] Wolfram Mathematica online integrator, *http://integrals.wolfram.com/index.jsp* (Accessed 10/05/2013).

[102] A. Behjat, G. J. Tallents, and D. Neely, "The characterization of a high-density gas jet", J. Phys. D: Appl. Phys. **30**, 2872 (1997).

[103] C. Spindloe, private communication.

[104] B. R. Benware, A. Ozols, J. J. Rocca, I. A. Artioukov, V. V. Kondratenko, and A.V. Vinogradov, "Focusing of a tabletop soft-x-ray laser beam and laser ablation ", Optics Letters **24**, 1714 (1999).

[105] M. Grisham, G. Vaschenko, C. S. Menoni, J. J. Rocca, Yu. P. Pershyn, E. N. Zubarev, D. L. Voronov, V. A. Sevryukova, V. V. Kondratenko, A. V. Vinogradov and I. A. Artioukov, "Damage to extreme-ultraviolet Sc/Si multilayer mirrors exposed to intense 46.9-nm laser pulses", Optics Letters **29**, 620 (2004).

[106] C. P. Ridgers, private communication.

[107] W. H. Press, S. A. Teukolsky, W. T. Vetterling, and B. P. Flannery, *Numerical Recipes in FORTRAN 77* (CUP, 1986).

[108] Wolfram MathWorld, determinant *http://mathworld.wolfram.com/Determinant.html* (Accessed 20/12/2015).

[109] K. F. Riley, M. P. Hobson and S. J. Bence, *Mathematical Methods for Physics and Engineering* (CUP, 1998).

[110] D. W. Marquardt, "An algorithm for least-squares estimation of nonlinear parameters", Journal of the Society for Industrial and Applied Mathematics, **11**, 431 (1963).

[111] J. W. Cooley and J. W. Tukey, "An algorithm for the machine calculation of complex Fourier series", Mathematics of Computation **19**, 297 (1965).

[112] M. Frigo and S. G. Johnson, "The design and implementation of FFTW3", Proc. IEEE **93**, 216 (2005).

[113] G. Evans, *Practical Numerical Integration* (Wiley, 1993).

[114] P. J. Davis and P. Rabinowitz, *Methods of Numerical Integration, Second Edition* (Academic Press, 1984).

[115] G. H. Golub and J. H. Welsch, Mathematics of Computation **23,** 221 (1969).

[116] L. N. Trefethen, "Is Gauss Quadrature Better than Clenshaw-Curtis?", SIAM Review **50**, 67 (2008).

[117] J. D. Lambert, *Numerical Methods for Ordinary Differential Systems: The Initial Value Problem* (Wiley, 1991).

[118] R. W. P. McWhirter and A. G. Hearn, "A Calculation of the Instantaneous Population Densities of the Excited Levels of Hydrogen-like Ions in a Plasma", Proc. Phys. Soc. **82**, 641 (1963).

[119] L. A. Wilson, G. J. Tallents, J. Pasley, D. S. Whittaker, S. J. Rose, O. Guilbaud, K. Cassou, S. Kazamias, S. Daboussi, M. Pittman, O. Delmas, J. Demailly, O. Neveu, and D. Ros, "Energy transport in short-pulse-laser-heated targets measured using extreme ultraviolet laser backlighting", Phys. Rev. E **86**, 026406 (2012).